5-2002

An Experimental and Numerical Study of Open Cavity Flows

Sekhar Radhakrishnan
University of Tennessee - Knoxville

To the Graduate Council:

I am submitting herewith a dissertation written by Sekhar Radhakrishnan entitled "An Experimental and Numerical Study of Open Cavity Flows." I have examined the final electronic copy of this dissertation for form and content and recommend that it be accepted in partial fulfillment of the requirements for the degree of Doctor of Philosophy, with a major in Mechanical Engineering.

Ahmad D. Vakili, Major Professor

We have read this dissertation and recommend its acceptance:

Charles Merkle, Gary Flandro, Bruce Bomar, Kenneth Kimble

Accepted for the Council:

Carolyn R. Hodges

Vice Provost and Dean of the Graduate School

(Original signatures are on file with official student records.)

To the Graduate Council:

I am submitting herewith a dissertation written by Sekhar Radhakrishnan entitled "An Experimental and Numerical Study of Open Cavity Flows." I have examined the final electronic copy of this dissertation for form and content and recommend that it be accepted in partial fulfillment of the requirements for the degree of Doctor of Philosophy, with a major in Mechanical Engineering.

Ahmad D. Vakili

Major Professor

We have read this dissertation
and recommend its acceptance:

Charles Merkle

Gary Flandro

Bruce Bomar

Kenneth Kimble

Accepted for the council:

Anne Mayhew
Vice Provost and Dean of
Graduate Studies

(Original Signatures are on file in the Graduate Student Services Office)

AN EXPERIMENTAL AND NUMERICAL STUDY OF OPEN CAVITY FLOWS

A Dissertation
Presented for the
Doctor of Philosophy
Degree
The University of Tennessee, Knoxville

Sekhar Radhakrishnan

May 2002

ACKNOWLEDGEMENTS

I gratefully acknowledge the love and support provided by my family in all the endeavors that I have undertaken. I would like to express my gratitude to my advisor, Dr. Ahmad Vakili for his guidance, encouragement and patience. My thanks and appreciation are also due to Keith Walker, Gary Payne, Ricky Meeker, Jim Goodman and other staff of the Gas Dynamics Laboratory. My heartfelt thanks to my committee members Dr. Charles Merkle, Dr.Gary Flandro, Dr. Kenneth Kimble and Dr. Bruce Bomar for their valuable advice and suggestions. I would also like to acknowledge my fellow graduate student Abraham Meganathan for his help.

ABSTRACT

This work is part of an ongoing study aimed at understanding of cavity flow oscillations. An experimental setup was designed, constructed, and tested to measure the Sound Pressure Levels (SPL) on the floor of four cavities, and to quantitatively visualize the flow-field inside the cavity. Measurements were made for a fixed cavity width by depth ratio of 3.33, for four length by depth (L/D) ratios of 2.0, 2.5, 3.5 and 4.5. Using Particle Image Velocimetry (PIV), the cavity velocity fields were obtained at subsonic speeds ranging from Mach 0.3 to Mach 0.6. Numerical simulations were performed for cavity geometry configurations and for flows corresponding to the experiments. Numerical simulations were carried out using a commercial code called CFD-ACE (U)®. Results of the simulations were used for comparison with experimental data. Numerical simulations led to further understanding of the mechanism of cavity oscillations.

Experimentally obtained dynamic pressure data show that for cavity with L/D = 2.5, the onset of oscillations occurs at a freestream Mach number of about 0.5. The measured cavity oscillation frequencies were in excellent agreement with the frequencies predicted by the modified Rossiter's semi-empirical formula. Sound Pressure Level peaks between the freestream Mach numbers of M = 0.57 and 0.6 exhibited the phenomenon of mode switching. Mode switching occurs when the dominant frequency of the cavity is changed from one mode to another with small changes in the freestream flow conditions. Onset of oscillations for cavity L/D = 4.5 occurred at a freestream Mach number of about 0.6 and the cavity oscillation frequencies were in good agreement with the frequencies predicted by the modified Rossiter's semi-empirical formula.

Post-processing of the PIV velocity data provided velocity, vorticity, turbulence intensity, and Reynolds stress information in the measurement region. Non-dimensional

vorticity contours showed the formation of shear layer (vorticity) immediately downstream of the cavity leading edge and its growth (convection) downstream. For cavity L/D = 2.5 and L/D = 4.5, the vorticity plots showed no organized vorticity structures in the shear layer at a freestream Mach number of 0.4. This corresponded to the absence of a large peak in the SPL for either of the cavity L/D ratios at a freestream Mach number of 0.4. On the other hand, for a Mach number of 0.6 vorticity plots for both displayed relatively well - organized vorticity structures in the shear layer. This finding was consistent with the well-defined SPL peak that was observed for both L/D ratios at this Mach number. For the cavity with L/D = 2.5, vorticity contours at M = 0.57 showed a highly non-linear growth of the shear layer that was interpreted as the mechanism responsible for mode switching. Velocity vectors showed periodic entrainment and ejection of fluid at the trailing edge of the cavity and the existence of recirculation zones that tended to occupy the downstream half of the cavity. Velocity contours displayed the growth of the shear layer and the characteristic shear layer motion associated with cavity oscillations.

Dynamic pressure data obtained from numerical simulations showed that the onset of oscillations for both cavity L/D ratios 2.5 and 4.5 was at a freestream Mach number of 0.4. This Mach number represented an earlier onset of oscillations numerically as compared with experiments. Frequencies predicted, numerically, were in good agreement with the modified Rossiter's semi-empirical formula. Mode switching phenomenon was exhibited between Mach numbers of 0.5 and 0.57 for cavity L/D = 2.5. Comparison of the phases between two pressure monitors on the floor of cavity L/D = 4.5 showed the existence of a upstream traveling disturbance (acoustic wave) that modulates the shear layer at its separation point.

The numerical simulations modeled the formation of a high concentration of vorticity immediately downstream of the cavity leading edge, the growth of the shear layer, and the

oscillation of the shear layer in close agreement with experiments. The numerically simulated velocity fields predicted all the major features of the cavity flow field as seen in experiments.

TABLE OF CONTENTS

LIST OF FIGURES

LIST OF TABLES

NOMENCLATURE

c	Speed of acoustic radiation (local speed of sound)
D	Depth of the cavity
f	Frequency
f_a', f_b', f_c'	Primary mode frequencies in the bicoherence spectrum
k_v	Vortex to freestream velocity ratio
L	Length of the cavity
m	Mode of oscillation
M	Mach Number
Re	Reynolds number (UL / ν)
Pa	RMS pressure at cavity opening
Pb	RMS pressure at base of cavity
St	Strouhal number (fL / U)
t	Time
U	Velocity
W	Width of the cavity
x	x-axis
y	y-axis
α	Acoustic wave emission delay
δ	Boundary layer thickness
γ	Specific heat ratio
λ	Wavelength

θ	Momentum thickness
$d\theta/dx$	Shear layer growth rate
dT, Δt	Time interval between two sequential images
Δx	Displacement
ω	Vorticity

Subscripts

a	acoustic
v	vortex
∞	freestream
c	convective

Chapter 1

Introduction

1.1 Cavity Oscillations

Cavity oscillations are rapid, organized fluctuations in the pressure, density, and velocity of the fluid inside a cavity which has been exposed to flow. Cavity oscillations have been observed to occur in wheel wells, ring cavities on projectiles, slotted wind tunnel walls, aerodynamic windows, bay vents on the Space Shuttle, and aircraft bomb bays [1]. These oscillations can cause structural deflection, structural fatigue, strong acoustic radiation, increased drag, and poor optical characteristics for aerodynamic windows. In order to prevent the deterioration of performance, the suppression of cavity oscillations is desirable. Suppression of cavity oscillations has been attempted with different levels of success by modifying different parts of the cavity flow. Techniques for suppression of cavity oscillation include direct and indirect free shear layer alteration (venting[2] and mass injection[3] from the cavity floor), separation and reattachment alteration (ramps[4]) and upstream boundary layer alteration (spoilers [5], vortex generators[6] and upstream mass injection[8,9]). The works of Vakili et al.[7,8] established the potential for successful suppression of cavity oscillations by passive or active steady or unsteady fluid injection upstream of the cavity. However, to achieve efficient suppression of these cavity oscillations, the mechanism of their production needs to be thoroughly understood. One such semi-empirical mechanism is described below.

1.2 Mechanism of Cavity Oscillations

The flow over a rectangular cavity and the geometric variables used in this study are shown in figure 1.1. The mechanism producing cavity oscillations consists of the creation of a free shear layer perturbation, amplification and downstream convection of the perturbation,

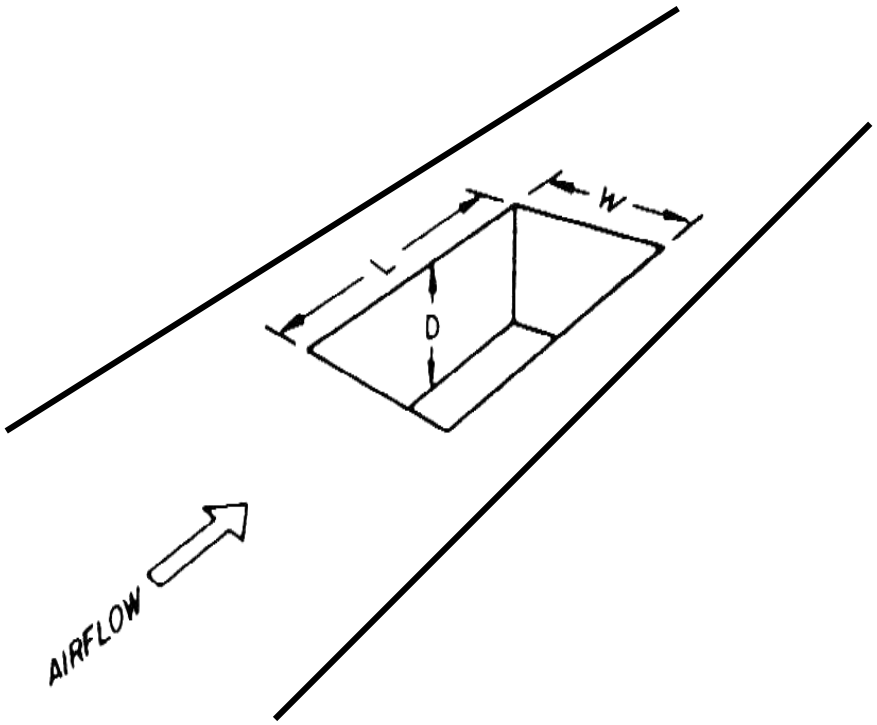

Figure 1.1. A Basic Rectangular Cavity Configuration

interaction of the perturbation with the trailing edge structure, and production of an upstream traveling influence (figure 1.2). The perturbation is a product of the inherently unstable nature of free shear layers. The perturbation may manifest itself as an oscillation of the free shear layer, a vortex, or other vorticity fluctuations. The perturbations are convected downstream and are amplified as they convect. The amplification is selective and non-linear. Upon reaching the trailing edge, the amplified perturbation interacts with the trailing edge structure and produces an upstream traveling influence. The upstream traveling influences are generally pressure disturbances, and may travel through the cavity, the free shear layer, and the freestream (when subsonic). The upstream traveling influence may create further free shear layer perturbations, usually at or near the separation point. When the upstream traveling influence and the downstream convecting perturbations are in proper phase, resonance may occur resulting in high amplitude unsteadiness inside the cavity. Though this mechanism predicts all the modes of possible oscillations, it is unable to predict the particular mode of oscillation that will occur or the amplitude of the oscillations.

1.3 Computational Cavity Flow Simulation

The complexity of cavity flows and the lack of a comprehensive analytic model leads to the consideration of numerical approaches. Cavity flows have been simulated on the computer with varying degrees of success and the approach used in this dissertation is described below.

The numerical simulations were performed on a commercial CFD package called CFD-ACE®. In CFD-ACE(U), the finite-volume approach is adopted to solve the compressible Navier-Stokes equations. It employs a co-located cell-centered variable arrangement. The SIMPLEC scheme is used to manipulate the continuity equation to formulate an equation for pressure. The Conjugate Gradient Squared (CGS) solver is

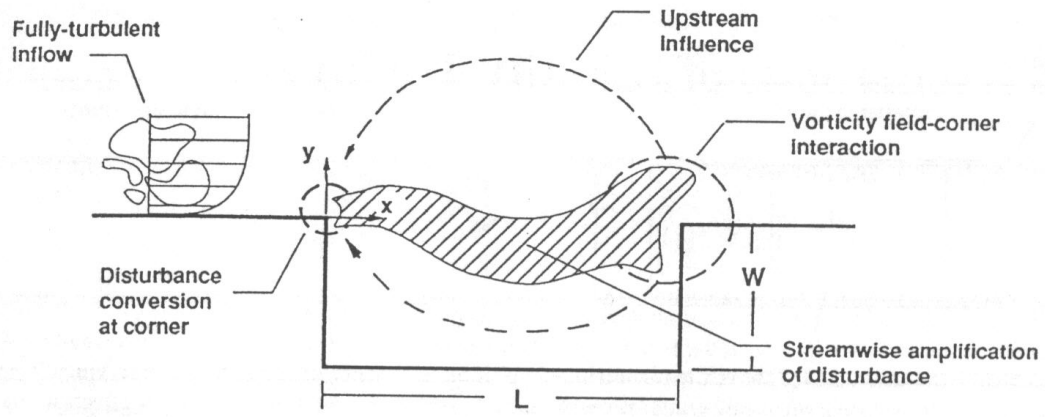

Figure 1.2 A Schematic Representation of a Cavity Oscillation Mechanism, Reproduced from Rockwell [1]

employed as an iterative, segregated solution method wherein the equation sets for each variable are solved sequentially and repeatedly until a converged solution is obtained. A k-ε turbulence model was used for obtaining turbulence closure.

1.4 Scope of Dissertation

Though extensive efforts have been made on the characterization and control of cavity flows, lack of detailed quantitative measurements inside the cavity makes it difficult to understand (a) the non-linear development of turbulent cavity shear layer, and (b) interaction of the disturbances (acoustic or other) with the shear layer to excite the flow instabilities. This knowledge is very important to achieve efficient control of flow over cavities. To this end, the following are the specific objectives of this work:

(a) To make flow field measurements over and inside open cavities at high subsonic speeds using Particle Image Velocimetry (PIV).

(b) To obtain unsteady pressure data on the floor of the open cavities at high subsonic speeds using unsteady pressure transducers.

(c) To compute cavity flow fields and pressure data using numerical approaches for the purposes of comparison with experiments.

It is anticipated that the results of this study would shed more light on understanding the physical process in cavity flows.

Chapter 2

Background and Literature Survey

2.1 Subsonic Cavity Flow-Field types

Flow over cavities can be classified based on

2.1.1 Length to Depth Ratio

(a) Shallow cavities

These cavities have their longest dimension in the streamwise direction (L/D > 1). Shallow cavities tend to resonate primarily in lengthwise mode.

(b) Deep cavities

These cavities have their longest dimension perpendicular to the streamwise direction (L/D < 1). Deep cavities tend to resonate primarily in depth mode.

2.1.2 Shear Layer Reattachment

(a) Closed flow

In closed cavities, the flow separates at the leading edge of the cavity and reattaches at some point along the cavity floor and separates again before reaching the trailing edge. Typically it has been observed to occur for an L/D ratio greater than or equal to 13[10]. The drag of closed cavities is substantially higher than that of open cavities[11]

(b) Open flow

In open cavities, the flow spans the length of the cavity and a shear layer is formed over the cavity. It occurs in cavities with L/D ratios less than or equal to 10. In this type of flow, cavity resonance can be sustained which generates high intensity acoustic tones[12].

(c) Transitional flow

The flow turning into the cavity may or may not impinge on the cavity floor before turning out and exiting. This occurs in cavities with L/D ratios between 10 and 13.

2.1.3 Cavity Oscillation

(a) Fluid Dynamic Oscillation

These are cavity oscillations that are driven solely by the inherent instability of the shear layer. Selective amplification of the instabilities and the pressure disturbances at the trailing edge are necessary. They are limited to situations where the cavity length is less than one-fourth of the acoustical wavelength. The length is too short for a standing wave to be present inside the cavity[13].

(b) Fluid Resonant Oscillation

These are cavity oscillations that result from a coupling of the inherent instability of the shear layer with one or more of the acoustic resonant modes of the cavity and are characterized by strong acoustic resonances inside the cavity. They occur when the shedding frequencies are sufficiently high and the acoustic wavelengths sufficiently short as to allow for standing waves inside the cavity. The acoustic resonances provide the upstream travelling influence.

(c) Fluid Elastic Oscillation

Fluid elastic oscillations result from the coupling of inherent instability of the shear layer with elastic movement of part or all of the cavity-bounding walls. The movement of the structure provides the pressure and acoustic resonance effects. Structural properties are important in these oscillations.

The classification of cavity oscillations as proposed by Rockwell and Naudascher[14] is shown in figure 2.1. In actual situations, these oscillations may occur simultaneously.

2.2 Review of Selected Experimental Work on Cavity Flows

Studies of the phenomenon of cavity oscillations covering a wide range of geometrical and flow parameters were performed by Karamcheti[15]. He studied the acoustic field of two-dimensional shallow cavities in the Mach number range of 0.25 to 1.5 using Schlieren and Inteferometric observations. He noticed that for a fixed freestream Mach number and depth, there exists a minimum length below which there was no sound emission and that the minimum length was inversely proportional to the Mach number. In a non-oscillating cavity, the shear layer bridges the cavity without strong interaction with the trailing edge. He also observed that the radiation was more intense for a laminar upstream boundary layer than for a turbulent upstream boundary layer.

Roshko[16] studied the pressure and velocity flow fields in cavities of L/D ratios ranging from 10.6 to 62.5 at low speeds (75 ft/sec to 210 ft/sec). He observed that the cavity flow was open for L/D ratios less than or equal to ten. He suggested that the shear layer impact on the trailing edge might be important in the sound production in cavities. He concluded that the drag increment due to cavity is almost entirely accounted for by the pressures on the walls.

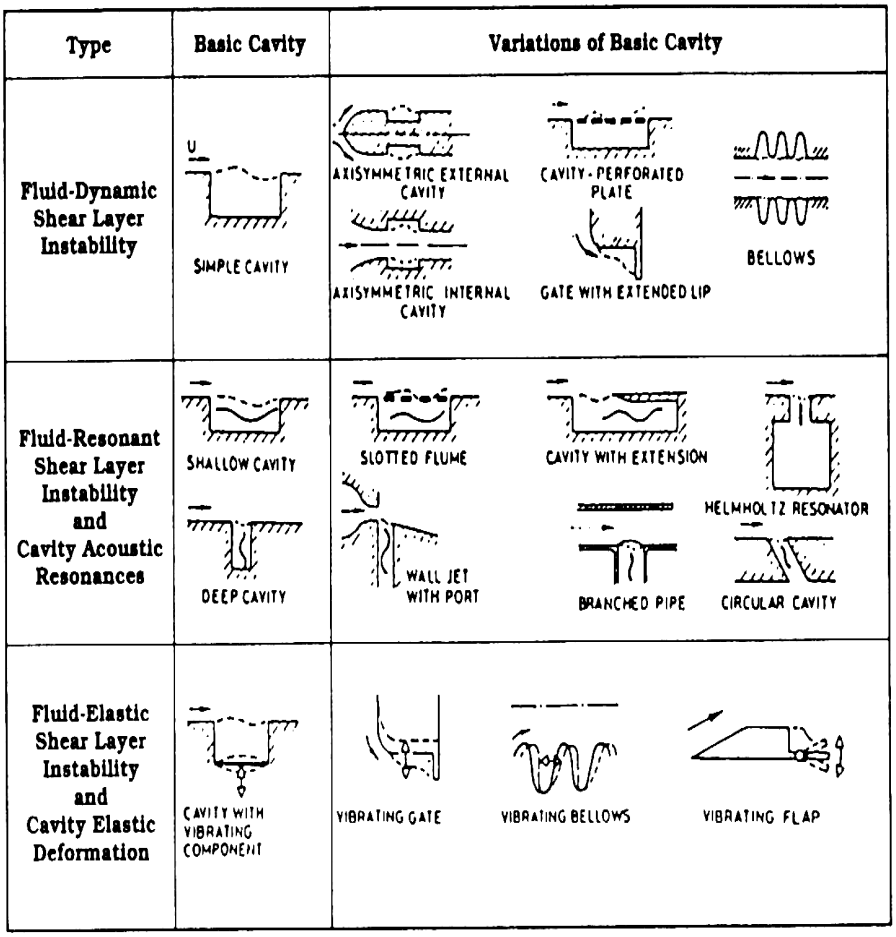

Figure 2 .1. Classification of Cavity Oscillations (reproduced from Rockwell and Naudascher[14])

Plumblee et al.[17] proposed that the observed discrete tones were the result of cavity resonance. They suggested that the frequencies of the tones were identical to those that corresponded to the maximum acoustic response of the cavity. According to this theory, the entire turbulent shear layer that spans the open end of the cavity provides a broad band noise source that drives the cavity oscillation. The response of the rectangular cavity to this broad band excitation is instrumental in selecting certain narrow band frequencies for amplification. But when experiments showed that flows with laminar upstream boundary layer produced louder tones, this line of reasoning was contradicted.

Rossiter[5] examined a series of rectangular cavities at low and transonic Mach numbers (0.4 – 1.2). He concluded that both periodic and random components of unsteady pressures could be present in the cavities. In general, the random component predominates in shallow cavities of $L/D > 4$ and the periodic component predominates in cavities having $L/D < 4$. The random component is more intense near the rear wall of the cavity. His high-speed shadowgraph motion pictures showed the periodic emission, downstream convection and amplification of the shed vortices. He also indicated that periodic components are due to an acoustic resonance in the cavity. Based on these observations he proposed a simple model (figure 2.2) consisting of periodic vortex emission, which is convected downstream and impinges on the trailing edge. After a small time delay, an acoustic wave is emitted from the trailing edge that travels upstream and perturbs the shear layer at the leading edge. He derived an empirical formula to predict the excitation frequency given by

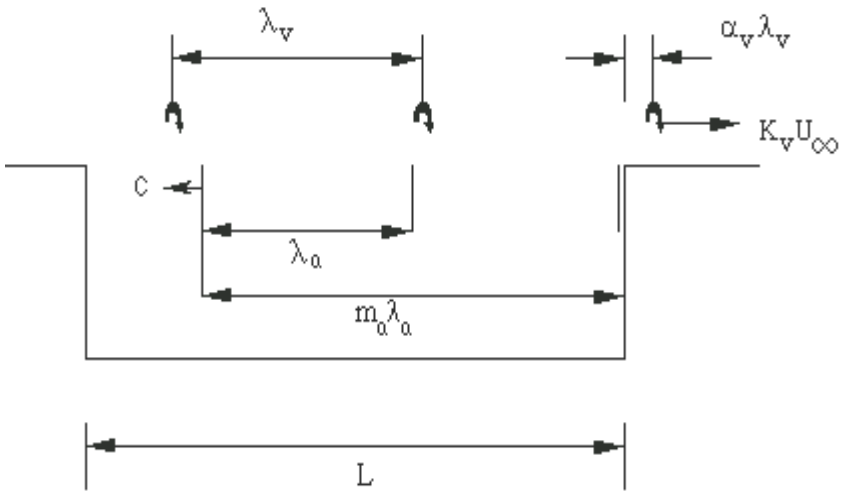

(a) Time = 0 Sound wave leaves rear lip

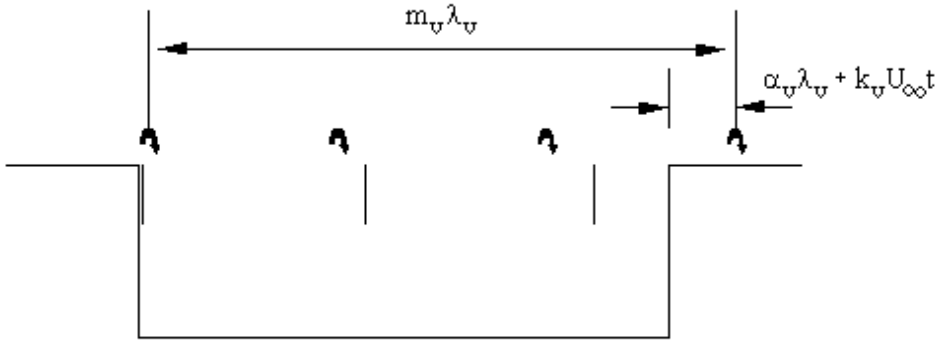

(b) Time = t Vortex leaves front lip

Figure 2.2 Rossiter's Cavity Model

$$St = \frac{fL}{U_\infty} = \frac{m - \alpha}{M + \frac{1}{K_v}}$$

where,

St = Strouhal number

f = Frequency

L = Length of the cavity

U_∞ = freestream velocity

M = Mach number

$K_v = U_c/U_\infty$ is the ratio of the shear layer velocity to free stream velocity, $K_v = 0.57$

m = mode number

α = empirical constant that accounts for the phase differences between (a) upstream arrival of the acoustic wave and subsequent vortex shedding (b) downstream interaction with the leading edge and subsequent acoustic radiation, $\alpha = 0.25$

This model agreed well with experimental data in the range of 0.4 to 1.5. Rossiter's assumption that the sonic speed inside the cavity is the same as the freestream sonic speed under-predicted the Strouhal number for Mach numbers above 1.5.

Heller, Holmes and Covert[18] modified the formula by assuming that the freestream stagnation sonic speed equals the cavity sonic speed. The modified Rossiter equation is

$$\frac{fL}{U_\infty} = \frac{m - \alpha}{\left\{ \frac{M_\infty}{\left[1 + \frac{\gamma - 1}{2} M_\infty^2\right]^{\frac{1}{2}}} + \frac{1}{K_v} \right\}}$$

where ,

γ = ratio of specific heats.

These formulas do not predict whether a self-sustained oscillation will occur. Neither can they predict the amplitude of the oscillations. The models do not describe how the acoustic wave interacts with the shear layer at the leading edge or how the acoustic disturbance is generated at the trailing edge wall in the first place.

Bilanin and Covert[19] improved on Rossiter's feedback model by relating the driving mechanism of oscillations to the instabilities of the free shear layer. The shear layer at the leading edge of the cavity is prone to Kelvin-Helmholtz instabilities. They assumed that the shear layer is being agitated periodically at the upstream lip of the cavity. This excites the flow instability waves of the shear layer as they propagate upstream. This fluctuating motion of the shear layer at the trailing edge of the cavity induces a periodic inflow of external flow into the cavity and half a period later a discharge of cavity fluid into the external flow. Bilanin and Covert attributed this mass inflow and outflow as the source of acoustic radiation. The acoustic disturbances then propagate upstream inside the cavity without disturbing the shear layer and excite the shear layer at the leading edge. Using a thin vortex sheet and a noise source at the downstream corner of the cavity, they modeled the flow and predicted the excitation frequencies that agreed well in high supersonic Mach number flows.

Heller and Bliss[20] using watertable visualization, observed periodic addition and removal of mass at the trailing edge in shallow cavities. They called this the "pseudo-piston" effect (shown in figure 2.3), which generates forward travelling waves in the cavity that reflect from the front bulkhead and become rearward travelling waves. They also identified that the

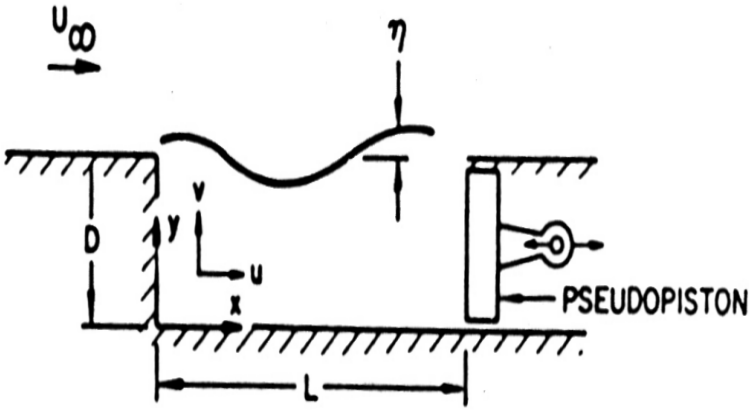

Figure 2 .3. “Pseudo-Piston” Effect (Reproduced from Heller and Bliss [20]

unsteady shear layer motion is responsible for the trailing edge mass addition and removal. The typical oscillation cycle is shown in figure 2.4.

Sarohia[21] examined ring cavities with dimensions of 0.05" to 0.875" in depth and 0" to 2" in length at speeds between 0 ft/sec and 80 ft/sec. Sarohia found a non-dimensional minimum length (ratio of length to momentum thickness) for oscillations to occur in laminar flows. He concluded that the phenomenon of oscillations in low-speed flows over cavities is not an acoustic resonance phenomenon in the longitudinal direction. These oscillations result from propagating disturbances that get amplified along the cavity shear layer. He also observed that the presence of strong cavity oscillations contributed to a large growth of the shear layer.

Tam and Block[22] investigated cavities in the low subsonic range ($M < 0.4$) and suggested that normal mode resonance dominated at Mach numbers less than 0.2 even for shallow cavities. Their model accounted for acoustic emission at the trailing edge as well as from the front, back and bottom of the cavity. They modeled the shear layer as an infinitesimally thin sheet and the acoustic disturbance at the trailing edge as a simple acoustic point source. Later they corrected it for the finite shear layer thickness based on a mean momentum thickness. Based on this model, they suggested that the ratio of the cavity length and momentum thickness of the shear layer were important.

Cattafesta et al.[23] studied the cause of additional peaks in the spectrum, particularly at low frequencies and the presence of multiple peaks in the power spectrum. They used time-frequency methods namely the Short Time Fourier Transform (STFT) and the continuous Morlet wavelet transform. They proposed a hypothesis that when three Rossiter modes ($f_c > f_b > f_a$) are present and satisfy the relation $(f_c - (f_a + f_b)) = \Delta f \approx 0$, significant nonlinear coupling

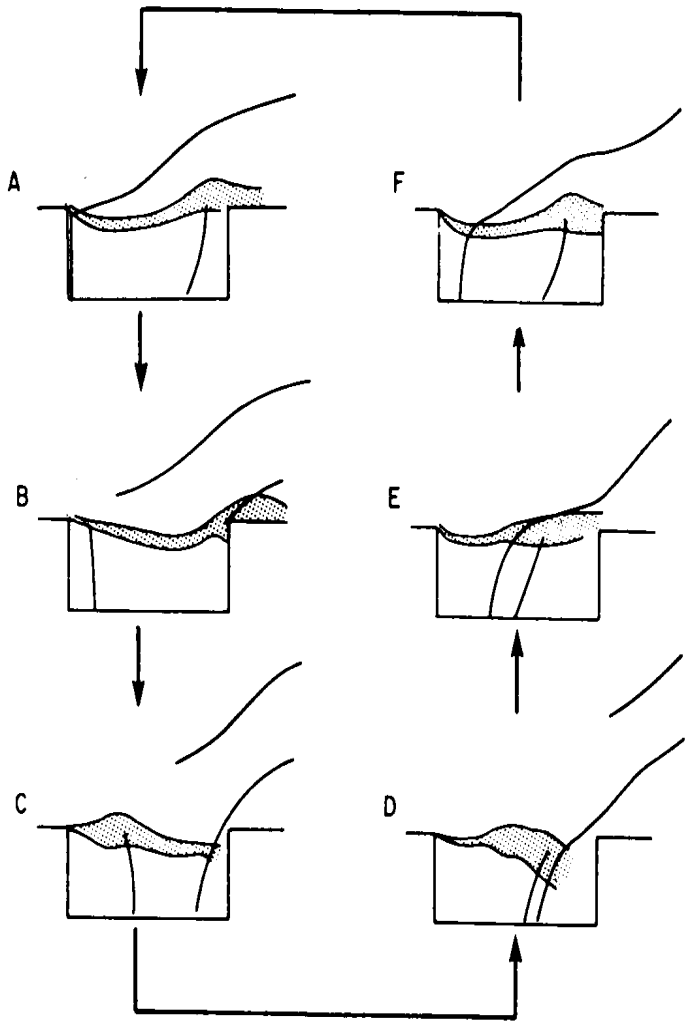

Figure 2.4 Typical Cavity Flow Oscillation Cycle as Proposed by Heller and Bliss [20]

can occur between the modes leading to a low frequency amplitude modulation of the primary modes at $f_m = \Delta f$ and larger than normal SPL. Even when this condition is not satisfied, the different interactions between the primary nodes create a low frequency mode that appears in the power spectrum and amplitude modulates the Rossiter modes.

Spina et al.[24] conducted detailed measurements of the cavity shear layer, the internal regions of the cavity and the acoustic near field with an optical deflectometer system at freestream Mach numbers of 0.4 and 0.6. They concluded that the convection speed ratio of the nodal disturbances is a function of frequency and that the upstream-travelling wave was acoustic in nature.

2.3 Review of Selected Computational Work on Cavity Flows

The complexity of cavity flows makes it very difficult to have a simple yet comprehensive analytic model. In addition to the experimental work on cavities which is reported in the paragraphs above, a lot of work has been done to predict cavity flow fields using numerical techniques. Xin Zhang [25] performed a computational analysis on a compressible flow oscillation due to shear layer instabilities over a cavity of length-to-depth ratio 3 at Mach 1.5 and 2.5. The mass-averaged Navier-Stokes equations were solved and turbulence closure was achieved using the k-ϖ model with compressibility corrections. Self-sustained oscillations were produced, and the shock wave-expansion wave interaction patterns, modes of the oscillation, sound pressure level, and the time-averaged surface pressure were found in good agreement with experimental results of previous investigations.

Rona and Dieudonne [26] used a second-order upwind in space, and time accurate numerical method to solve the Navier-Stokes equations for the Mach 1.5 Blasius laminar flow over a cavity of length-to-depth ratio 3. The Roe flux difference approximate method was used

to estimate the inviscid fluxes, and an explicit Runge-Kutta advanced the flow prediction in time. It was found that second order accurate upwind methods were able to reproduce consistently the flow details of aerodynamic instabilities characterized by the large-scale motion of vortices inside the cavity. Colonius et.al [27] studied the resonant instabilities in the flow past an open cavity using a sixth-order-accurate compact finite difference scheme which was able to resolve acoustic fields with velocity fluctuations five orders of magnitude smaller than near-field fluctuations. Time integration was performed with a fourth-order Runge-Kutta method. This combination of schemes resulted in very low numerical dissipation, and that allowed accurate wave propagation. The results of the simulations showed that, for shorter cavities, compared to the upstream boundary layer thickness, and lower Mach numbers, the cavity oscillates in a shear layer mode. Acoustic radiation was found to be intense and directional, but dominated by a single frequency corresponding to mode 2 of Rossiter's equation. For longer cavities, and higher mach numbers, the cavity oscillations became nearly periodic in time, with one cycle corresponding to the growth, shedding and ejection of a very large vortex. In this wake mode, the Strouhal number was found to be nearly independent of the Mach number.

Tam, Orkwis, and Disimile [28] obtained a comparison between results of several modifications of the Baldwin-Lomax turbulence model for the unsteady flow field of a supersonic 2-D open cavity. The tested modifications included the upstream relaxation, first peak, multiple-wall, Suhs' and inverse Suhs' approaches, and laminar flow in and above the cavity. Results from these simulations were compared with experimental data. None of the tested models were clearly superior, although multiple-wall modification was found to be adequate in all the tests.

Rona, Chen and Zhang [29] modeled the effects of a leading edge ramp and mass injection on supersonic cavity oscillations. The flow was found to undergo a coupled motion of shear layer flapping in transverse direction and vortex convection in streamwise direction due to non-linear propagation effects. The introduction of a leading edge ramp produced a reduction in sound pressure level. A passive pressure response was seen when mass injection was introduced, leading to local vorticity production and vortex shedding. Kim and Chokani [30] made a computational investigation of the supersonic turbulent flow past a 2-D rectangular cavity with passive venting. The passive venting was numerically simulated by the use of a linear form of the Darcy pressure-velocity law. The time accurate solutions of the 2-D, Reynolds averaged Navier-Stokes equations were generated using the explicit MacCormack scheme. The computational results showed good agreement with available experimental data. Lamp and Chokani [31] conducted a numerical study of the compressible cavity flow with active control. The cavity length-to-depth ratio was 4.33 and the freestream Mach number was 1.75. A small jet placed below the front lip of the cavity was used to force the shear layer at different amplitudes and frequencies. This technique was successful in reducing the amplitude of the oscillations. The effectiveness of the control was found to depend upon the jet frequency, amplitude, and duty cycle.

2.4 Important Cavity Flow and Geometry Parameters

The onset and amplitude of cavity oscillations depend on a number of variables that are related to the incoming boundary layer, the shear layer spanning the length of the cavity, the cavity geometry and the acoustic characteristics of the cavity. Some of the important parameters characterizing cavity flows are given below.

Upstream Boundary Layer & Freestream Parameters

Boundary layer thickness (δ)

Momentum thickness (θ)

Freestream velocity (U_∞)

Mach number (M)

Free Shear layer parameters

Hydrodynamic wavelength (λ)

Convective velocity (U_c)

Shear layer Frequency (f)

Shear layer momentum thickness ($\theta(x)$)

Shear layer growth rate ($d\theta / dx$)

Velocity profile (U(x))

Cavity Geometry Parameters

Cavity length (L)

Cavity depth (D)

Cavity width (W)

Acoustic Radiation Parameters

Acoustic wavelength (λ_a)

Speed of sound (c)

Acoustic frequency (f_a)

RMS pressure at base of cavity (P_b)

RMS pressure at cavity opening (P_o)

Figure 2.5 shows important flow and geometry parameters pertinent to cavity flows.

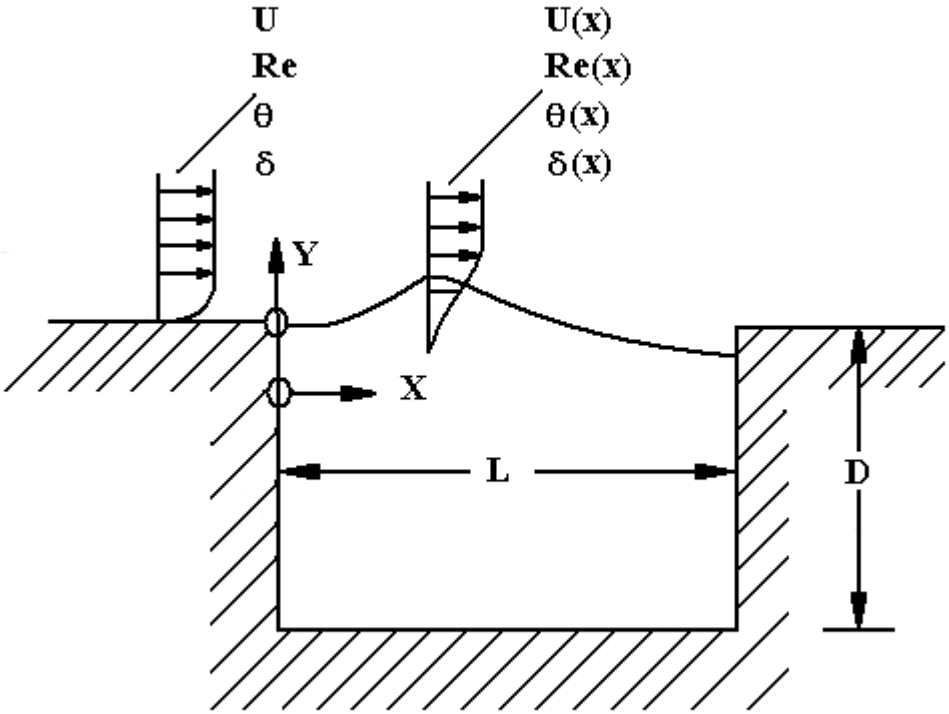

Figure 2.5 Key Flow and Geometry Parameters in Cavity Oscillations

Chapter 3

Experimental Approach

3.1 Wind Tunnel

All experiments were conducted in the blow-down wind tunnel in the UTSI Gas Dynamics Laboratory. The wind tunnel test section consists of an 8-inch by 8-inch square duct about four feet long. In general, the Mach number was maintained constant throughout each run, and was controlled by throttling the air from a high pressure storage tank via a control valve. However, the tunnel reference pressure, used to control the Mach number in the tunnel, was noted to vary during each run. This variation occurred because the manually controlled flow valve needed to be continuously adjusted as the tank pressure decreased. However, the flow conditions were found adequate for testing with the Mach number varying within two percent throughout the tests.

3.2 Cavity Model

A flat plate with a rectangular, three-dimensional cavity was designed, manufactured and mounted in the test section as shown in figure 3.1 and 3.2. The plate was 25.0 inches long, 6.5 inches wide, and 1.0 inch thick. It has a 0.5 inches long elliptic tip and 6.5 inch wedge-shaped leading edge contour to eliminate separation and have a fully developed boundary layer at the leading edge of the cavity. The ratio of the major axis to the minor axis of the elliptical tip contour was 16:1. The trailing edge had a 4.5-inch long wedge-shaped contour also to minimize the effects of separation. Four legs on the sides of the plate supported the model. The legs were designed to minimize tunnel blockage and to reduce flow separation.

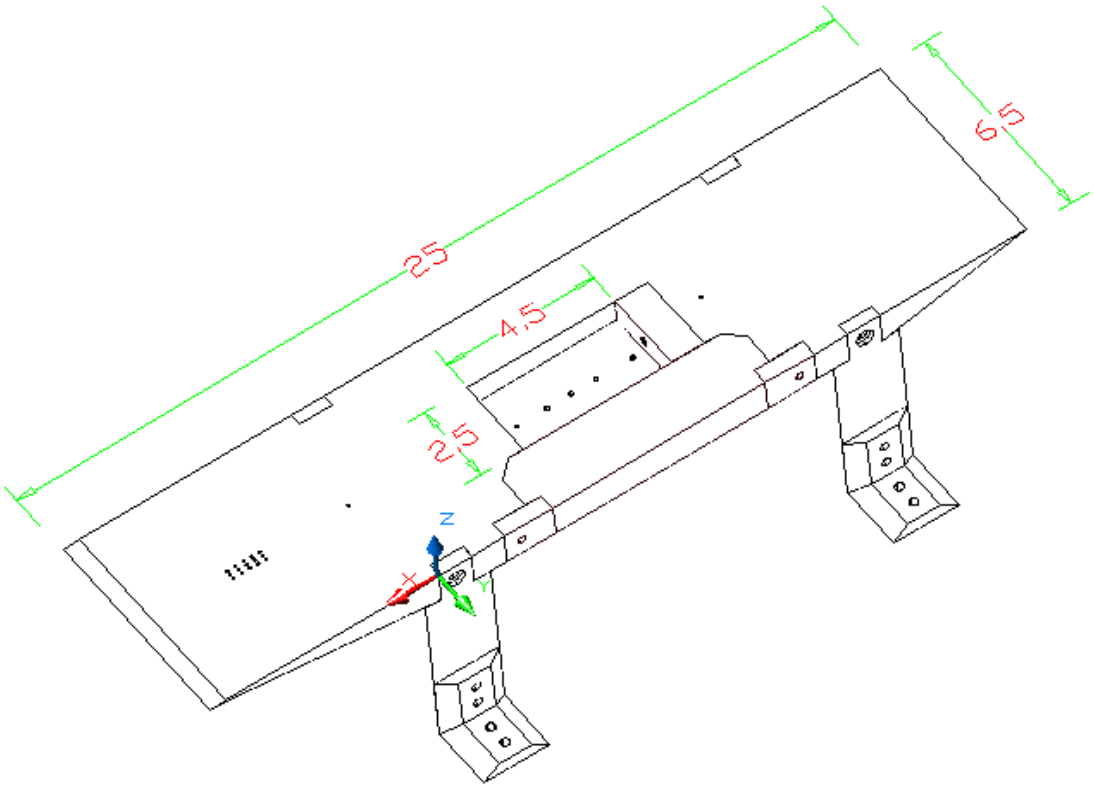

Figure 3.1. Cavity Model Installed in UTSI Blowdown Wind Tunnel

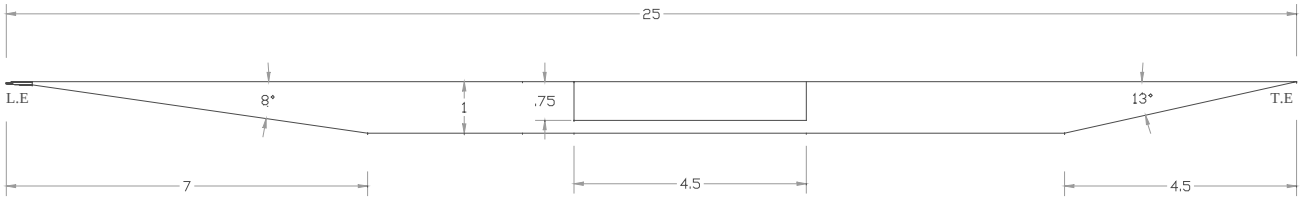

Figure 3.2 Cavity Model Layout (All Dimensions in Inches)

The cavity was located 11 inches aft of the leading edge of the flat plate. The maximum dimensions of the cavity were 4.5 inches long, 0.75 inches deep and 2.5 inches wide. Different L/D ratios (6.0, 4.5, 3.5, 2.5 and 2.0) were achieved by placing blocks of varying sizes inside the cavity while keeping the depth and width unchanged. The leading edge of the cavity remained fixed for a Reynolds number for each speed.

The cavity had a width to depth ratio of 3.33. A Plexiglas window (6.5 inch length x 2 inch width x 1 inch thick) was mounted on one side of the cavity. This window was specially designed to allow optical access inside the cavity. The tests were conducted at speeds ranging from 70 m/s to 210 m/s.

3.3 Instrumentation and Data Acquisition

3.3.1 Pressure Measurement System

Figure 3.3 shows the layout of the dynamic pressure transducers. For most L/D ratios two dynamic pressure transducers were used, one on the cavity floor near the trailing edge and the other on the cavity floor near the center of the cavity. The modified pressure transducers used were ENDEVCO® model 8507C-2. These transducers were of the omnidirectional, Piezoresistive type, and had a sensitivity of 150 mV/psi. For these transducers, the measurement error in SPL was quoted at ±0.5 dB up to 5000 Hz and ±5 dB from 5000 Hz to 20,000 Hz. The resonance frequency of these transducers was specified at 70,000 Hz. The output of the pressure transducers was connected to a computer with instrumentation simulation based on LABVIEW® software that was programmed to acquire the dynamic pressure data. Data from the pressure transducers was recorded at a sampling rate of 12000Hz giving a frequency range of 0 - 6000Hz. A total number of 6144 data points were obtained for

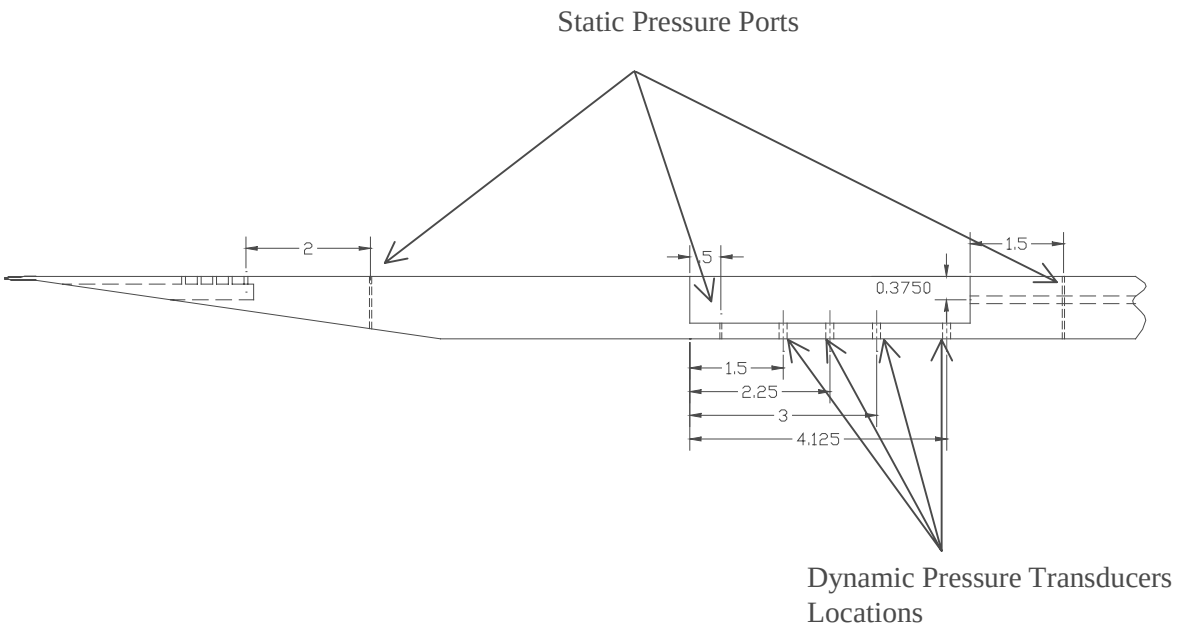

Figure 3.3. Cavity Instrumentation Layout, Position of Dynamic Pressure Transducers and Static Pressure Ports

each run condition. The data was divided into 6 blocks of 1024 points each, and a Fast Fourier Transform was performed on each block of data using a non-overlapping Hanning Window to yield the frequency domain. The six blocks of Fourier transformed data were averaged to yield the power spectrum.

Figure 3.3 also shows the layout of the static pressure ports that were used in conjunction with the plenum pressure to calculate the freestream velocity inside the test section of the wind tunnel using isentropic relations.

3.3.2 Particle Image Velocimetry (PIV) System

The PIV technique is based on the fundamental definition of velocity

$$u(x,t) = \frac{\Delta x(x,t)}{\Delta t}$$

where Δx is the displacement of a flow marker (seeds), located at 'x' at a time 't', over a short interval Δt separating observations of the marker images. This Lagrangian velocity of the marker is equated to the Eulerian velocity at that location. The accuracy of the measurements depends on how accurately the seeds follow the flow. PIV is performed by illuminating a seeded flow field with a planar laser sheet, which is pulsed at a known time interval forming one or more images of each seed particle. The elapsed time between each exposure of the seed particles is accurately recorded. This technique has the ability to collect non-intrusive data over large number of spatial grids. This ability to perform global flow field measurements enables PIV to identify instantaneous flow structures and compute spatial quantities such as vorticity and the instantaneous contribution of the Reynolds stress which are almost impossible to obtain in point based techniques [33].

The PIV system employed a continuum Nd:YAG laser to provide a thin planar laser sheet. The laser provides output pulse energy of 200 mJ/pulse at a wavelength of 532 nm (green

light). The horizontally and vertically polarized beams of the two lasers are combined with a polarized beam splitter. Then it is shaped by spherical and cylindrical lenses to form a planar beam profile with thickness of about 1 mm and width of 50 to 100 mm. TSI®'s PIVCAM 10-30 CCD camera with a 60 mm FL F/2.8 Micro Nikkor Lens was used for image capture. It has 1,026,144 light sensitive pixels and is capable of taking 30 frames per second. Since a pair of images is required to get a single velocity field, the effective sampling rate of the flow was 15 Hz. TSI® Model 610032 Laser pulse synchronizer controls the camera and the laser. External triggering is also possible. The synchronizer is connected to a 233 MHz personal computer loaded with TSI®'s Insight® software. This is a user friendly graphical user interface, which allows the operator to easily define all laser, camera and data recording options. The Insight® software allows for image spatial domain calibration so that the calculated velocity vectors could be expressed in useful engineering units (m/s). The schematic layout of the PIV system is shown in figure 3.4. The spatial domain of the image is calibrated by taking the image of a calibration scale placed over the model. The numbers of pixels between the identified points is then measured to give the calibration in terms of μm/pixel. The images for study were taken at a scale of 69 μm/pixel for L/D = 2.5 and 103 μm/pixel for L/D = 4.5. The optical window used in these was 2 inch wide. Therefore, diffraction was expected. Two calibrations were done. One calibration was done inside the cavity (through the optical window) and the other above the cavity. Except at the top edge of the window, the calibration results were the same. Along the edge, there was some shift in the images. The shift varied from 4 to 10 pixels along the edge. This depended on the perpendicularity between the laser sheet and the camera.

The system has the capability to take two sequential pictures within a minimum time interval of 200 nanoseconds. It uses the Frame Straddling technique to achieve such small dT.

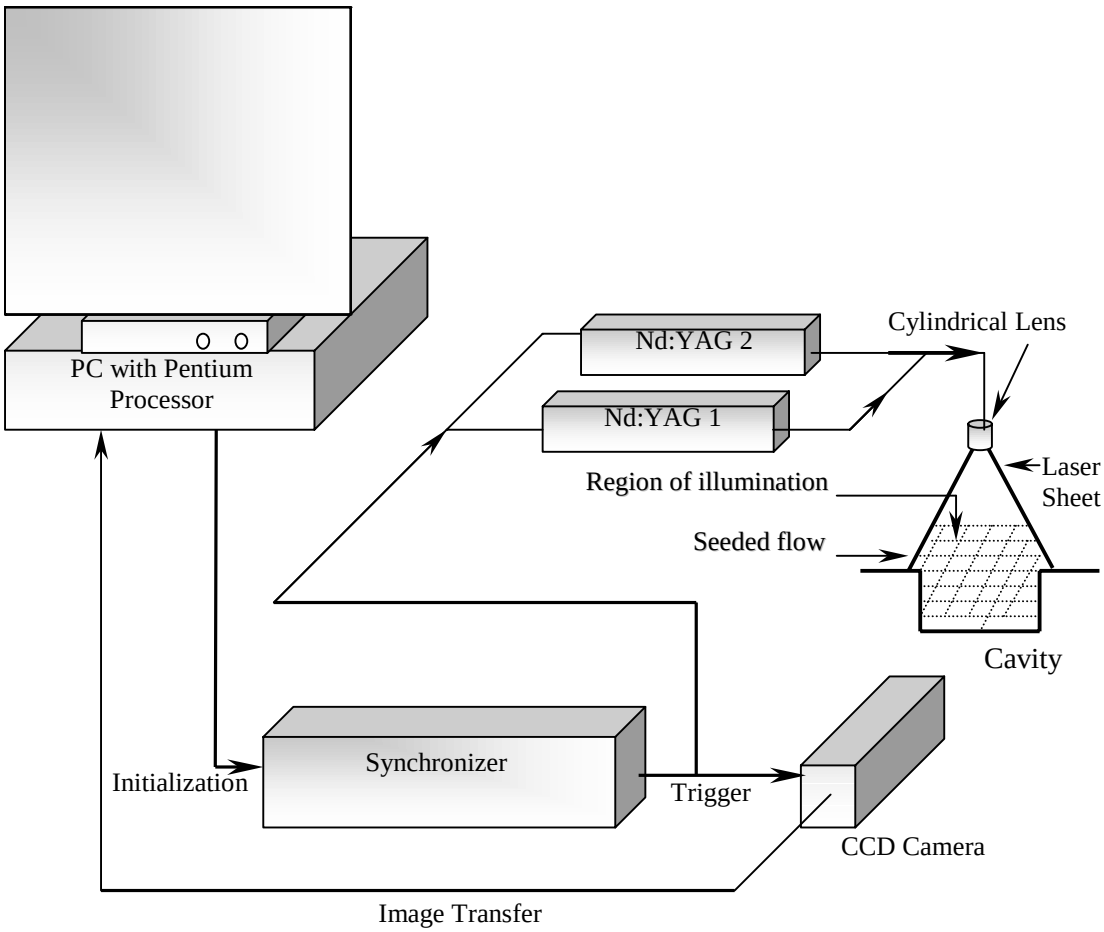

Figure 3.4. Schematic of the PIV System Setup [33]

For useful results, the image of the seed should move less than one-fourth of the interrogation spot in the time between the first and the second laser pulses. The images for this study were taken with a dT of 1μs.

As mentioned above, seeding is the most critical part for the success of PIV measurements. Atomized droplets of alcohol were used as seeding particles. Two concentric hollow metal tubes upstream of the model were employed as the seeding device. The inner tube carried pressurized air and forced the alcohol flowing in the annulus through a hole on the side of the outer tube. The atomized alcohol formed a spray over the cavity model that was suitable for PIV measurements.

The captured images are then processed using Insight® software. Correlation techniques are used to find the displacement of the particles. Correlation techniques generally used are auto-correlation and cross-correlation. In the auto-correlation technique, two sequential images of the seeded flow are taken in the same frame. This results in directional ambiguity, which requires image-shifting techniques to resolve. In this study, the two-frame cross-correlation technique was used. In this technique, two sequential images are captured in different frames and hence there is no directional ambiguity. The minimum time interval is also limited only by the ability of the camera. Figure 3.5 shows the basic difference between auto-correlation and cross-correlation. The image is divided into numerous regions called interrogation spots. Cross-correlation allows for much smaller spot sizes. Signal to noise ratio of 2-frame cross-correlation is the best among all the correlation methods. Cross-correlation is performed in the following sequence. The 2D FFT result of image 1 is multiplied by the complex conjugate of the 2D FFT result of image 2. Computing the 2D FFT of the multiplication result and taking the modulus gives the correlation result. The maximum peak in the correlation plane is at the location of the movement between the two recordings.

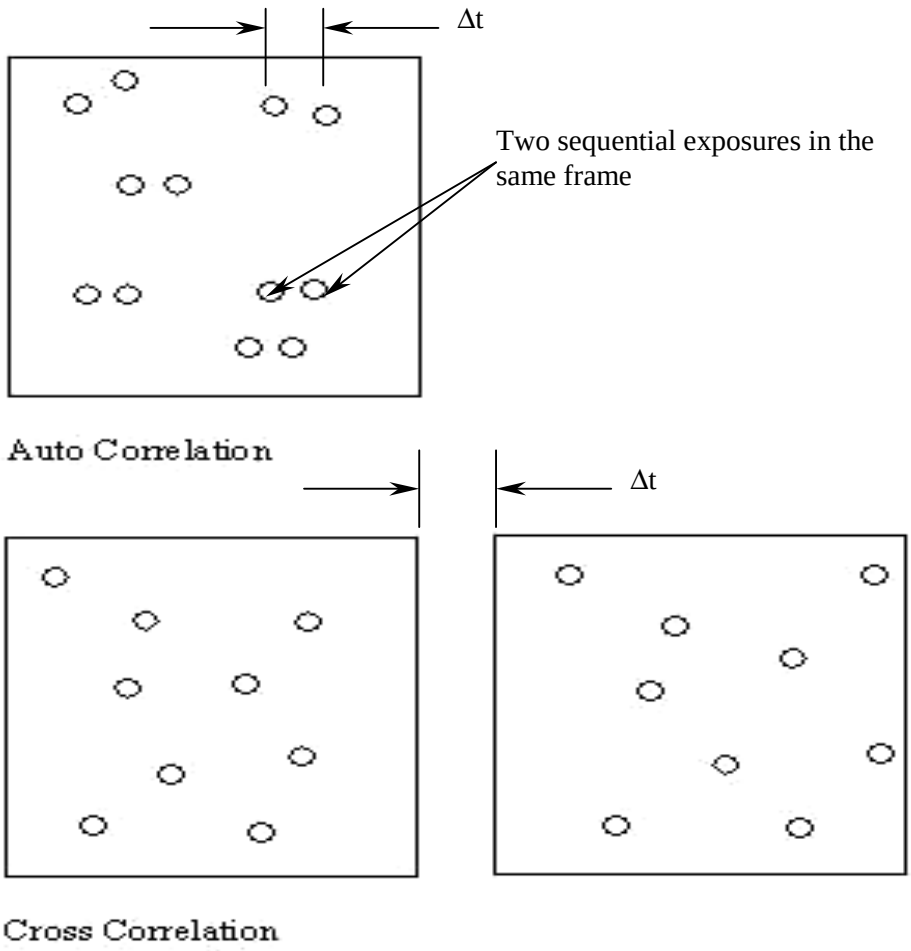

Figure 3.5. Correlation Techniques

Therefore, by determining the location of the highest peak in the correlation plane, the velocity vector is calculated.

3.3.3 PIV Resolution and Error Analysis

For all images, an interrogation spot size of 64 pixels by 64 pixels was used. The distance between any 2 vectors was 10 pixels (column-wise and row-wise) giving a resolution ranging from 0.69 mm for cavity L/D = 2.5 to 1.03 mm for cavity L/D = 4.5. There were a total of 5288 vectors obtained for cavity L/D = 2.5 with 1904 vectors within the cavity. Similarly, a total of 4815 vectors were obtained for cavity L/D = 4.5 with 1680 vectors within the cavity. The interrogation spot size was adequate to resolve flow structures of dimension 4.4 mm and higher for cavity L/D = 2.5. For cavity L/D = 4.5, the interrogation spot size was enough to resolve flow structures of dimension 6.6 mm and higher.

The measurement of velocity vectors by the method of PIV is affected by errors induced by the unsteadiness of the wind tunnel freestream, and the errors caused by the inaccuracies in the position of the seeding particles in the images. The following section seeks to quantify these errors for cavity L/D = 2.5 and 4.5 for freestream velocities of 0.4, 0.57 and 0.6.

For each run condition, at least 70 vector fields were averaged, and the mean and standard deviation of the velocity was calculated. For cavity L/D = 2.5 exposed to a freestream Mach number of 0.4, the standard deviation of the velocity in the freestream was found to be 4.54 % of the mean velocity.

The seeding particles in one pair of images moved a distance of 1.95 pixels in a time interval of 1μs for this Mach number. It was assumed that the percentage maximum error in the position of seed particles would be equal to 1.95/64 = 0.0305 or ±3.05 % of the actual position

of seeding particles, where the size of the interrogation spot size was set at 64 pixels by 64 pixels.

The vorticity, ω, was calculated using the following formula

$$\omega = \frac{\left\{\frac{dv}{dx} - \frac{du}{dy}\right\}}{2}$$

Since the calculation of the vorticity involves velocity gradients, the error in the vorticity was calculated as a vector sum of the error in velocity, and the error in the spatial positions of the seed particles. Therefore, the error in the vorticity is given by

$$error_{vort} = \sqrt{\left(error_{vel}^2 + error_{pos}^2\right)}$$

where $error_{vort}$, $error_{vel}$, and $error_{pos}$, represent the percentage error in vorticity, velocity and spatial position respectively.

A value of 5.47 % was obtained for the error in vorticity calculations for this run condition. Similar calculations were performed for cavity L/D = 2.5 for freestream velocities of 0.57 and 0.6. In addition, error band estimates for velocity and vorticity fields were obtained for cavity L/D = 4.5. The error band data is summarized in table 3.1.

A brief description of the common sources of error in PIV measurements is given in Appendix A.

Table 3.1 Summary of Velocity and Vorticity Error Bands

Cavity L/D = 2.5				Cavity L/D = 4.5			
Mach	% error velocity	% error position	% error vorticity	Mach	% error velocity	% error position	% error vorticity
0.4	4.54	3.05	5.47	0.4	4.98	2.05	5.38
0.57	2.98	4.29	5.22	0.57	4.33	2.88	5.20
0.6	3.68	4.50	5.81	0.6	3.67	3.03	4.76

Chapter 4

Numerical Methods

A finite-volume approach was adopted to predict the flow field of the cavities. The approach was implemented using the commercial software package called CFD-ACE(U)®. The finite-volume approach used by the software is described as follows [32].

4.1 Finite Volume Method

The solution domain is divided into a number of cells known as control volumes. The governing equations are then numerically integrated over each of these computational cells or control volumes. For example, consider the control volume in Figure 4.1. The geometric center of the control volume, which is denoted by *P*, is called the cell center. A collocated cell-centered variable arrangement is employed, that is, all dependent variables and material properties are stored at the cell center *P*. In other words, the average value of any quantity within a control volume is given by its value at the cell center.

Most of the governing equations can be expressed in the form of a generalized transport equation, equation 4.1,

$$\frac{\partial \rho \phi}{\partial t} + \nabla \bullet \left(\rho \overline{V} \phi \right) = \nabla \bullet \left(\Gamma \nabla \phi \right) + S_{\phi} \tag{4.1}$$

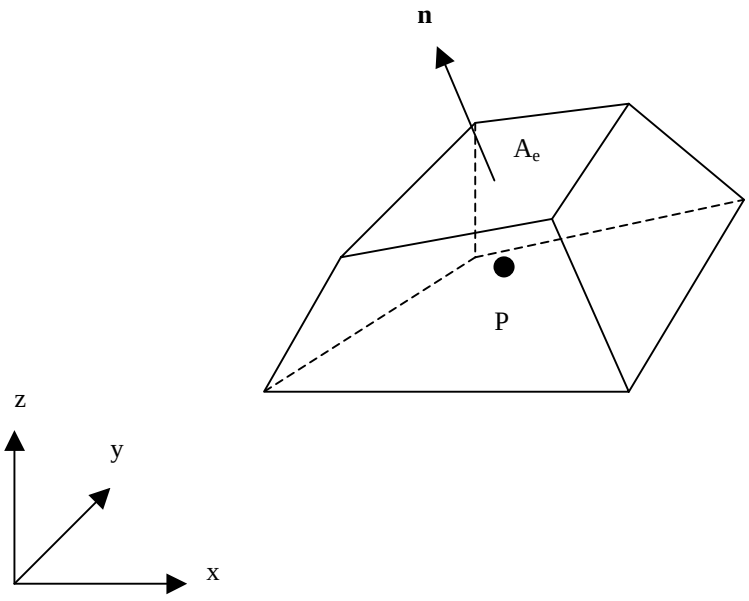

Figure 4.1 Three - Dimensional Computational Cell (Control Volume)

This equation is also known as the generic conservation equation for a quantity ϕ.

Integrating this equation over a control-volume cell, we have,

$$\int_{\vartheta} \frac{\partial(\rho\phi)}{\partial t} d\vartheta + \int_{\vartheta} \nabla \bullet \left(\rho \bar{V} \phi\right) d\vartheta = \int_{\vartheta} \nabla \bullet \left(\Gamma \nabla \phi\right) d\vartheta + \int_{\vartheta} S_{\phi} d\vartheta \tag{4.2}$$

4.1.1 Transient Term

The transient term in equation (4.2) is integrated as follows,

$$\int_{\vartheta} \frac{\partial(\rho\phi)}{\partial t} d\vartheta = \frac{\rho\phi\vartheta - \rho^0\phi^0\vartheta^0}{\Delta t} \tag{4.3}$$

where the superscript "*0*" denotes an older time, while no superscript denoted the current or the new time. The cell volume, represented by ϑ, may change with time (in particular when moving grids are used).

4.1.2 Convective Term

The convection term is discretized as follows,

$$\int_{\vartheta} \nabla \bullet \left(\rho \bar{V} \phi\right) d\vartheta = \oint_{A} \rho\phi \bar{V} \bullet \bar{n} dA = \sum_{e} \left(\rho_e \phi_e V_e^n\right) A_e = \sum_{e} C_e \phi_e \tag{4.4}$$

where subscript *e* denotes one of the faces of the cell in question, A_e is the area of the face *e*, V_e^n represents the velocity component in the direction that is normal to the face, and C_e is the mass flux across the face. The evaluation of ϕ at control volume faces is described next.

Let us consider a 2-D control volume as shown in figure 4.2. Because the solution variable ϕ is available only at the cell centers, the cell-face values of ϕ need to be interpolated. Various interpolation schemes with varying levels of numerical accuracy

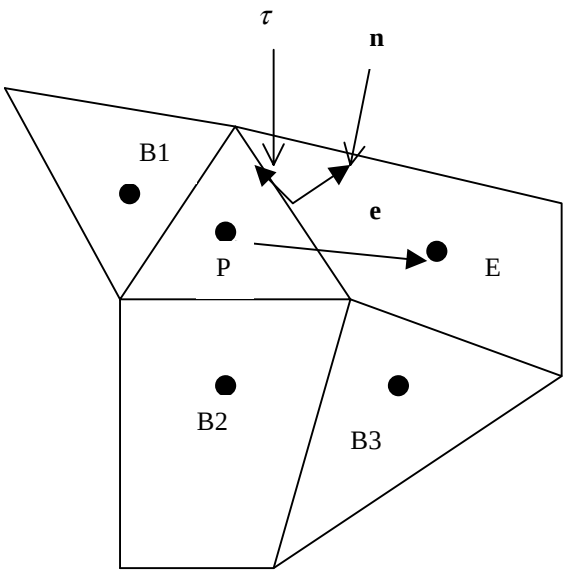

Figure 4.2 Computational Cell (Control Volume)

and stability exist. The first-order upwind, central difference, and second-order upwind interpolation schemes will be discussed in the sections below.

4.1.2.1 First-Order Upwind Scheme

In this scheme, ϕ_e is taken to be the value of ϕ at the upstream grid point, i.e., ϕ_e equals either ϕ_P or ϕ_E depending on the flow direction at cell face *e*. Mathematically, ϕ at this face can be expressed as

$$\phi_e^{UP} = \phi_P \text{ if } V_e^n > 0$$

$$\phi_e^{UP} = \phi_E \text{ if } V_e^n < 0 \tag{4.5}$$

This scheme has first-order accuracy, and is one of the most stable schemes.

4.1.2.2 Central Difference Scheme

In the conventional second-order accurate central difference scheme, ϕ_e is evaluated by arithmetically averaging the values at cell centers *P* and *E*, assuming that ϕ varies linearly between the cell centers, namely,

$$\phi_e^{CD} = \gamma_e \phi_P + (1-\gamma_e)\phi_e \tag{4.6}$$

where γ_e is the geometrical weighting function at the face *e*.

It is known that the conventional central difference scheme may give rise to non-physical oscillations in the numerical solution. Moreover, most iterative methods tend to be unstable when central differencing is used to evaluate convection terms. For most problems, some damping (or artificial viscosity) is needed for stability. In CFD-ACE(U)®, central difference with damping is constructed,

$$\phi_e = \alpha\phi_e^{UP} + (1-\alpha)\phi_e^{CD} \tag{4.7}$$

where α is a blending factor that combines the central scheme with the first-order upwind scheme to produce a stable scheme. The scheme represented by the preceding equation has an order of accuracy between 1 and 2.

4.1.2.3 Second – Order Upwind Differencing

The original idea of this scheme is to evaluate the cell face value by using linear interpolation of values at two upstream cells, instead of one. With the index notation in figure 4.2, the second-order upwind scheme gives,

$$\phi_e^{SUD} = f(\phi_{C3}, \phi_P) \text{ if } V_e^n > 0$$

$$\phi_e^{SUD} = g(\phi_{EE}, \phi_P) \text{ if } V_e^n < 0 \tag{4.8}$$

To improve stability characteristics, a blending factor is used with this scheme,

$$\phi_e = \alpha\phi_e^{UP} + (1-\alpha)\phi_e^{SUD} \tag{4.9}$$

4.1.3 Diffusion Terms

The diffusion term is discretized as follows,

$$\int_{\vartheta} \nabla\bullet(\Gamma\nabla\phi)d\vartheta = \int_A \Gamma\nabla\phi\bullet\bar{n}dA = \sum_e \Gamma_e\left(\frac{\partial\phi}{\partial n}\right)_e A_e \tag{4.10}$$

With the three unit vectors defined in figure 4.2, we have,

$$\frac{\partial\phi}{\partial n} = \frac{1}{\bar{n}\bullet\bar{e}}\left(\frac{\partial\phi}{\partial e} - \bar{e}\bullet\bar{\tau}\frac{\partial\phi}{\partial\tau}\right) \tag{4.11}$$

the diffusion term becomes

$$\int_{\vartheta} \nabla \bullet (\Gamma \nabla \phi) d\vartheta = \sum_{e} \frac{\Gamma_e}{\bar{n} \bullet \bar{e}} \left(\frac{\partial \phi}{\partial e} \right)_e A_e - \sum_{e} \frac{\tau \bullet \bar{e} \Gamma_e}{\bar{n} \bullet \bar{e}} \left(\frac{\partial \phi}{\partial \tau} \right)_e A_e \tag{4.12}$$

where,

$$\left(\frac{\partial \phi}{\partial e} \right)_e = \frac{\phi_E - \phi_P}{\delta_{P,E}} \tag{4.13}$$

$$\left(\frac{\partial \phi}{\partial \tau} \right)_e = \frac{\phi_{C2} - \phi_{C1}}{\delta_{C2,C1}} \tag{4.14}$$

where $\delta_{P,E}$ and $\delta_{C2,C1}$ represent the distance between E and P, and C2 and C1, respectively.

4.1.4 Source Term Linearization

If the source term is a function of ϕ itself, it is linearized as

$$S_\phi = S^U + S^P \phi \tag{4.15}$$

such that S^P is negative. In general, both S^P and S^U can be functions of ϕ. They are evaluated using the latest available value of ϕ, which is generally taken to be the value of ϕ at the end of the previous iteration. The linearized source term is integrated over the control volume that results in

$$\int_{\vartheta} S_\phi d\vartheta = S_U + S_P \phi_P \tag{4.16}$$

where $S_P = S^P \vartheta$ and $S_U = S^U \vartheta$.

4.1.5 Finite Difference Equations

If the numerically integrated transient, convection, diffusion and source terms are assembled together, it results in the following linear equation.

$$a_P \phi_P = \sum_{nb} a_{nb} \phi_{nb} + S_U \tag{4.17}$$

where the subscripts "*nb*" denote values at neighboring cells, a_{nb} are known as the link coefficients. This Finite Difference Equation (FDE) is the discrete equivalent of the continuous flow transport equation (4.1).

The FDE in equation (4.17), in general, is nonlinear because the link coefficients themselves are functions of ϕ_P, ϕ_{nb} etc. CFD-ACE(U)® employs an iterative procedure to solve the set of coupled nonlinear algebraic equations at every time step. A linear FDE is formed by evaluating the link coefficients with the values of ϕ available at the end of the previous iteration.

4.1.6 Velocity-Pressure Coupling

The continuity equation, which governs mass conservation, requires special attention because it cannot be written in the form of the general convection-diffusion equation. Also, it is used to determine the pressure field in the pressure-based method.

4.1.6.1 Continuity and Mass Evaluation

The mass conservation equation can be written as,

$$\frac{\partial \rho}{\partial t} + \nabla \bullet \left(\rho \bar{V} \right) = m \tag{4.18}$$

Integrating the above equation over the cell in figure 4.2, we have,

$$\frac{\rho\vartheta-\rho^0\vartheta^0}{\Delta t}+\sum_e \rho_e V_e^n A_e = m\vartheta \tag{4.19}$$

where V_e^n is the face-normal component of the velocity at face *e*, which is obtained by the inner product of the velocity vector (*u*, *v*, *w*) and the face-normal unit vector (n_x, n_y, n_z),

$$V_e^n = u_e n_x + v_e n_y + w_e n_z \tag{4.20}$$

Because the fluid density and velocities are available only at cell centers, their face values need to be interpolated from cell-center values. In CFD-ACE(U)® the cell-face mass flux is evaluated by averaging the momentum equation to the cell faces and relating the cell face velocity directly to the local pressure gradient. With the face values of both velocity and density obtained, the mass flux evaluation is accomplished.

4.1.6.2 Pressure Correction and "SIMPLEC" Algorithm

Solutions of the three momentum equations yield the three Cartesian components of velocity. Even though pressure is an important flow variable, no governing PDE for pressure is presented. Pressure-based methods utilize the continuity equation to formulate an equation for pressure. In CFD-ACE(U)®, the SIMPLEC scheme has been adopted.

4.1.7 Boundary Conditions

A control cell adjacent to the west boundary of the calculation domain is shown in Figure 4.3. A fictitious boundary node labeled *B* is shown. The finite-volume equation for node *P* is constructed as

$$a_P\phi_P = a_E\phi_E + a_N\phi_N + a_S\phi_S + S \tag{4.21}$$

Coefficient a_w is set to zero after the links to the boundary node are incorporated into the source term *S* in its linearized form,

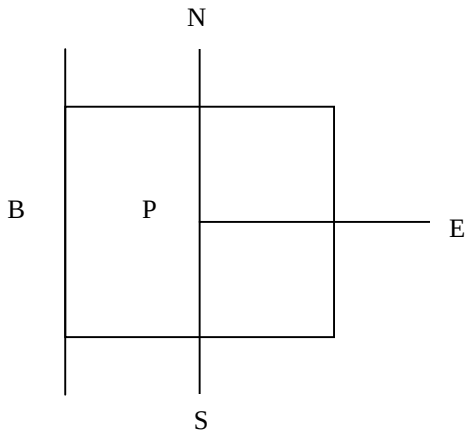

Figure 4.3 Computational Boundary Cell

$$S = S_U + S_P \phi_P \tag{4.22}$$

4.1.7.1 Fixed Value Boundary Condition

If the boundary value is fixed as ϕ_B, the source term is modified as,

$$S_U = S_U + a_W \phi_B \tag{4.23}$$

$$S_P = S_P - a_W \tag{4.24}$$

4.1.7.2 Zero-Flux Boundary Conditions

At zero-flux boundaries, such as adiabatic walls for heat and symmetric boundaries for any scalar variables, the boundary link coefficients are set to zero without modifying source terms.

4.1.8 Solution Methods

CFD-ACE(U)® uses an iterative, segregated solution method wherein the equation sets for each variable are solved sequentially and repeatedly until a converged solution is obtained. The overall solution method is presented in flowchart form in Figure 4.4.

4.1.8.1 Conjugate Gradient Squared (CGS) Solver

The CGS solver available in CFD-ACE(U)® is used in this study. The CGS algorithm applied to the system $A\phi = S$ is expressed as follows:

Initialization (n=0)

$$r_0 = S - A\phi_0$$

$$q_0 = p_{-1} = 0; p_{-1} = 1$$

n^{th} sweep (n > 0)

$$\rho_n = r_0^T r_n; \beta_n = \frac{\rho_n}{\rho_{n-1}}$$

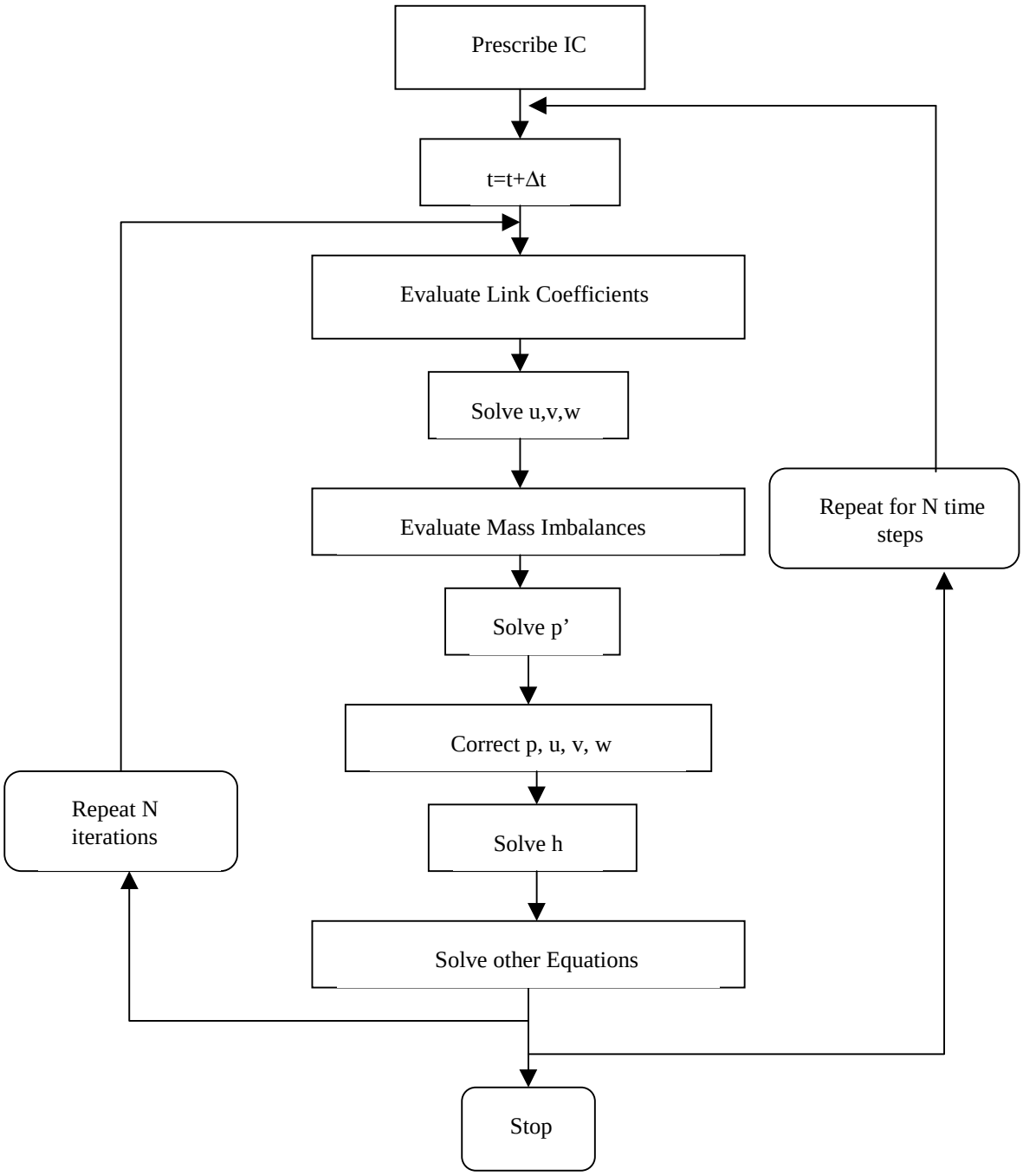

Figure 4.4 Solution Flowchart

$$u_n = r_n + \beta_n q_n$$

$$p_n = u_n + \beta_n \left(q_n + \beta_n p_{n-1} \right)$$

$$v_n = A p_n$$

$$\sigma_n = r_0^T v_n ; \alpha_n = \frac{\rho_n}{\sigma_n}$$

$$q_{n+1} = u_n - \alpha_n v_n$$

$$r_{n+1} = r_n - \alpha_n A \left(u_n + q_{n+1} \right)$$

$$\phi_{n+1} = \phi_n + \alpha_n \left(u_n + q_{n+1} \right)$$

where r_{n+1} is the residual at the n^{th} sweep.

4.2 Grid Convergence Study

A grid convergence study is a method for determining the ordered discretization error in a CFD simulation. The method involves performing the simulation on two or more successively finer grids. The method results in an error band on the computational result that indicates the possible difference between the discrete and continuum value.

4.2.1 Grid Considerations for a Grid Convergence Study

The easiest approach for generating the series of grids is to generate a grid with what one would consider fine grid spacing, perhaps reaching the upper limit of one's tolerance for generating a grid. Then coarser grids can be obtained by removing every other grid line in each coordinate direction. This can be continued to create additional levels of coarser grids. However,

it is not necessary to halve the number of grid points in each coordinate direction to obtain the coarser grid. Non-integer grid refinement or coarsening can be used. This may be desired since halving the grid may put the solution out of asymptotic range. However, the grid refinement ratio should be a minimum of **r>=1.1** to allow the discretization error to be differentiated from other error sources (iterative convergence errors, computer round-off, etc.).

4.2.2 Order of Grid Convergence

The order of grid convergence involves the behavior of the solution error defined as the difference between the discrete solution and the exact solution,

$$E = f(h) - f_{exact} = Ch^p - H.O.T.$$

Where **C** is a constant, **h** is a measure of grid spacing, and **p** is the order of convergence. A "second-order" solution would have **p=2.**

A CFD code uses a numerical algorithm that will provide a theoretical order of convergence; however, the boundary conditions, numerical models, and grid will reduce this order so that the observed order of convergence will likely be lower. Neglecting Higher-order terms, and taking the logarithm on both sides of the above equation results in

$$\ln(E) = \ln(C) + p \ln(h)$$

p can be obtained from three solutions using a constant grid refinement ratio **r,**

$$p = \ln\left(\frac{f_3 - f_2}{f_2 - f_1}\right)\frac{1}{\ln(r)}$$

4.2.3 Asymptotic Range of Convergence

Assessing the accuracy of a code and calculations requires that the grid is sufficiently refined such that the solution is in the asymptotic range of convergence. The asymptotic range of convergence is obtained when the grid spacing is such that the various grid spacings **h** and errors **E** result in the constancy of **C,**

$$C = E/h^p$$

4.2.4 Richardson's Extrapolation

Richardson extrapolation is a method for obtaining a higher-order estimate of the continuum value (value at zero grid spacing) from a series of lower-order discrete values. Richardson extrapolation is based on a Taylor series representation. If there are shocks and other discontinuities present, the Richardson extrapolation is invalid in the region of the discontinuity, but it still applies to solution functionals computed from the entire flow field.

4.2.5 Grid Convergence Index (GCI)

The Grid Convergence Index (GCI) is a measure of the percentage the computed value is away from the value of the asymptotic numerical value. It indicates an error band on how far the solution is away from the asymptotic value. A small value of the GCI indicates that the computation is in the asymptotic range.

The GCI on the fine grid is defined as

$$GCI_{fine} = \frac{F_s |\varepsilon|}{\left(r^p - 1\right)}$$

Where F_s is a factor of safety. The refinement may be spatial or in time. The facto of safety is recommended to be $F_s = 3.0$ for comparisons of two grids and $F_s = 1.25$ for comparisons over three or more grids. The higher factor of safety is recommended for reporting purposes and is quite conservative of the actual errors.

When an analysis involves many CFD simulations, one may want to use the coarser grid. It is then necessary to quantify the error for the coarser grid. The GCI for the coarser grid is defined as

$$GCI_{coarse} = \frac{F_s |\varepsilon| r^p}{\left(r^p - 1\right)}$$

It is important that each grid level yield solutions that are in the asymtotic range of convergence for the computed solution. This can be checked by observing two GCI values as computed over three grids,

$$GCI_{23} = r^p GCI_{12}$$

4.2.6 Effective Grid Refinement Ratio

If one generates a finer or coarser grid and is unsure of the value of grid refinement ratio to use, one can compute an effective grid refinement ratio as

$$\tau_{eff} = \left(\frac{N_1}{N_2}\right)^{\frac{1}{D}}$$

where N is the total number of grid points used for the grid and D is the dimension of the flow domain. This effective grid refinement ratio can also be used for unstructured grids.

Chapter 5

Results and Discussion

5.1 Comparison of Low Speed Cavity Data with Numerical Simulations

Meganathan [33] obtained PIV and unsteady pressure data to characterize open cavity flows at low speeds in the UTSI low speed wind tunnel. In order to evaluate the numerical algorithms used for this study will capture the essential features of the cavity flow oscillation, Meganathan's PIV and pressure data for cavity L/D = 2.0 at a freestream velocity of 64 m/s was compared with the results of the corresponding numerical simulations.

5.1.1 Boundary Layer Measurement, Freestream Velocity = 64 m/s

Figure 5.1 shows the experimental boundary layer profile obtained 6 mm upstream of the cavity leading edge for a freestream velocity of 64 m/s. The boundary layer thickness $\delta_{0.99}$ for this velocity profile was found to be 6.58 mm. The Reynolds number based on the length of the flat plate leading to the cavity was about 1.00 x 10^6. In order to decide whether the measured boundary layer is laminar or turbulent, turbulent and laminar boundary layer thickness values were calculated and compared with the experimental result. The following are the expressions used to calculate corresponding turbulent and laminar boundary layer thickness respectively.

Turbulent boundary layer thickness was calculated using:

$$\delta = 0.14\left(\frac{x}{\mathrm{Re}_x^{\frac{1}{7}}}\right)$$

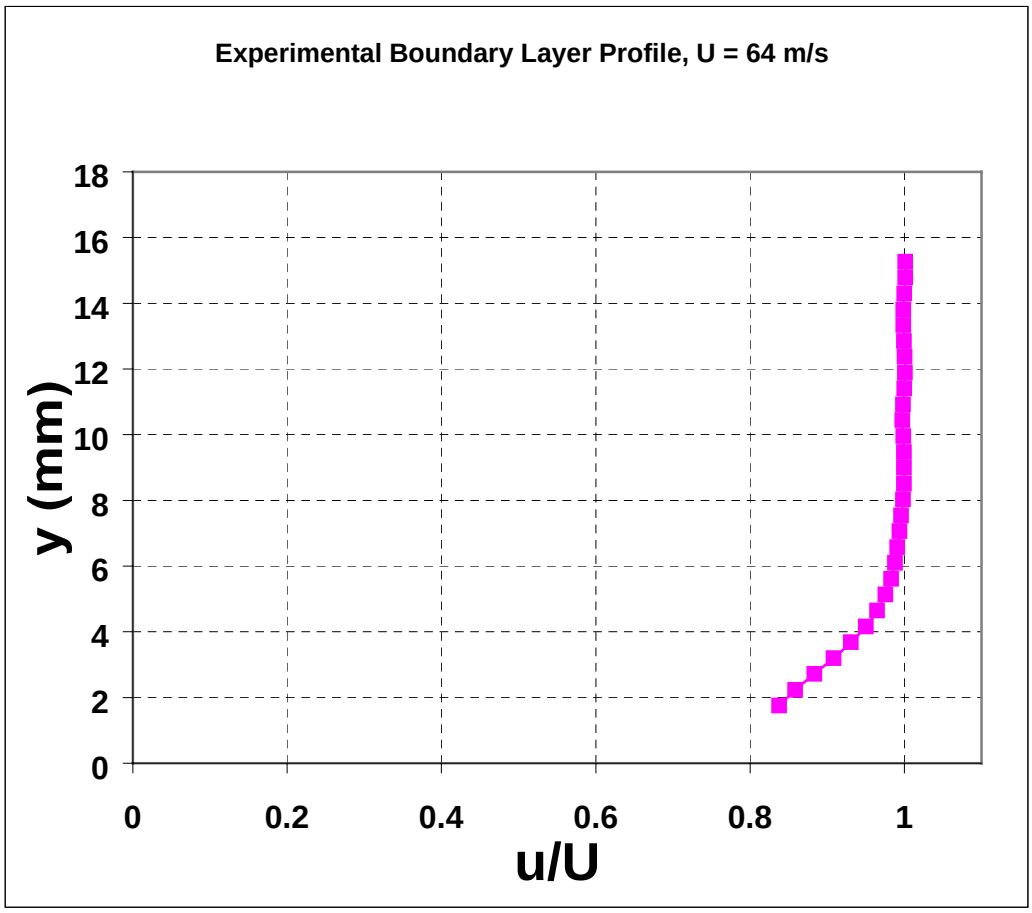

Figure 5.1 Cavity Upstream Boundary Layer Profile, U=64 m/s (214 ft/s) [33]

Laminar boundary layer thickness was calculated using:

$$\delta = 4.96\left(\frac{x}{\mathrm{Re}_x^{\frac{1}{2}}}\right)$$

The turbulent boundary layer expression yields a boundary layer thickness of 5.29 mm, and the laminar boundary layer formula yields a value of 1.34 mm as compared to 6.58 mm obtained from experiments. Since the experimental value of the boundary layer thickness compared better with the turbulent boundary layer thickness value, it was concluded that the boundary layer was turbulent for this cavity configuration.

5.1.2 Dynamic Pressure Measurements

Figure 5.2 exhibits the acoustic power spectrum as measured by a ¼-inch microphone placed on the floor of the cavity near the cavity trailing edge wall, for a cavity L/D of 2.0 and freestream velocity of 64 m/s. The spectrum shows a peak between 1900Hz and 2250 Hz, that has an amplitude of about 98 dB. This does not correspond to any of the Rossiter modes. In general, Meganathan's low speed experimental data showed very weak agreement with the Rossiter semi-empirical formula. This is because Rossiter's equation is not very accurate in predicting frequencies in the low Mach number range. The physical mechanism for this is believed to be the low levels of coherent vorticity in the shear layer at these low speeds. This results in the formation of weak and non-coherent vortices that are convected downstream to interact with the forward facing step of the cavity.

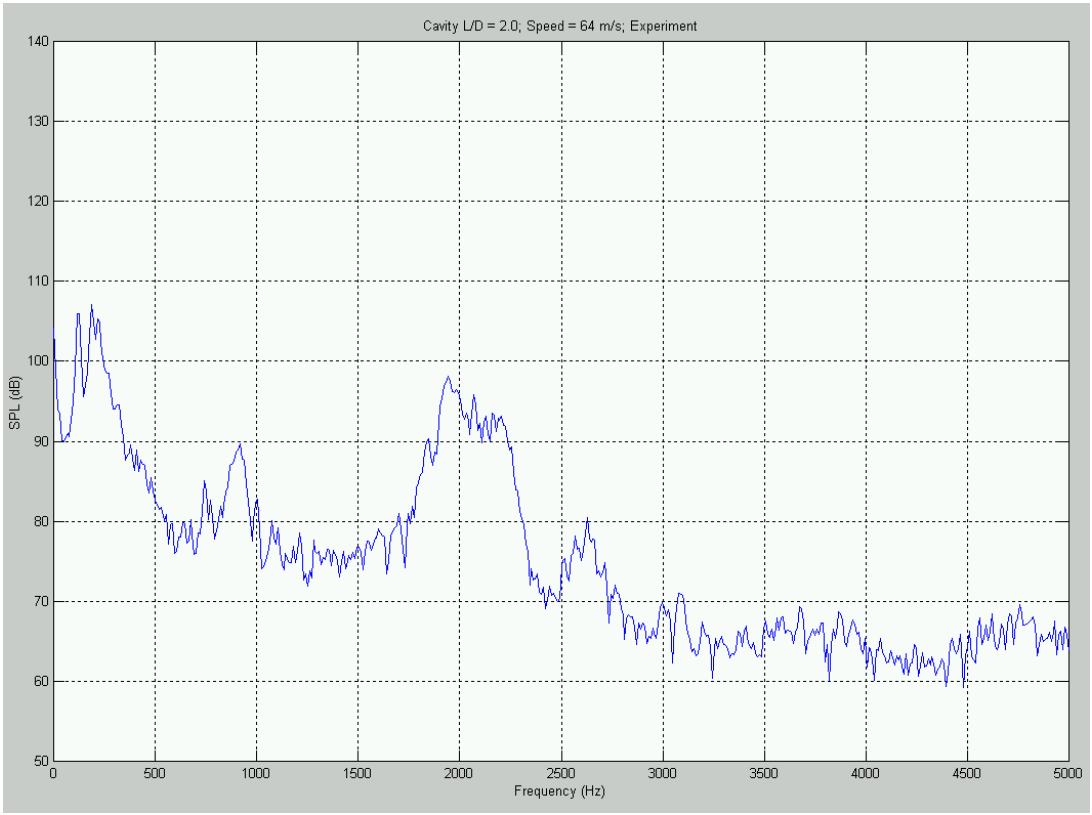

Figure 5.2 Power Spectrum, Cavity L/D = 2.0, U = 64 m/s [33]

5.1.3 Velocity Measurements

Using Particle Image Velocimetry, global flow field measurements were made for flow inside and over cavities with an L/D ratio of 2.0 at a speed of 64 m/s. The images were obtained at random phases of the shear layer oscillation cycle (i.e., they were not taken during the same oscillation cycle and the phase relationship between any two images is not known). The sequence in which they are presented does not necessarily represent the sequence in which the oscillation cycle takes place. All presented images are post-processed images, which include data-validation by a range filter, a median filter and a mean filter. The filters remove bad vectors (as in the top right hand corner of figure 5.3(a)) that are mainly due to non-uniform seeding. The removed vectors were replaced by interpolation if valid vectors are available in the neighborhood. On an average, about 5 % of velocity field vectors were obtained by interpolation. A minimal Gaussian smoothing (3 x 3) was also applied. The effects of post processing are shown in figures 5.3(a-d).

5.1.3.1 Cavity L/D = 2.0, U = 64 m/s

Instantaneous velocity vector fields for cavity L/D = 2.0 at a freestream velocity of 64 m/s are shown in figures 5.4(a-f). The vectors show the shear layer oscillating near the trailing edge and a re-circulation zone occupying the whole cavity. The velocity vector profiles show that the thickness of the shear layer increases in the downstream direction. This increase in shear layer thickness is attributed to the entrainment of fluid by the shear layer. The speed inside the cavity reaches up to 25% of the freestream velocity. Comparing the sequence of images in the area above the cavity shows fluctuations in velocity up to about 20% of freestream. This could be a local change in velocity because of the presence of an oscillating cavity in a subsonic flow.

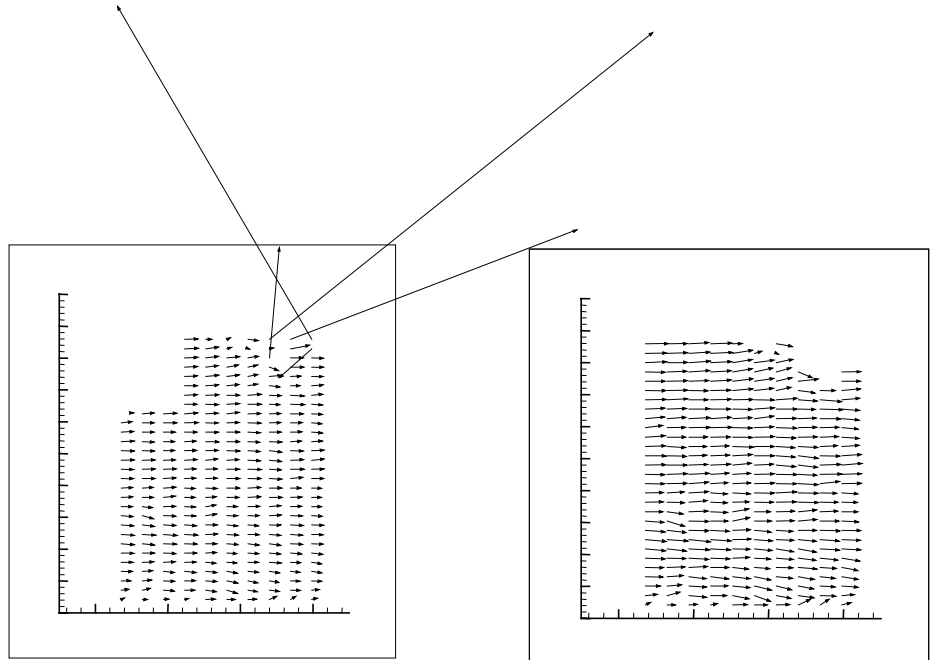

a) Raw vector Image b) After Applying Range and Mean Filter

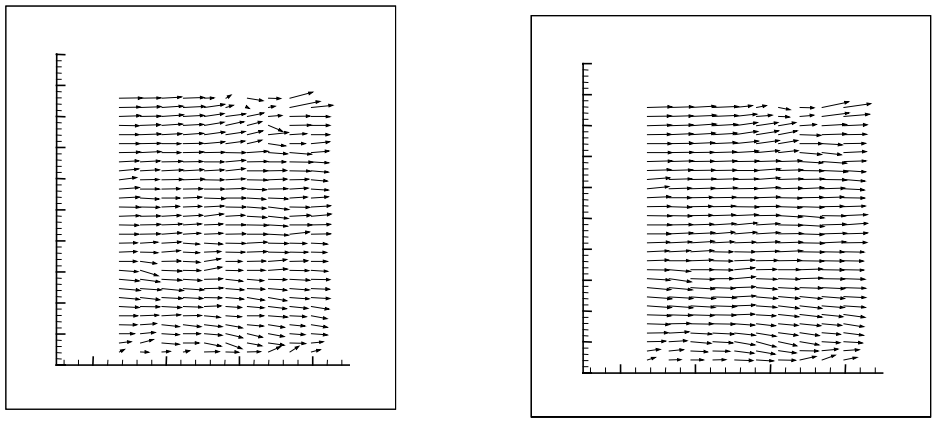

c) After Interpolation d) After Gaussian Smoothing (3x3)

Figure 5.3 Effects of Post-Processing [33]

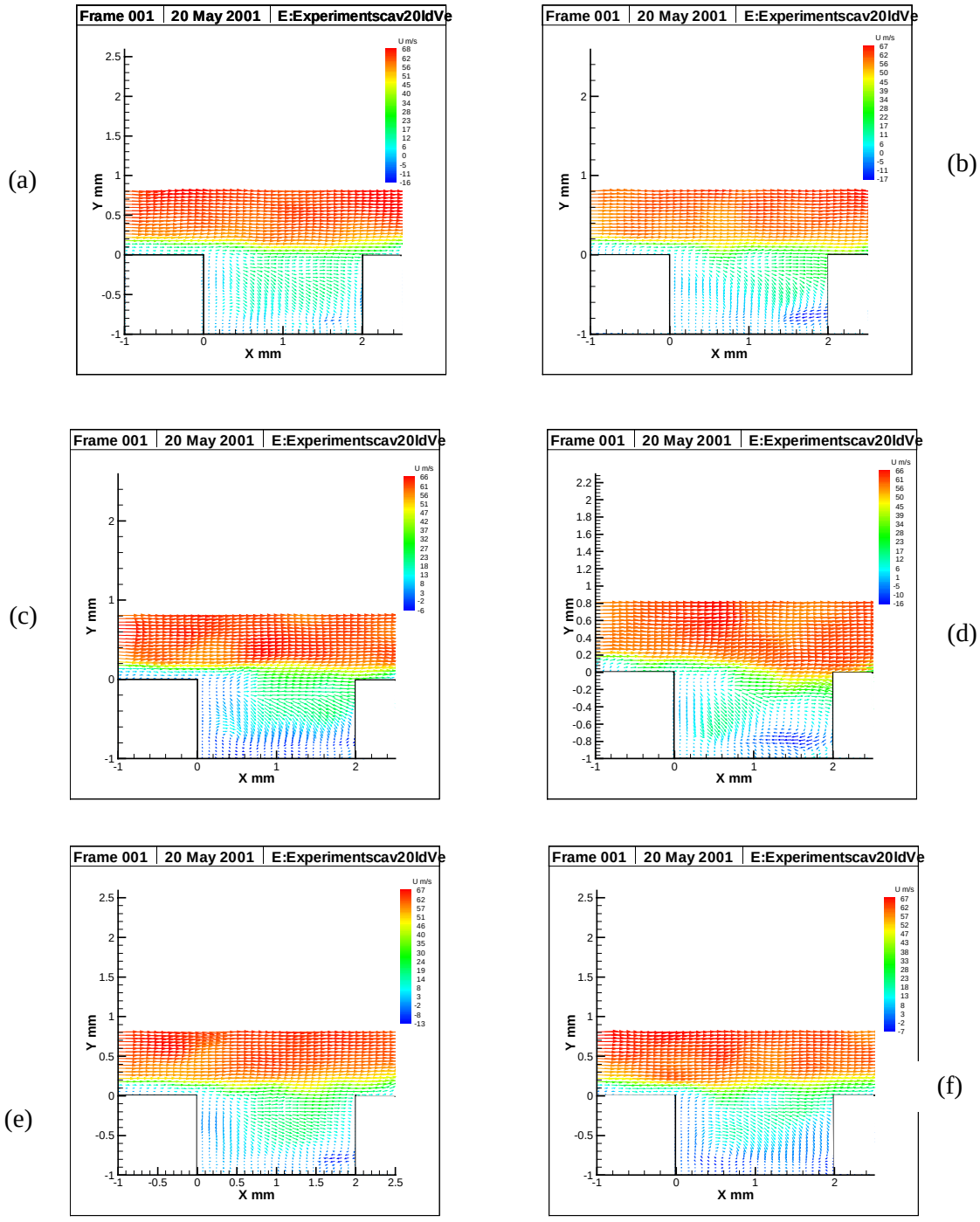

Figure 5.4 Instantaneous Experimental Velocity Vectors, Cavity L/D = 2.0, U = 64 m/s [33]

Figures 5.5(a-f) show the corresponding instantaneous velocity contours. An animation of the velocity contour images show the oscillation of the fluid layer just upstream of the leading edge in addition to the shear layer oscillation near the trailing edge of the cavity. These oscillations excite the instability waves of the shear layer.

Figures 5.6(a-f) show the instantaneous vorticity contours illustrating the various stages in the oscillatory cycle. Vorticity was calculated using the relation

$$\omega = \frac{\left\{\frac{dv}{dx} - \frac{du}{dy}\right\}}{2} \tag{5.3}$$

The presented images have non-dimensional vorticities of the form $\frac{\omega D}{U}$. Contour levels range between $\frac{\omega D}{U}$ = -1.45(blue) and $\frac{\omega D}{U}$ = 0.2(red). It is evident from the vorticity contour that vortical disturbances are present inside the shear layer. They show the shear layer oscillating near the trailing edge and the vorticity propagating downstream, thus giving physical evidence of the cavity oscillation mechanism.

5.1.4 Numerical Formulation

The numerical simulations were performed using a commercial CFD package called CFD-ACE®. In CFD-ACE(U), the finite-volume approach is adopted due to its attractive capability of conserving solution quantities. It employs a co-located cell-centered variable arrangement. The SIMPLEC scheme is used to manipulate the continuity equation to formulate an equation for pressure. The Conjugate Gradient Squared (CGS) solver is employed as an iterative, segregated solution method wherein the equation sets for each variable are solved sequentially and repeatedly until a converged solution is obtained.

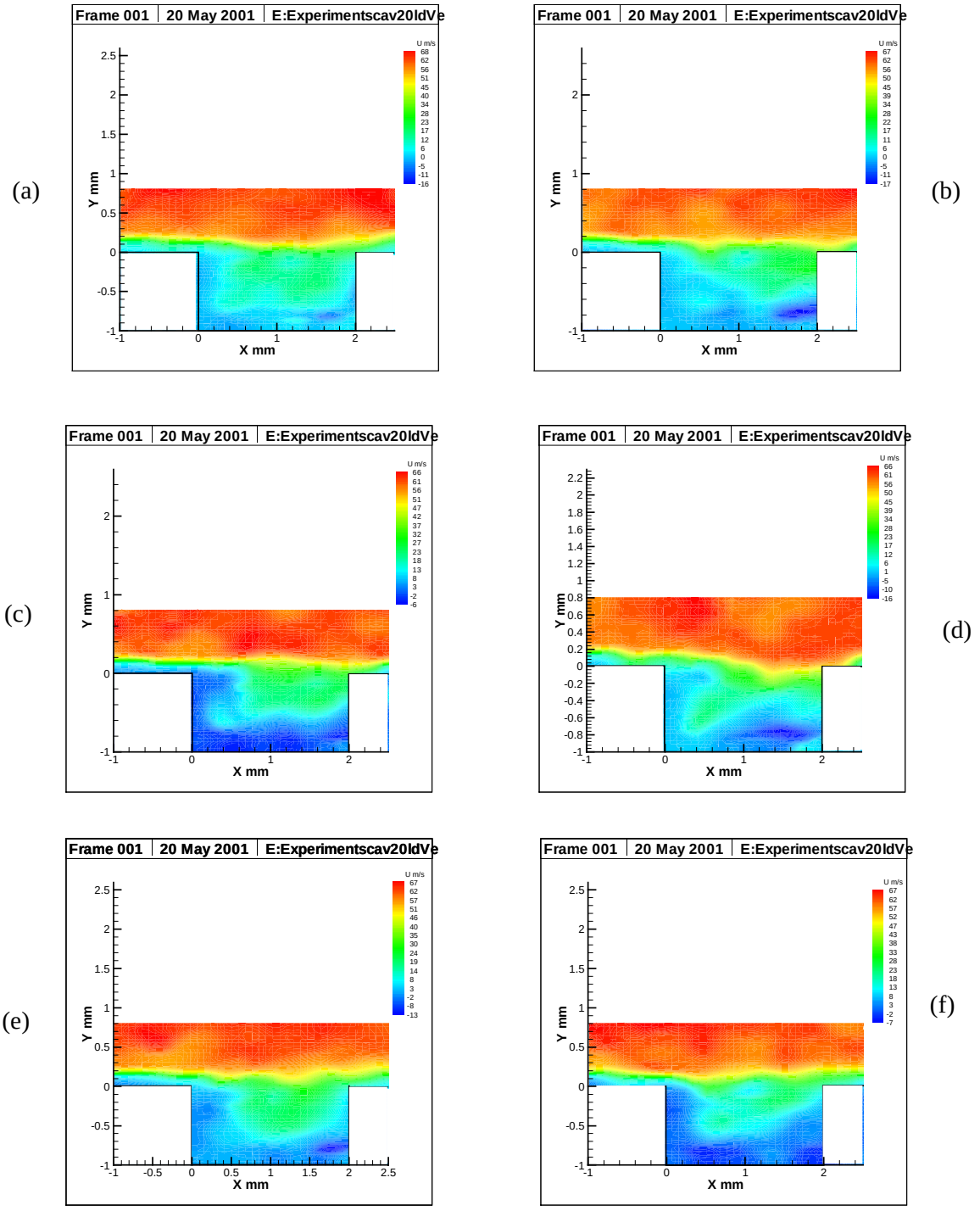

Figure 5.5 Instantaneous Experimental Velocity Contours, Cavity L/D = 2.0, U = 64 m/s [33]

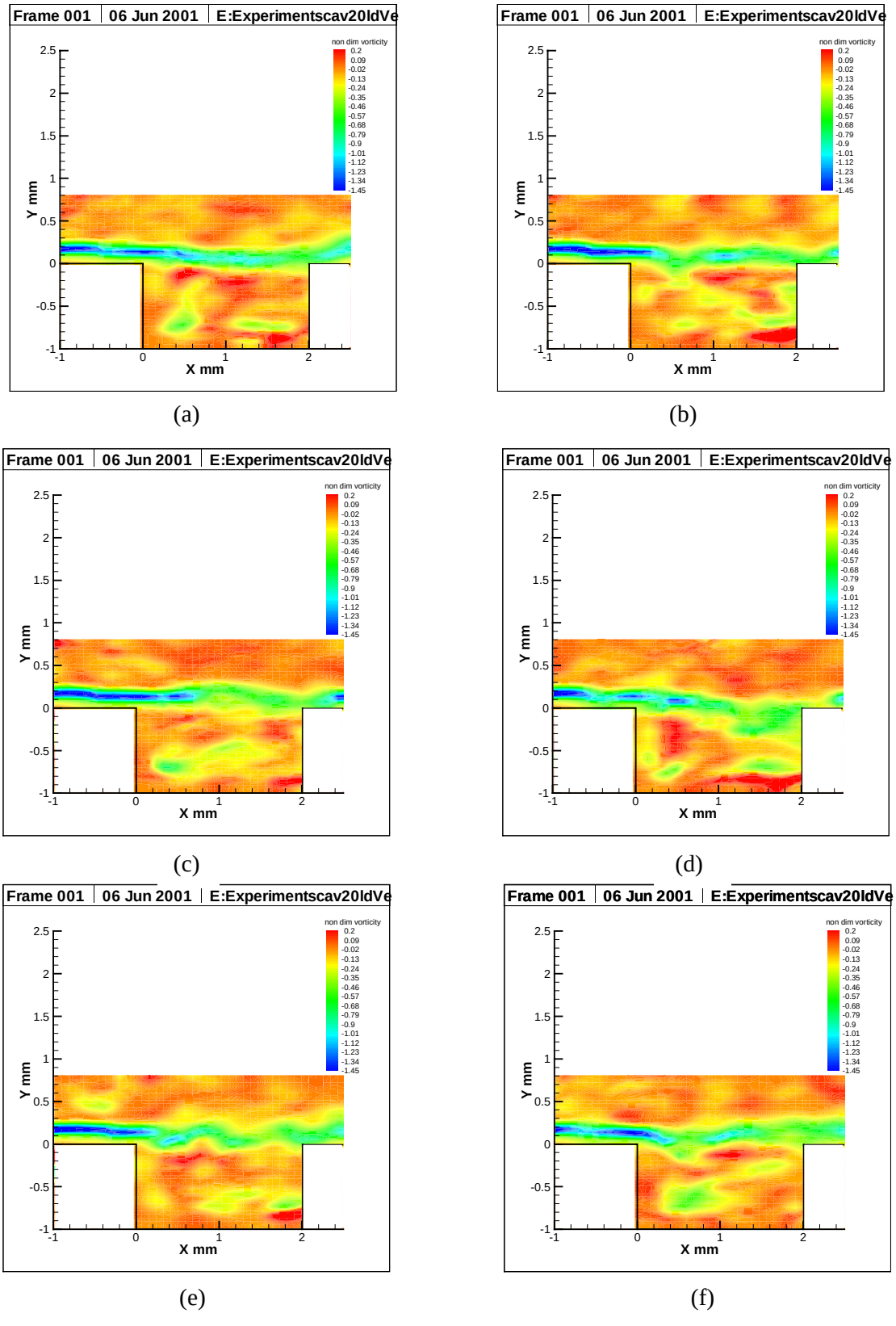

Figure 5.6 Experimental Non-Dimensional Vorticity (ωD/U) Contours, Cavity L/D = 2.0, U = 64 m/s [33]

The code employs a second-order-accurate method for solving the compressible Navier-Stokes equations for two-dimensional cavities with boundary layers obtained from experiments specified upstream of the cavities. Time integration was performed using the Crank-Nicholson scheme. A Cartesian grid was used, with clustering of nodes near the walls. Quadratic power law mappings were used for grid stretching. To speed up convergence, a quiescent initial condition was imposed inside the cavity. A computational pressure monitor was placed on the floor of the cavity near the trailing edge corresponding to the position of the microphone in the experiments. The position of the pressure monitor for cavity L/D = 2.0 is shown in figure 5.7. Spectral analysis was performed on the computational pressure data in order to compare it with the spectrum obtained from the experiments. The turbulent boundary layer profile obtained from experiments was specified as the inlet boundary condition and ambient conditions were imposed as the outlet boundary condition. The grid and computational domain used for the open cavity is shown in figure 5.8.

Test runs showed that the use of a turbulence model added additional dissipation to the code due to eddy viscosity that damped out the weak self-sustained oscillations that are characteristic of cavity flows at these low speeds. In order to retain the undamped self-sustained oscillations, a laminar flow calculation was performed with the turbulent boundary layer profile specified as the inlet boundary condition. The results of the two-dimensional laminar flow computations are given below.

5.1.5 Computational Pressure Data

Figure 5.9 is the time history of the computed pressure signal on the floor of cavity L/D = 2.0 at a freestream velocity of 64 m/s. The time history record shows that the instability becomes self-sustained and weakly coherent in phase after a time of approximately 0.04 s.

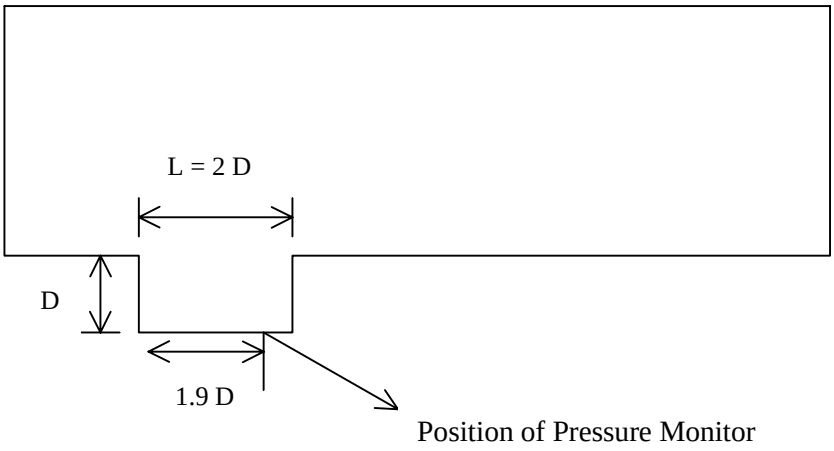

Figure 5.7. Position of Computational Pressure Monitor for Cavity L/D = 2.0, D = 0.019 m

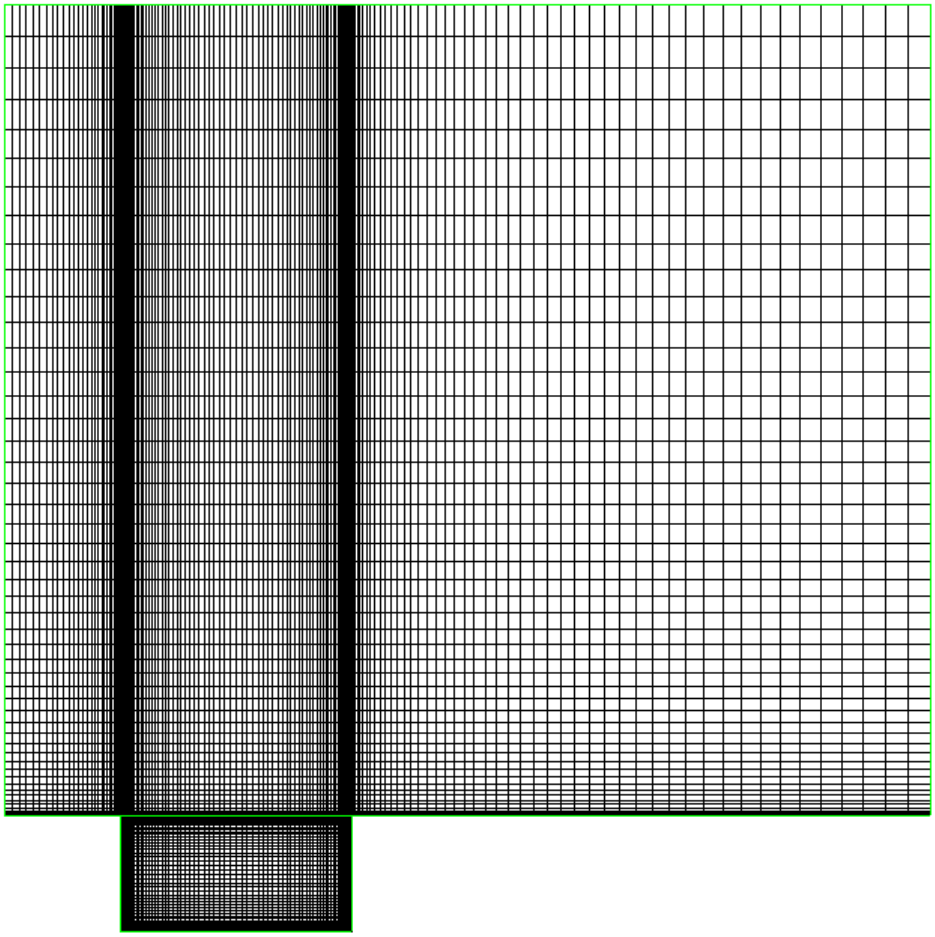

Figure 5.8. Typical Computational Domain, Cavity L/D = 2.0

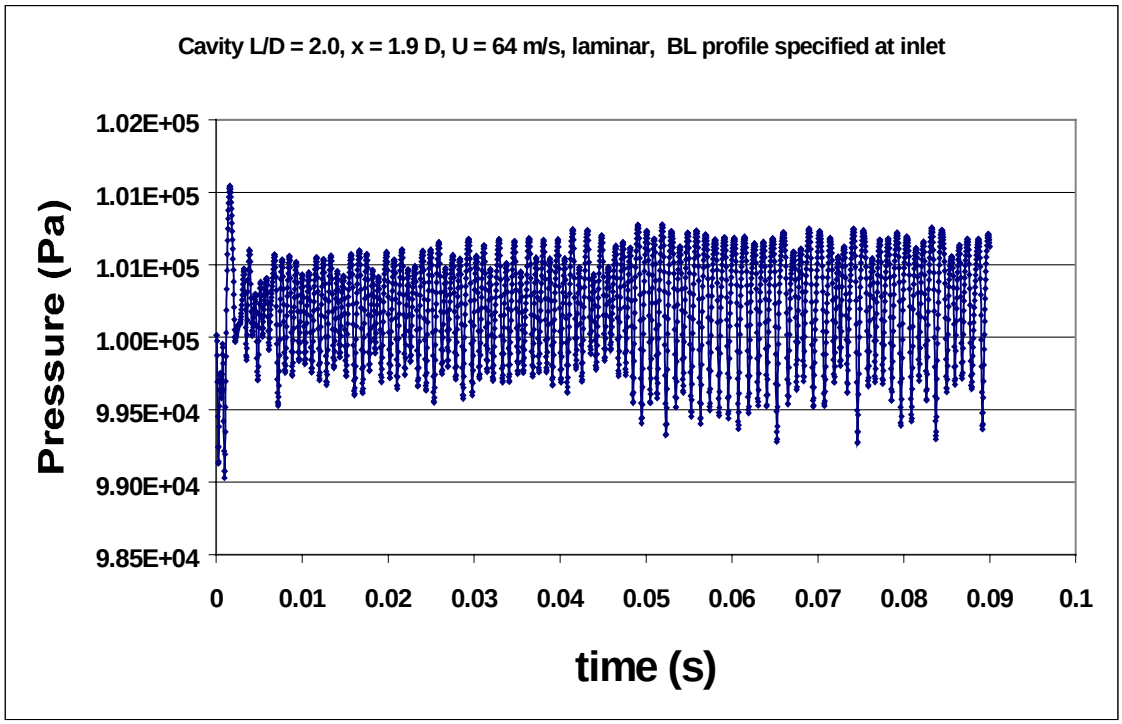

Figure 5.9 Computed Time History of Pressure Signal on Cavity Floor, Cavity L/D=2.0, U = 64 m/s

The fundamental cavity mode is at a frequency of 1026 Hz as observed from the spectrum shown in figure 5.10. This value agrees to within 120 Hz of the experimental value of 906 Hz(figure 5.2). However, the amplitude of the computational peak is at 134 dB as compared to 90 dB obtained from the experimental data. This difference of about 44 dB or two orders of magnitude difference in the SPL peak is attributed to the fact that the numerical simulation is laminar, thus unaffected by additional viscosity effects, whereas the cavity flow is turbulent in reality. Also seen from figure 5.10 is that the second mode of oscillation lies at a frequency of 1675 Hz as compared with an experimental value of 1988 Hz(figure 5.2). The value of the computational peak is 127 dB and experiments yield a SPL of 98 dB. Another fact gleaned from figure 5.10 is that the first mode of oscillation is dominant for the computed pressure history, whereas experiments show that the second mode of oscillation is dominant.

Since the laminar two-dimensional computational runs made for cavity L/D = 2.0 at U = 64 m/s were able to simulate the frequencies of the weakly coherent self-sustained oscillations obtained from experimental data, it was decided that a comparison of the computational and experimental velocity and non-dimensional vorticity fields would yield a worthwhile comparison.

5.1.6 Computed Velocity and Vorticity Results

5.1.6.1 Cavity L/D = 2.0, U = 64 m/s

The computed instantaneous velocity vector fields for cavity L/D = 2.0 at a freestream velocity of 64 m/s are shown in figures 5.11. The six vector plots represent two cycles of the cavity oscillation mechanism. The vectors show the shear layer oscillating near the trailing edge, and two large contra-rotating re-circulation zones occupying the inside of the cavity. This is unlike the one re-circulation zone as seen from experiments (figure 5.4(a-f)) and is due to the fact that the numerical results are based on a laminar flow model whereas in reality the cavity flow mechanism is being driven by a relatively dissipative turbulent shear layer. The vectors also show

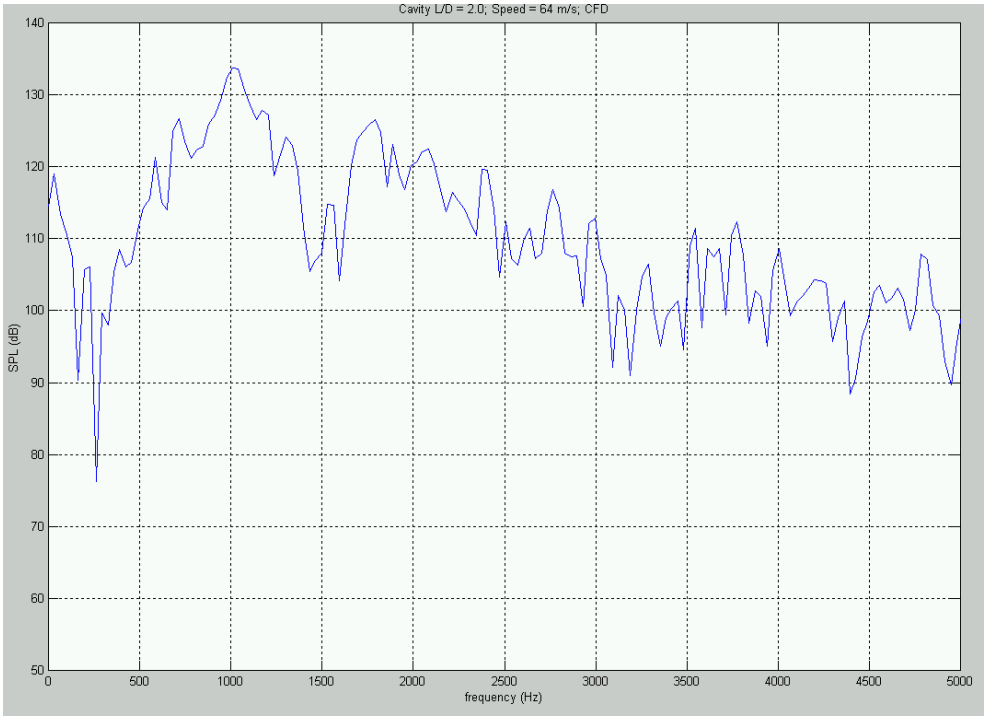

Figure 5.10 Power Spectrum of Pressure Signal on Floor of Cavity, L/D = 2.0, U = 64 m/s

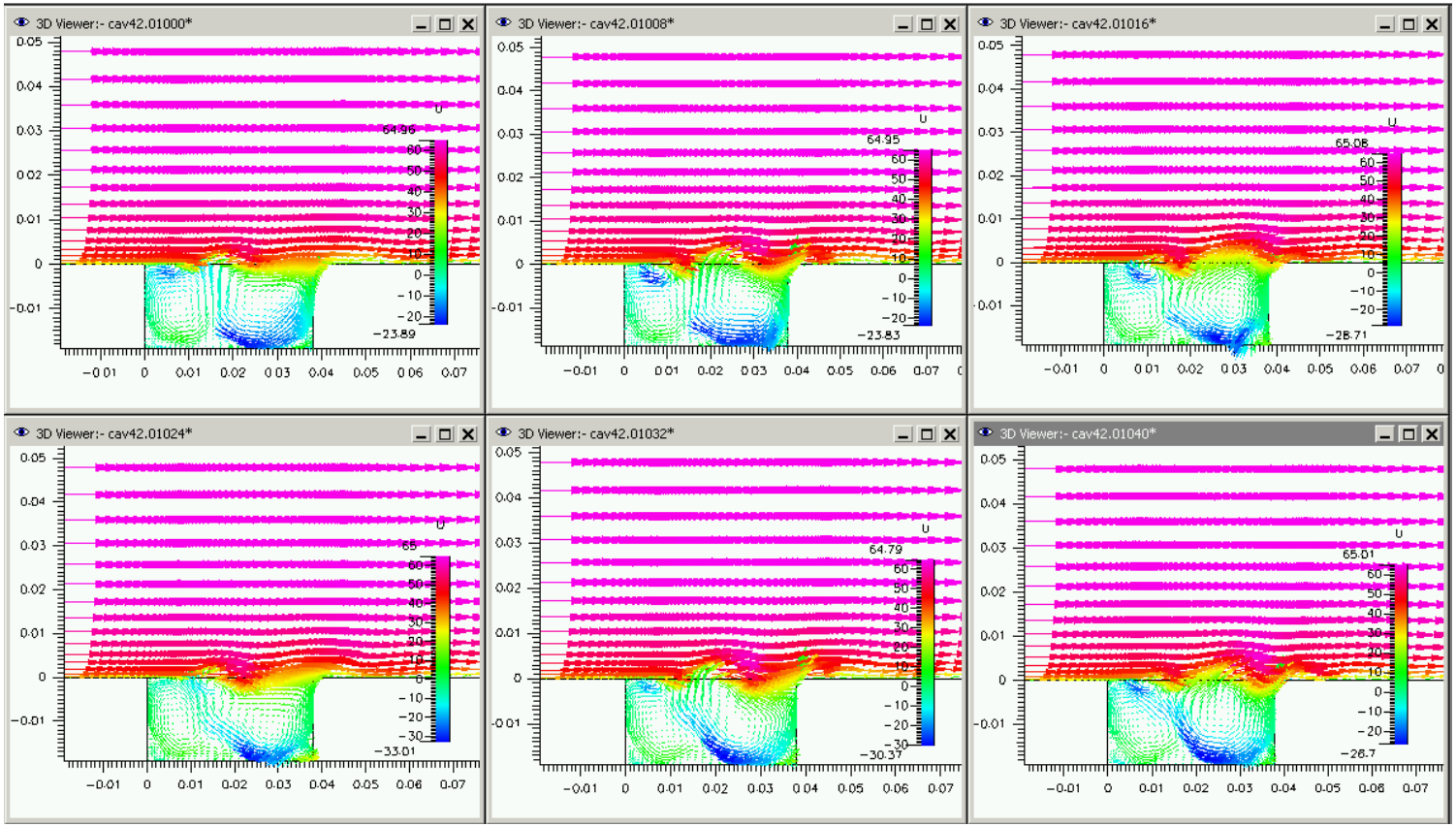

Figure 5.11 Computed Velocity Vectors, Cavity L/D = 2.0, U = 64 m/s

the production of a vortex at the leading edge of the cavity, its convection downstream, and interaction with the trailing edge in accordance with the observations made from the experimental results. The speed inside the cavity reaches up to 50% of the freestream velocity unlike the 25% of freestream as seen from the experimental results. The velocity contours shown in figure 5.12 clearly show the production and downstream convection of a vortex from the leading edge, in addition to the shear layer oscillation near the trailing edge of the cavity.

Figures 5.13 are the contour plots of the non-dimensionalized vorticity (ndv) of the cavity configuration. The range of the contour and the contour levels were set such that they matched exactly with that of the experimental data. The non-dimensional vorticity plots reconfirm the mechanism of the cavity oscillations as seen in the velocity vector and contour plots.

5.1.7 Summary of Comparison

Meganathan's experimental data for open cavity flows at low subsonic speeds was compared with the results predicted by numerically simulated laminar, two-dimensional open cavity flows. Numerical simulation was able to produce sustained undamped cavity oscillations near the trailing edge of the cavity as observed from experiments. The computed frequencies of oscillation were in good agreement with the experimental data. Both experiments and numerical results agreed poorly with the Rossiter's predicted frequencies. The computed magnitude of oscillations was at least 40 dB higher than that observed in experiments. This was due to the fact that the computation was laminar, whereas the experimental results were driven by a relatively dissipative turbulent shear layer. The numerically simulated velocity and non-dimensional vorticity plots exhibit the oscillation of the shear layer, and the mechanism of the cavity oscillation as seen in the experiments.

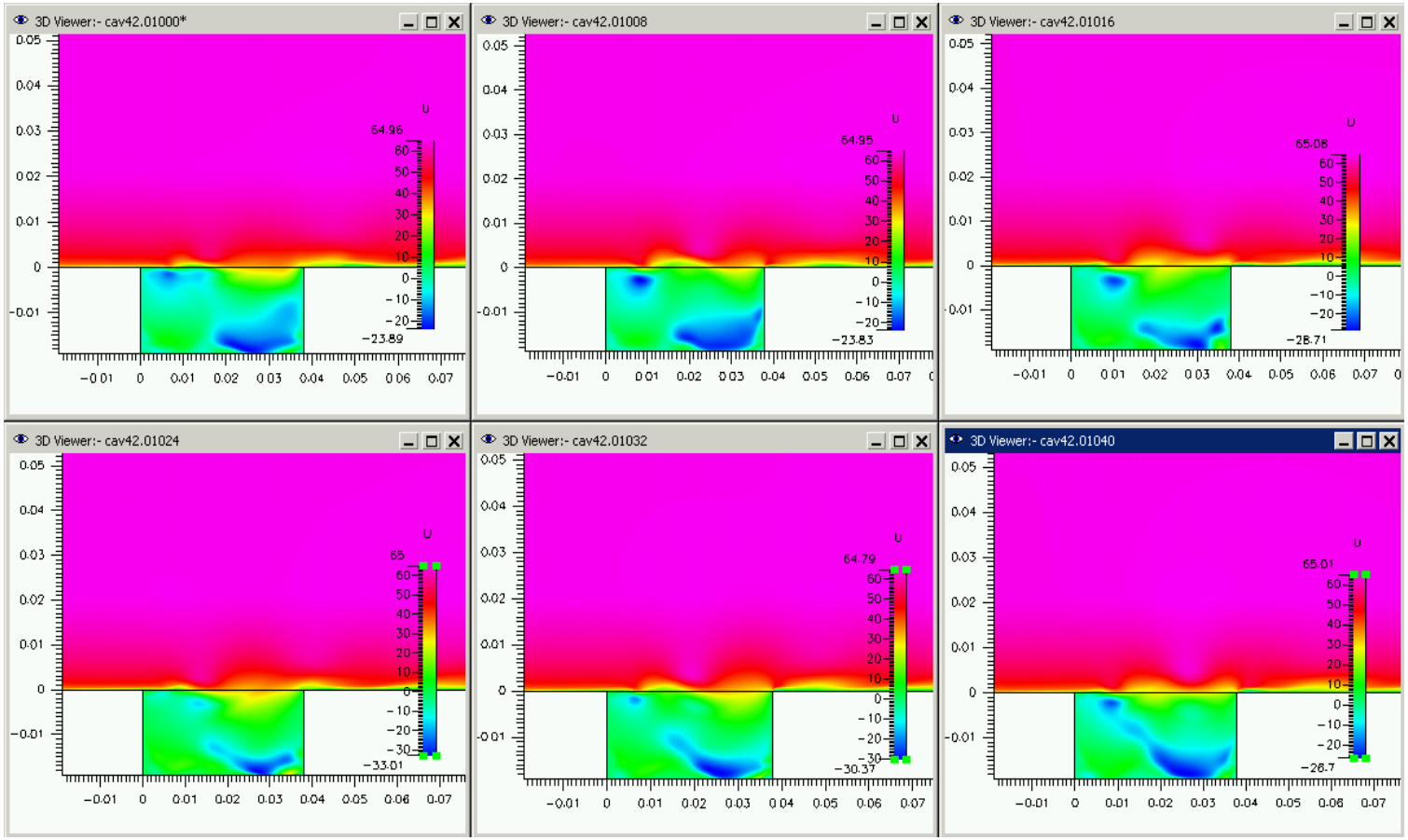

Figure 5.12 Computed Velocity Contours, Cavity L/D = 2.0, U = 64 m/s

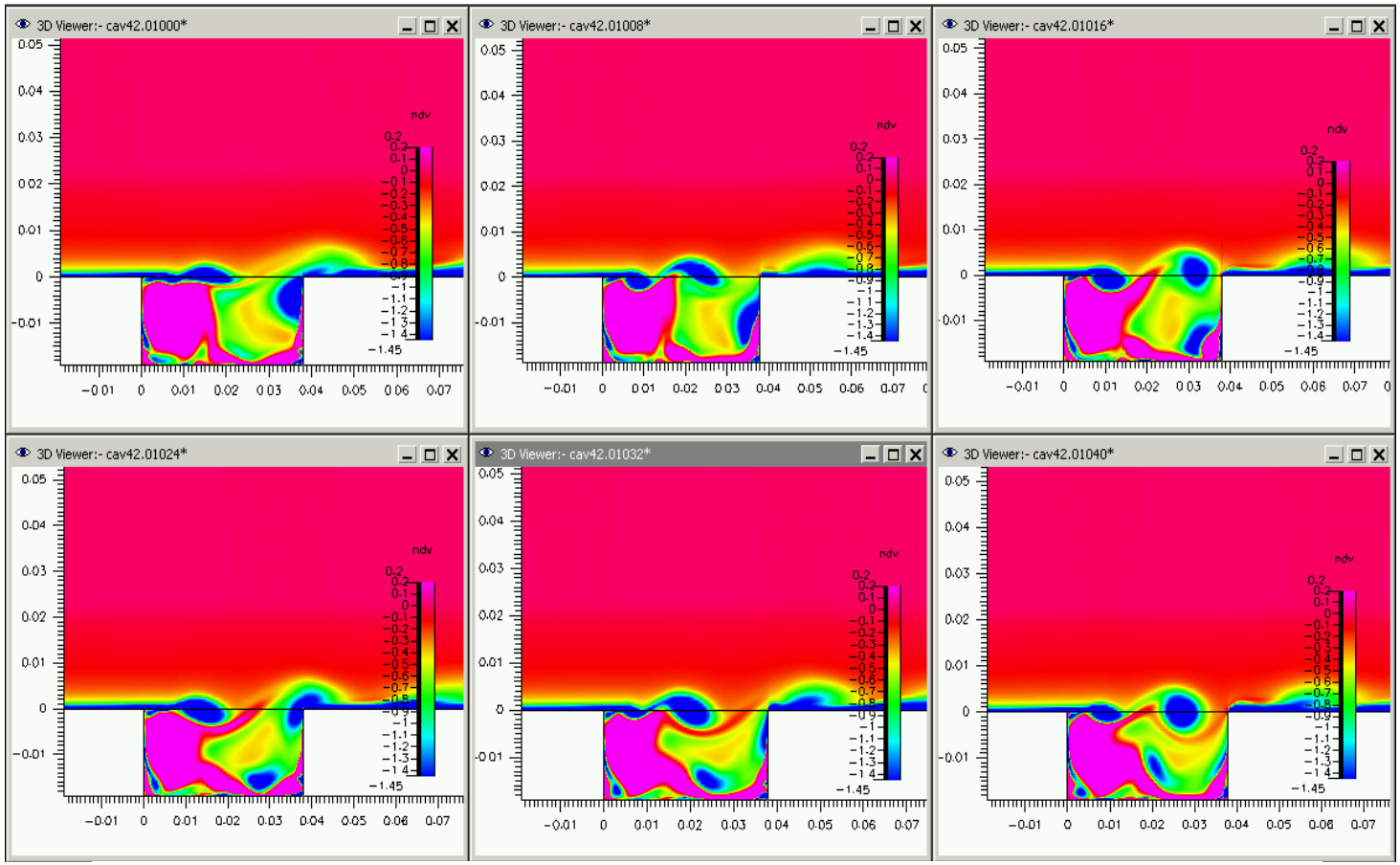

Figure 5.13 Computed Non-Dimensional Vorticity Contours (ωD/U), Cavity L/D = 2.0, U = 64 m/s

These computations capture the essential features of open cavity flows, thus serving as a useful starting point for computations to be made for cavity flows at high subsonic speeds. The following sections describe comparison of experimental and numerical results obtained for high speed subsonic cavity flows.

5.2 High Speed Wind Tunnel Cavity Data and Comparison with Numerical Simulations

Experiments were performed in the UTSI High Speed Wind Tunnel (HSWT) with the same model for cavity L/D ratios of 2.0, 2.5, 3.5, and 4.0 for freestream speeds ranging between 70 m/s to 210 m/s. Dynamic pressure measurements were obtained on the floor of the cavity using dynamic pressure transducers. Global velocity fields were measured using Particle Image Velocimetry (PIV).

Numerical simulations performed with CFD-ACE(U)® were compared with the data obtained from experiments. Results are presented for Cavity L/D ratios 2.5 and 4.5 respectively.

5.2.1 Dynamic Pressure Measurements

To ensure that the Sound Pressure Level peaks generated by the cavity are indeed produced by the cavity, and are not present in the empty tunnel configuration, the empty tunnel was run between Mach numbers of M = 0.25 to M = 0.64. The dynamic pressure transducer was positioned on the floor of the empty tunnel. The spectra of the empty tunnel is shown in Figure 5.14. This figure will be used to compare with the SPL peaks measured by the cavities installed in the tunnel.

Figure 5.15 (a-h) plots the spectra of the dynamic pressure data on the floor of the cavity of L/D ratio 2.5 for Mach numbers ranging from 0.22 to 0.64. The dynamic pressure transducer was located along the centerline of the cavity floor in the streamwise direction, and

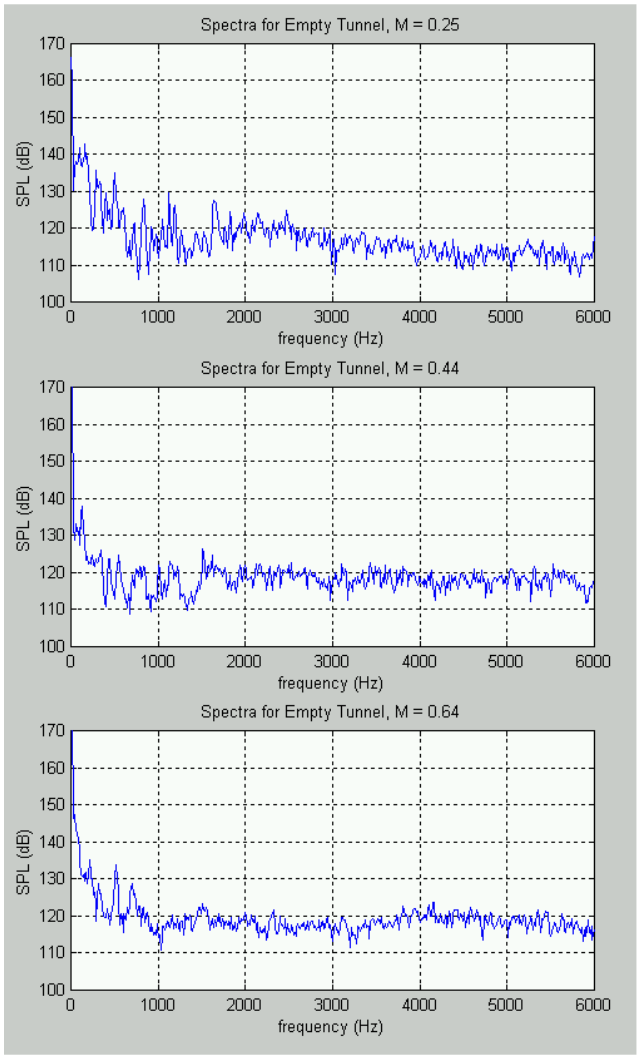

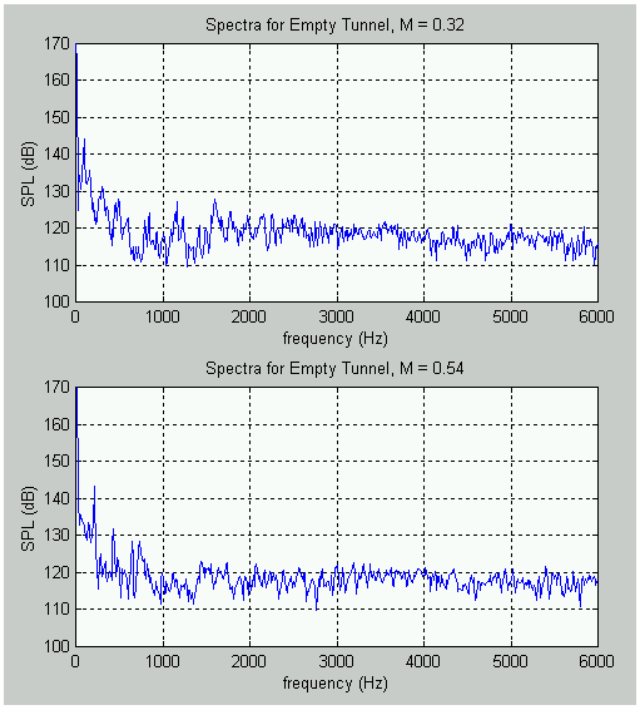

Figure 5.14 Power Spectra of Empty Tunnel

(a)

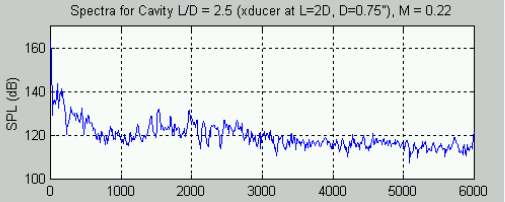

(b)

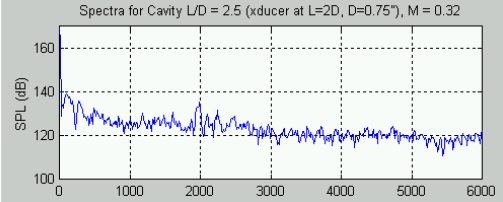

(c)

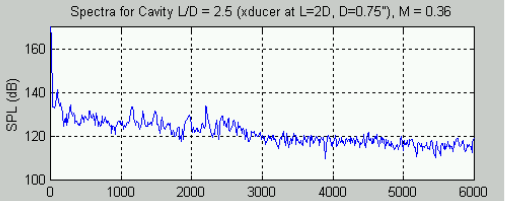

(d)

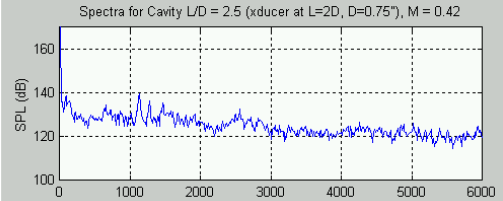

(e)

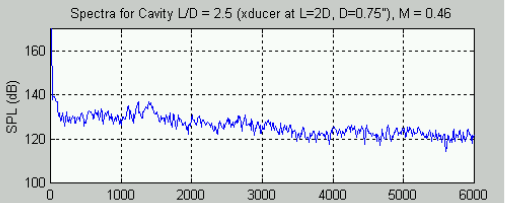

(f)

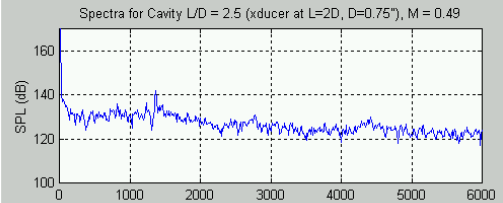

(g)

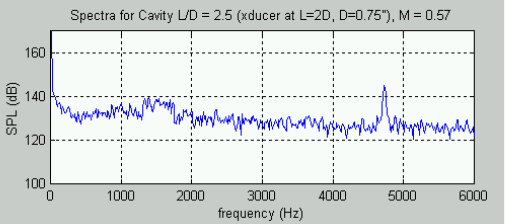

(h)

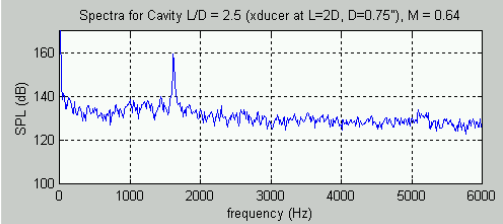

Figure 5.15 Spectra of Cavity L/D = 2.5

was at a distance of 1.5 inches (0.0381 m) from the leading edge of the cavity corresponding to a length L = 2D, where D, the depth of the cavity was equal to 0.75 inches (0.019 m). The spectra in figure 5.15 are plotted for speeds ranging from M = 0.22 to M = 0.64. The spectra show that weak Rossiter mode cavity peaks occur for speeds ranging between M = 0.32 to M = 0.49. The physical mechanism for this is believed to be the low levels of coherent vorticity in the shear layer at these speeds. This results in the formation of weak and non-coherent vortices that are convected downstream to interact with the forward facing step of the cavity. However, at M = 0.57 (figure 5.15 (g)), a well-defined peak of amplitude 143 dB is observed at a frequency of 4722 Hz. This peak corresponds to the third Rossiter mode of oscillation. Also, at M = 0.64 (figure 5.15 (h)), a sharp peak of amplitude 160 dB is noticed at a frequency of 1617 Hz that corresponds to the first Rossiter mode of oscillation. These well-defined peaks show the resonant interaction of the cavity with the flow as propounded by Rossiter. Another interesting observation is that mode switching occurs between M = 0.57 and M= 0.64. Mode switching is a result of the non-linear feedback coupling that occurs in cavity flows, and is a topic of active research. Comparison of the spectra for cavity L/D = 2.5 with the spectra produced by the empty wind tunnel (figure 5.14) show that the SPL peaks obtained for the cavity are indeed produced by the cavity, and are not modes that exist in the empty tunnel.

Figure 5.16 (a-j) plot the spectra of Cavity L/D ratio 4.5 for speeds between M=0.24 to M=0.62. Two dynamic pressure transducers at L = 2D and L = 4D (D=0.019 m) from the cavity leading edge respectively, were positioned on the floor of the cavity along its centerline in the streamwise direction. As expected, both transducers measure similar spectra. However, for a given Mach number, the transducer at L = 4D that is near the cavity trailing edge produces a higher level of background noise than the one at L = 2D. This is due to the proximity of the transducer at L = 4D to the cavity trailing edge. Figures 5.16 (i) and (j) show well defined SPL

(a)

(b)

(c)

(d)

(e)

(f)

(g)

(h)

(i)

(j)

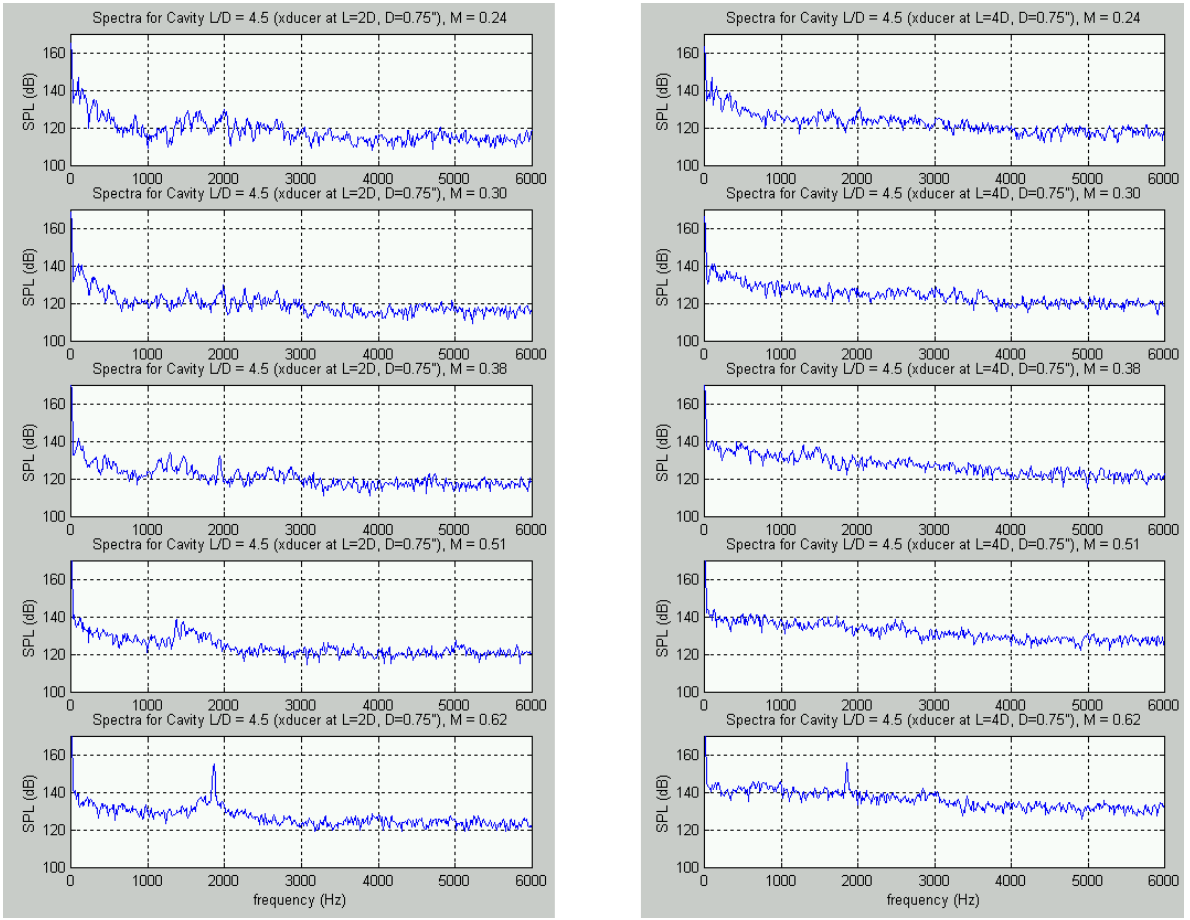

Figure 5.16 Spectra of Cavity L/D = 4.5

peaks for the two transducers at a frequency of 1863 Hz and an amplitude of 158 dB for M=0.62. These peaks correspond to the second mode of the Rossiter's prediction. For each spectrum, the amplitudes, frequencies and modes of the peaks were extracted, and the non-dimensional Strouhal number, St (fL/U), of the oscillations was calculated. These are compared to the modified Rossiter's formula

$$St = \frac{fL}{U} = \frac{m - n}{1/K_v + \frac{M_\infty}{\sqrt{1 + \frac{\gamma - 1}{2} M_\infty^2}}}$$

Figure 5.17 shows the comparison of the experimental data for cavity L/D = 2.0, 2.5, 3.5 and 4.5 with the Rossiter's formula. As seen in the figure, the agreement is very good, verifying that the cavities did not experience interferences in the tunnel.

5.2.2 Velocity Field Measurements

In the following sections, flow field data obtained by Particle Image Velocimetry (PIV) is presented for cavity L/D ratio of 2.5 with the freestream Mach numbers set at 0.4, 0.57 and 0.6 respectively. Velocity field data is also presented for cavity L/D ratio 4.5 for freestream Mach numbers of 0.4 and 0.6 respectively. The data is interpreted and analyzed using both instantaneous and averaged flow fields.

The instantaneous fields were obtained in sets of 15 image pairs taken at a rate of 15 frames/second. The time interval between two images in each image pair was set to 1μs. The instantaneous flow fields presented in the following sections were chosen randomly from one set of 15 image pairs. This implies that no phase reference or phase trigger was employed in the image acquisition process.

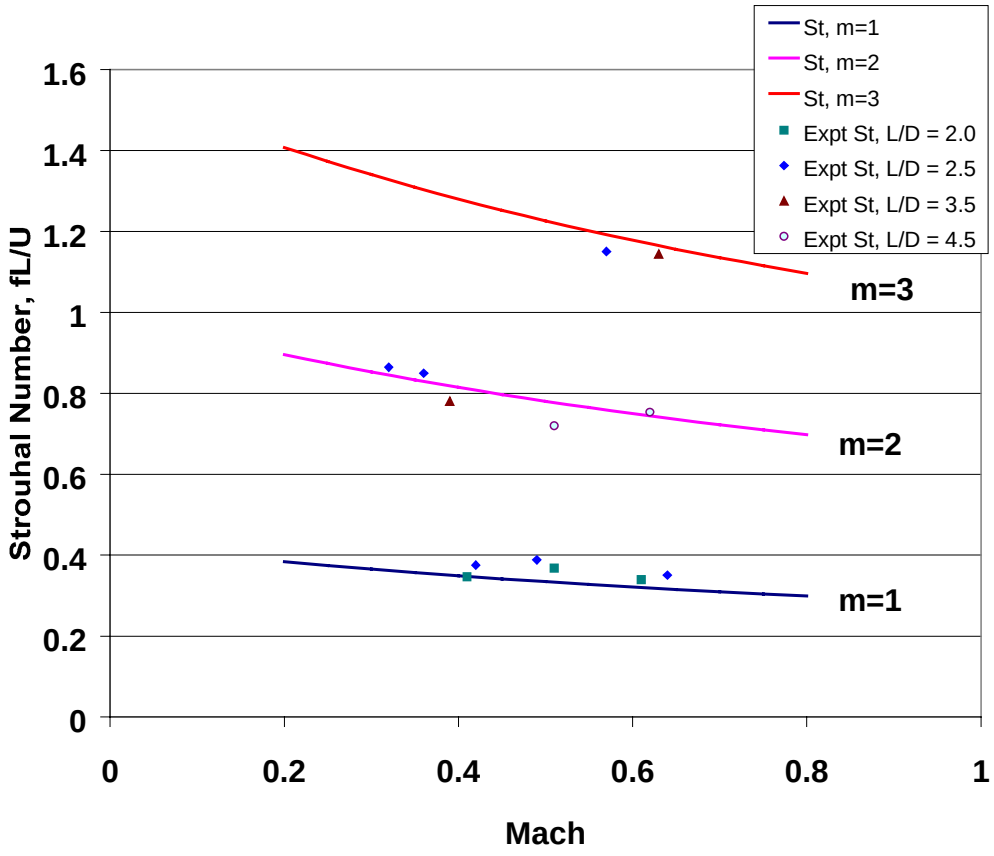

Figure 5.17 Comparison of Experimental Data with Rossiter's Semi-Empirical Formula

The PIV images of the flow near the walls were affected by the reflected glare and hence not enough seeds were visible to the CCD camera. This is the reason why there is a narrow region near the cavity walls where there is no velocity field data available.

For each flow condition, at least 70 vector fields were averaged to calculate a parameter at a given location (x,y). Averaged flow fields were used to calculate the turbulence intensity and Reynolds Stress values over the measured velocity field.

5.2.2.1 Boundary Layer Measurements

The boundary layer approaching the cavity was measured 0.5 inches (0.0127 m) upstream of the leading edge corner of the cavity. Figure 5.18 shows the boundary layer profile for a freestream Mach number of 0.4. The Reynolds number based on the length of the flat plate leading to the cavity was about 1.9×10^6. The boundary layer thickness $\delta_{0.99}$ for this velocity profile was measured as 6.93 mm. The turbulent boundary layer expression yielded a boundary layer thickness of 4.98 mm. The displacement thickness and momentum thickness were calculated by fitting a parabolic profile between zero (point on the wall) and the two points measured closest to the wall.

Figures 5.19 and 5.20 show the boundary layer profiles measured at M = 0.57 and M = 0.6 respectively. Table 5.1 summarizes the boundary layer data for all the three Mach numbers. The decreasing values of momentum thickness for increasing Mach numbers indicates the presence of higher values of kinetic energy in the boundary layer as the Mach number goes up. The comparison of measured boundary layer thickness with theoretical boundary layer thickness showed that the flow approaching the leading edge of the cavity was fully turbulent for all the three Mach numbers.

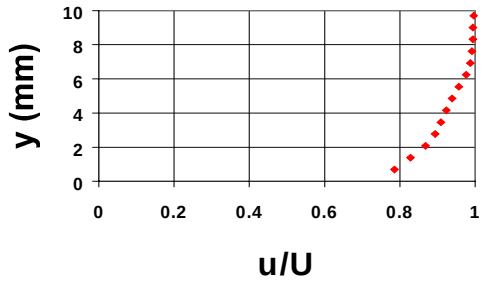

Figure 5.18 Boundary Layer Profile, Mach = 0.4

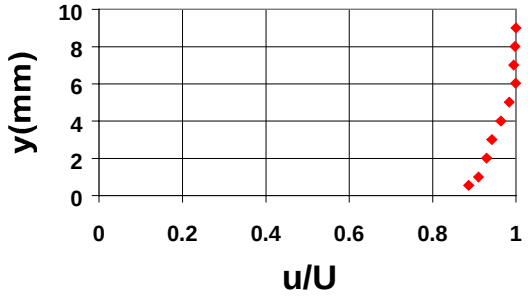

Figure 5.19 Boundary Layer Profile, Mach = 0.57

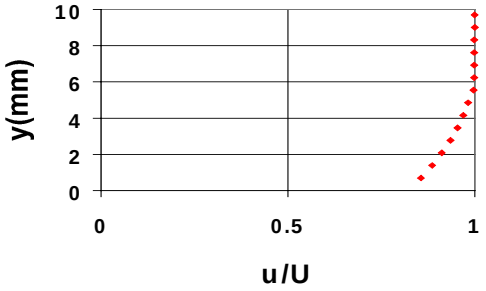

Figure 5.20 Boundary Layer Profile, Mach = 0.6

Table 5.1 Summary of Boundary Layer Parameters

Mach	Re (million)	Measured δ (mm)	Measured δ (D)	Theoretical δ (mm)	δ^* (mm)	θ (mm)	H
0.4	1.93	6.93	0.36	4.98	0.85	0.79	1.08
0.57	2.96	6.03	0.32	4.65	0.72	0.68	1.06
0.6	3.27	5.54	0.29	4.59	0.62	0.60	1.03

5.2.2.2 PIV Results, L/D = 2.5, M = 0.4

Figure 5.21(a-f) plots the instantaneous non-dimensional vorticity contours for cavity L/D = 2.5 with the freestream Mach number set at 0.4. The vorticity contours show that the shear layer is primarily made up of two scales of vortical structures. Immediately downstream of the leading edge of the cavity, the vorticity concentration is very high, indicating that small scale, highly coherent vortical structures are formed that have a high value of vortex passage frequency. The presence of these small scale structures indicate that this region is highly turbulent with a large rate of mixing. As these small-scale structures move downstream, they coalesce together to form larger vortical structures that scale with the cavity length. Vortex merging causes the shear layer to spread and the vortex passage frequency to decrease. However, the plots indicate that the vortices are not well organized in the shear layer. This observation suggests a lack of coherence among the vortical structures, and could be an indication as to why the power spectrum of the pressure signal did not exhibit a well-defined SPL peak at this Mach number (Figure 5.16 (d)). The interaction of the large vortical structures with the trailing edge of the cavity is widely recognized [5] to be associated with the generation of upstream influences that modulate the shear layer at the cavity leading edge. However, it is apparent from the vorticity contours that there exists only a relatively weak interaction of the large vortical structures with the trailing edge of the cavity.

The instantaneous velocity vectors plotted in Figures 5.22 (a-f) show the existence of a wall jet like flow adjacent to the lower half of the trailing edge that is oriented towards the floor of the cavity. A similar wall jet like flow is encountered near the floor of the cavity that extends well upstream of the trailing edge. This jet adjacent to the floor then turns in the upward direction over a short distance to feed the large entrainment demands of the shear layer. This jet plays an important role in modulating the shear layer at the leading edge of the cavity. Whenever the jet travels to the leading edge of the cavity in phase with the upstream traveling acoustic wave

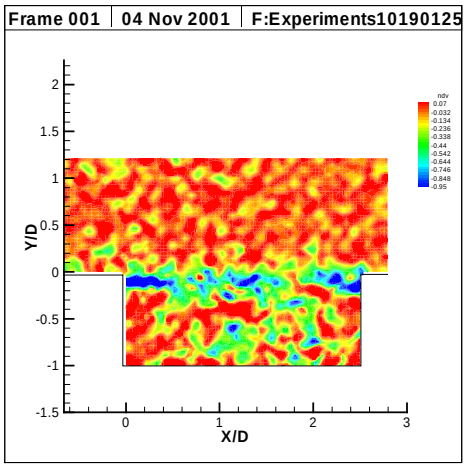

(a)

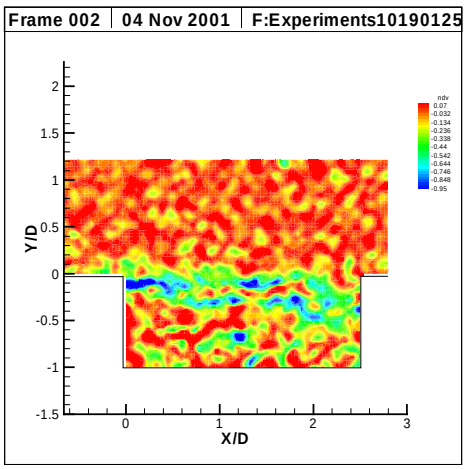

(b)

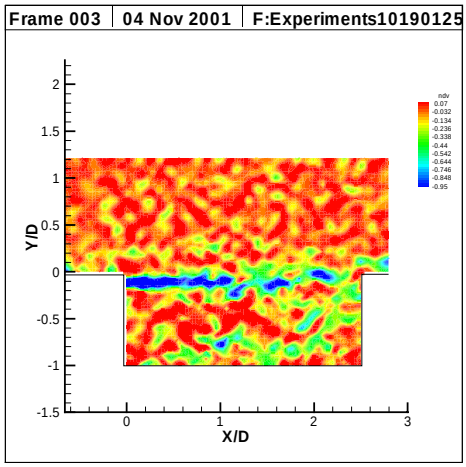

(c)

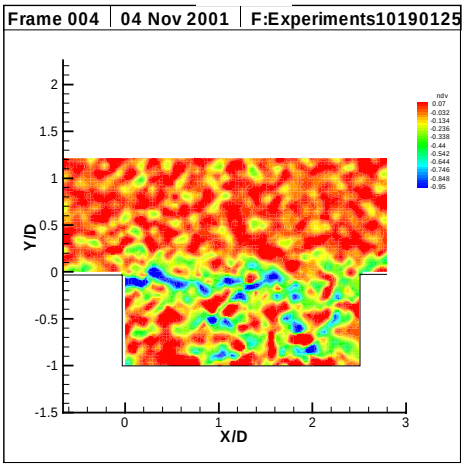

(d)

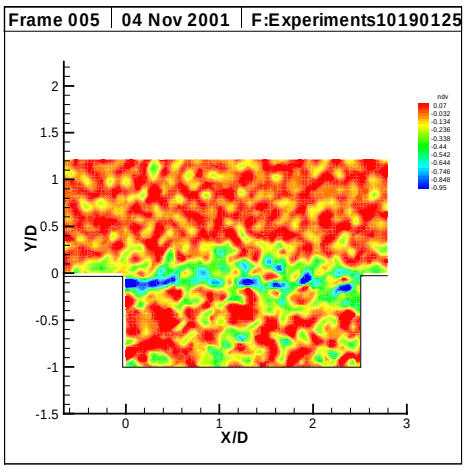

(e)

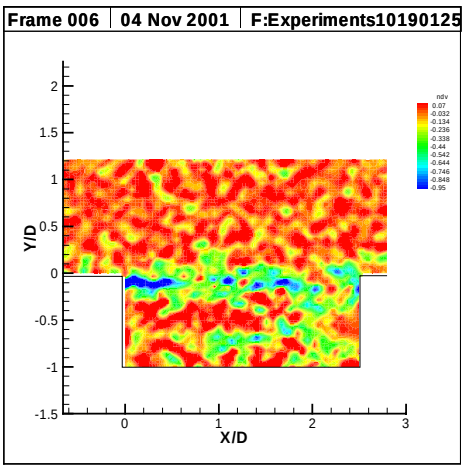

(f)

Figure 5.21 Instantaneous Non-Dimensional Vorticity Contours, Cavity L/D = 2.5, M = 0.4

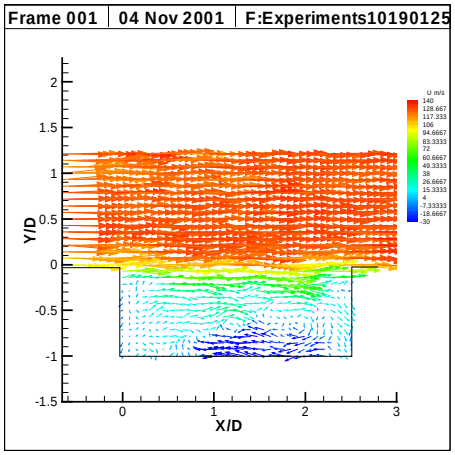

(a)

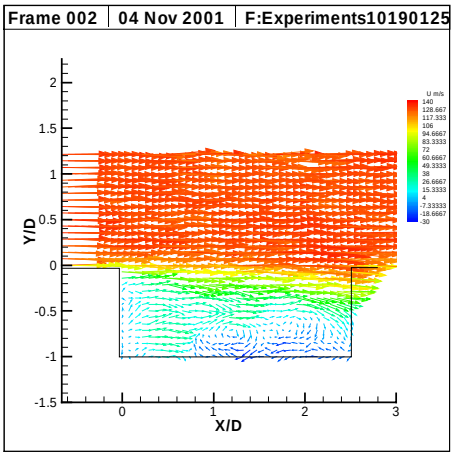

(b)

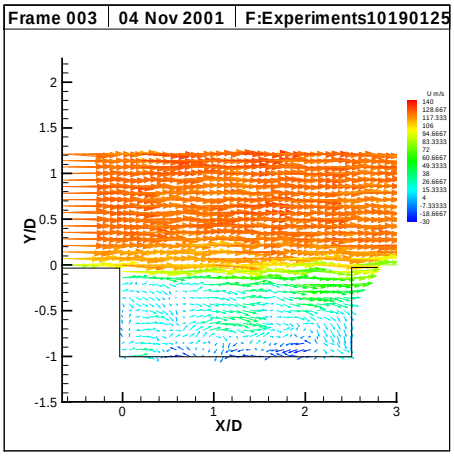

(c)

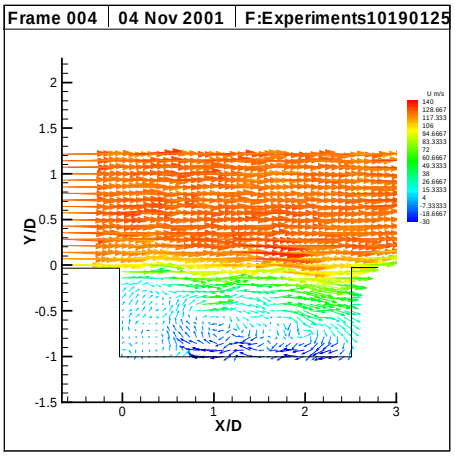

(d)

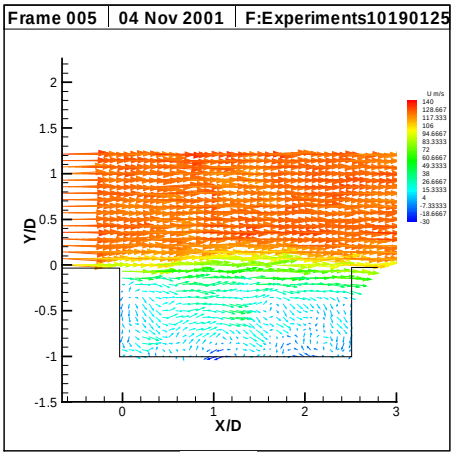

(e)

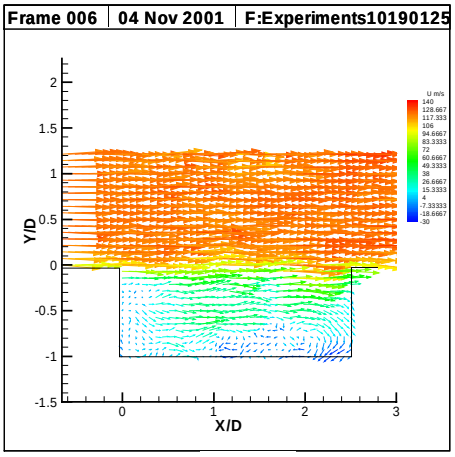

(f)

Figure 5.22 Instantaneous Velocity Vector Fields, Cavity L/D = 2.5, M = 0.4

produced at the cavity trailing edge, the convective and acoustic modes of the cavity interfere constructively to exhibit resonance. Cavity resonance is characterized by large changes in the amplitude of the shear layer disturbance.

The velocity vectors in Figure 5.22 (a) show an upward oriented outflow of fluid at the trailing edge corner. This outflow is associated with the arrival of the cluster of vorticity as seen in Figure 5.21 (a). On the other hand, Figure 5.22 (b) plots the downward oriented inflow of fluid at the trailing edge corner. This is the basis of the pseudo-piston theory put forward by Heller and Bliss [6] in which they consider a massless piston at the trailing edge periodically entraining and ejecting fluid mass that causes the cavity pressure oscillations. Two recirculating zones can be observed within the cavity and they tend to occupy the right half of the cavity. These recirculating zones are not stationary, and they interact with the vortical structures in the shear layer to cause variations in the inflow and outflow of fluid mass. Figures 5.23 (a-f) show the velocity contours corresponding to the velocity vectors plotted in Figures 5.22 (a-f). The velocity contours clearly demonstrate the oscillation of the shear layer with mass entrainment and ejection at the trailing edge of the cavity. Animation of the velocity contours show that the shear layer oscillates even at the separation point. However, the amplitude of oscillation at the trailing edge is higher indicating the interaction of the recirculation zones that are located in the right half of the cavity with the shear layer.

Figures 5.24(a) shows the averaged velocity vectors for the given flow conditions. Many of the features that were observed in the instantaneous velocity vector plots can also be observed in the averaged velocity plot. The mean velocity profile clearly shows the growth and spreading of the shear layer along the length of the cavity. The jet like flow near the cavity trailing edge wall, the cavity floor and near the leading edge region can be noticed in the mean velocity profile. The existence of two recirculating zones that occupy the right half of the cavity can also be observed from the plot. The mean non-dimensional vorticity contours shown in Figure 5.24 (b)

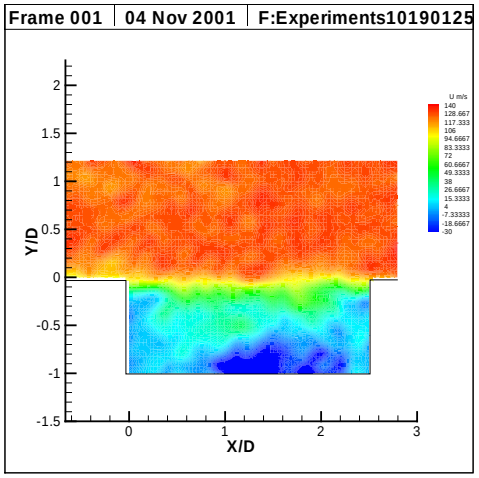

(a)

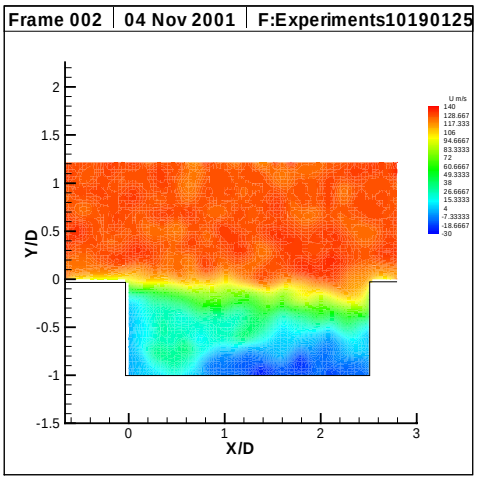

(b)

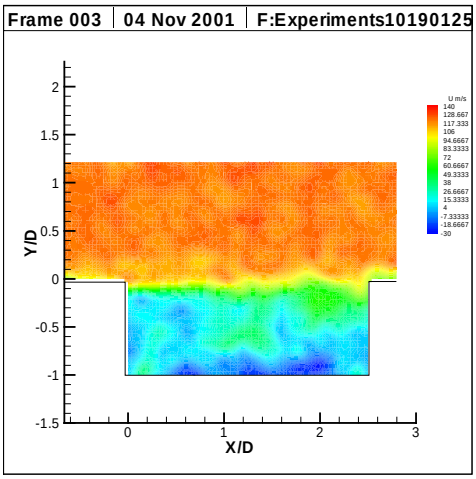

(c)

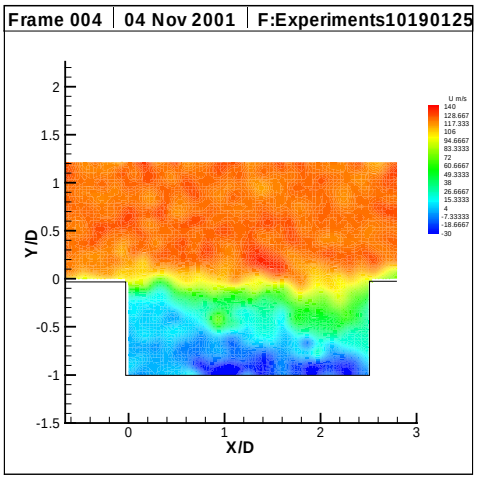

(d)

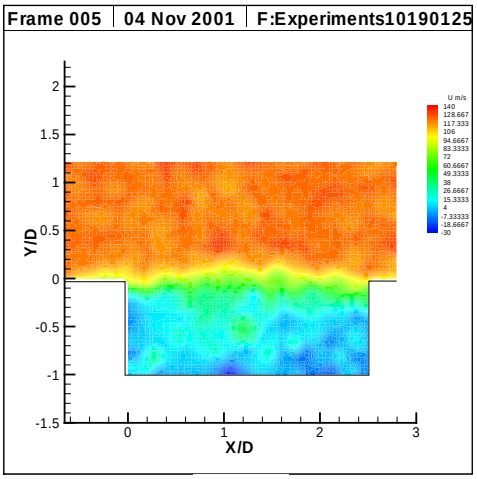

(e)

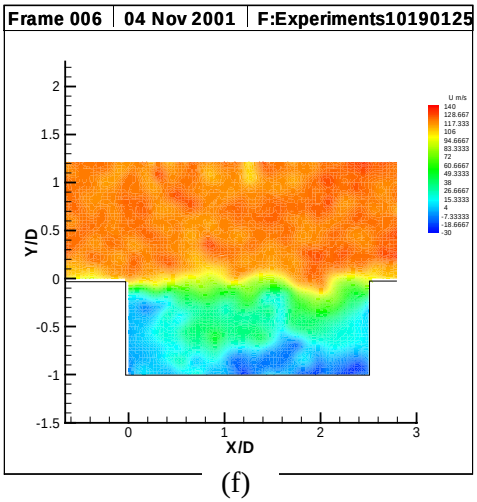

(f)

Figure 5.23 Instantaneous Velocity Contours, Cavity L/D = 2.5, M = 0.4

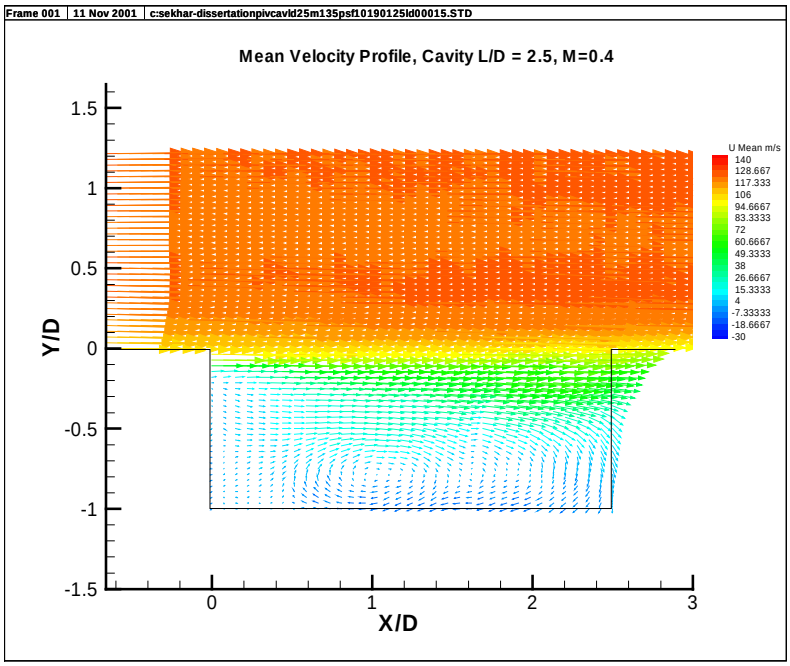

(a)

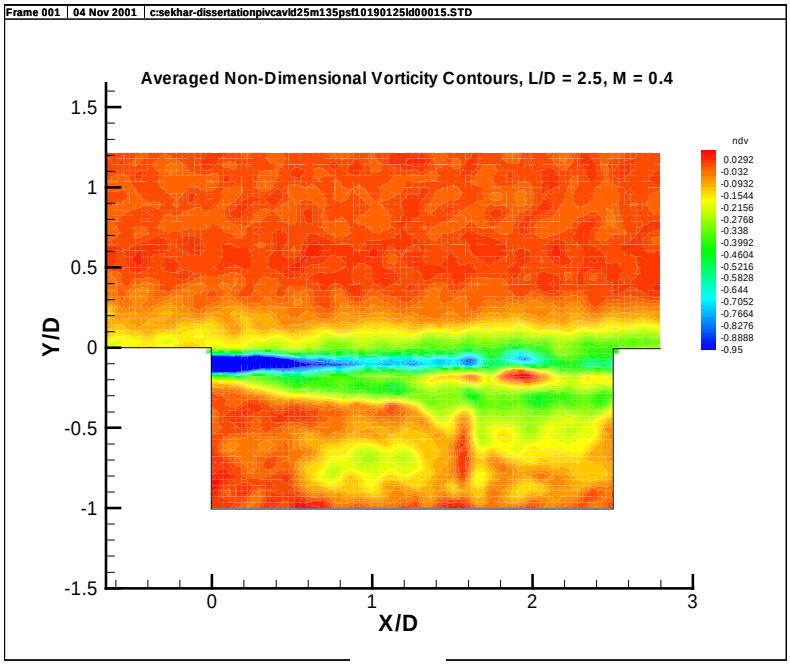

(b)

Figure 5.24 Averaged Velocity and Vorticity Field, Cavity L/D = 2.5, M = 0.4, (a) Velocity Vectors, (b) Vorticity Contours

confirm the spreading of the shear layer along the length of the cavity, and the high concentration of vorticity just downstream of the leading edge of the cavity. The green colored contours inside the cavity that represent a non dimensional vorticity value of about –0.2156 correspond to the vorticity associated with the strong recirculation zone seen in the averaged velocity vector plot (figure 5.24 (a)). The relatively weaker recirculation zone to its right is separated by a region of low vorticity that is represented by the red contours with a value of about 0.0292.

Figure 5.25 (a) plots the turbulence intensity for cavity L/D = 2.5 at freestream M = 0.4. The turbulence contours show freestream turbulence intensity upstream of the cavity leading edge to be about 5% and relatively high values of turbulence intensity in the shear layer and inside the cavity. Figure 5.25 (b) shows a contour plot of the Reynolds stress, normalized by the square of the freestream velocity. The red contours with a Reynolds stress value of about 0.005 in the shear layer indicate the high levels of vorticity present in the shear layer. As expected, the freestream has a zero value of Reynolds stress. The plot also exhibits the separation of the two recirculation zones by a region of approximately zero Reynolds stress.

5.2.2.3 PIV Results, L/D = 2.5, M = 0.57

As noticed from the power spectrum for cavity L/D = 2.5 (Figures 5.15(g-h)), the flow interaction with the cavity undergoes a mode switch with the primary SPL peak moving from a frequency of 4722 Hz at M = 0.57 to a frequency of 1617 Hz at M = 0.64. The SPL peak at 4722 Hz corresponded to the third Rossiter mode of oscillations and the SPL peak at 1617 Hz corresponded to the first Rossiter mode of oscillations for the given cavity geometry and flow conditions. In order to study the mechanism underlying the mode switch, PIV measurements were made were made for freestream Mach numbers of 0.57 and 0.6 respectively. The following paragraphs describe the PIV velocity field data for cavity L/D = 2.5 with the freestream Mach number set at 0.57.

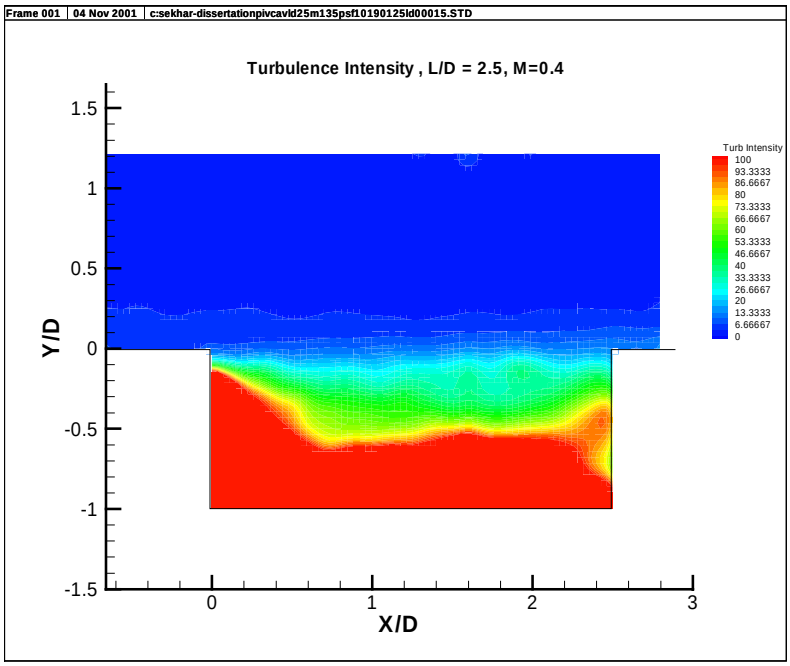

(a)

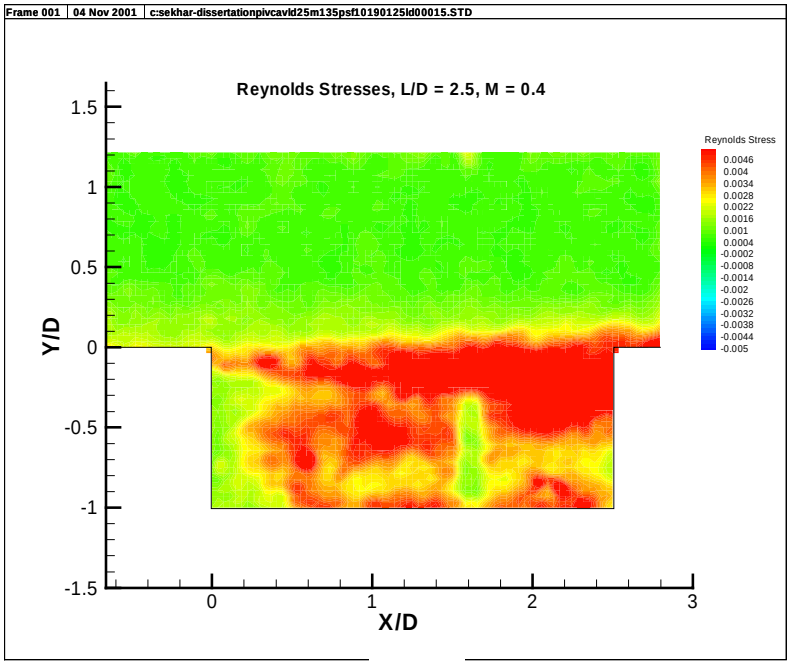

(b)

Figure 5.25 Averaged Velocity Fluctuations and Reynolds Stress, Cavity L/D = 2.5, M = 0.4, (a) Velocity Fluctuations (Turbulence Intensity), (b) Reynolds Stress

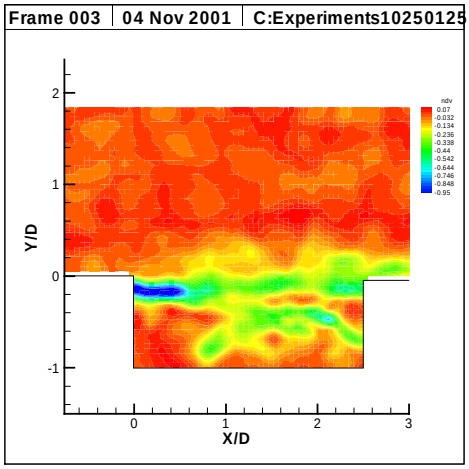

(a)

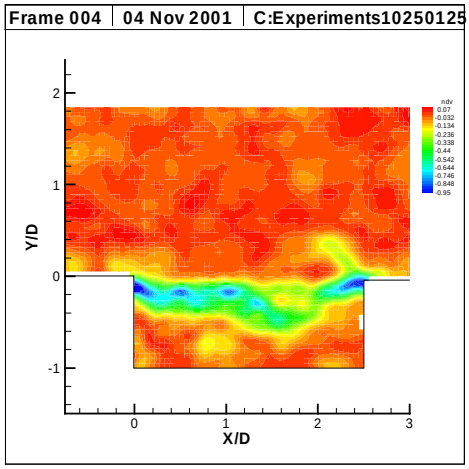

(b)

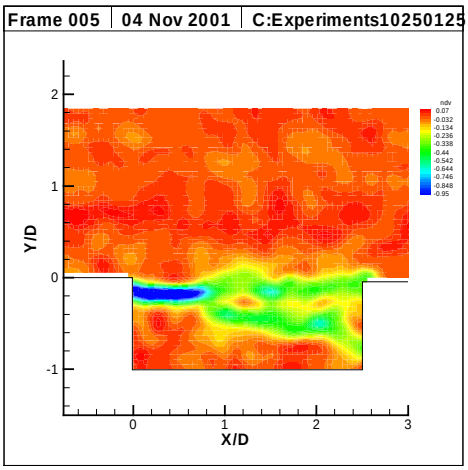

(c)

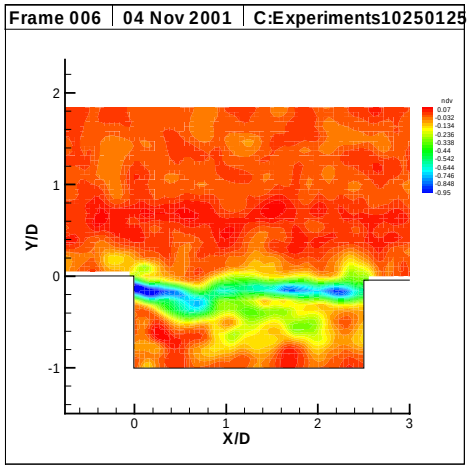

(d)

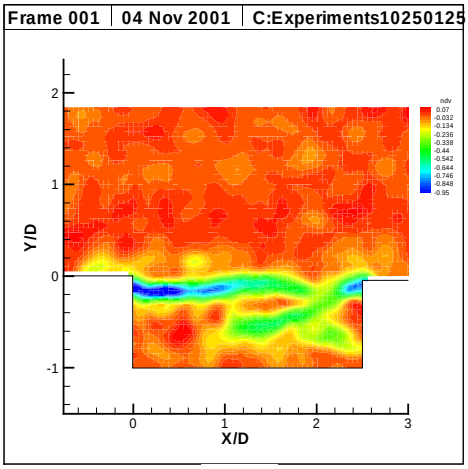

(e)

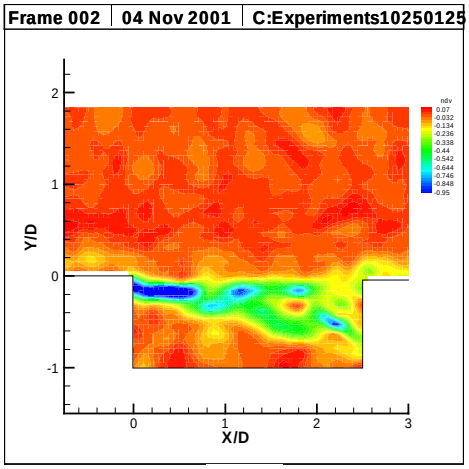

(f)

Figure 5.26 Instantaneous Non-Dimensional Vorticity Contours, Cavity L/D = 2.5, M = 0.57

Figure 5.26(a-f) shows the instantaneous non-dimensional vorticity contours for cavity L/D = 2.5 with the freestream Mach number of 0.57. As the vortices continue to convect in the streamwise direction, their amplitude continues to increase linearly until there is a departure from linear growth. Figure 5.27 plots the distance from the leading edge of the cavity where the shear layer departs from linear growth as a function of the freestream Mach number for cavity L/D ratios 2.5 and 4.5. A visual inspection shows that the deviation from linear growth occurs at a distance of about 0.4 D from the leading edge of the cavity at M = 0.57 for cavity L/D = 2.5. This value of 0.4 D represents an approximately 63 % decrease from the value of 1.1 D observed for M = 0.5. The onset of non-linearity at distance of 0.4 D for M = 0.57 implies that about 85 % of the cavity length is spanned by a non-linearly growing shear layer. This implies that a relatively large amount of the freestream energy is entrained in the shear layer that is available to the cavity for oscillations. In addition, for a free shear layer, at a streamwise coordinate well into the non-linear region, it is known that the amplitude of some of the higher modes could amplify to a point such that they dominate the fundamental mode, thereby transferring the energy from the first mode to higher modes of oscillation[13]. In addition to the fact that the shear layer grows nonlinearly is the fact that a downstream disturbance is created by the interaction of the vortical structures with the cavity trailing edge. This disturbance acts as a major upstream influence that modulates the shear layer at the point of separation. The mode selection at the point of separation is therefore coupled with the upstream influence created by the trailing edge of the cavity. Therefore, amplification of the third mode of oscillation over the first mode is a result of the combination of energy transfer among oscillation modes in the nonlinear shear layer growth region, coupling of the upstream travelling influence with the shear layer, and the well organized nature of vorticity in the shear layer spanning the cavity. Figures 5.28(a-f) plot the instantaneous velocity vectors for this cavity configuration. Just as in the M = 0.4 case, the velocity vectors show the existence of a downward oriented wall jet like flow adjacent to the lower half of the trailing edge of the cavity.

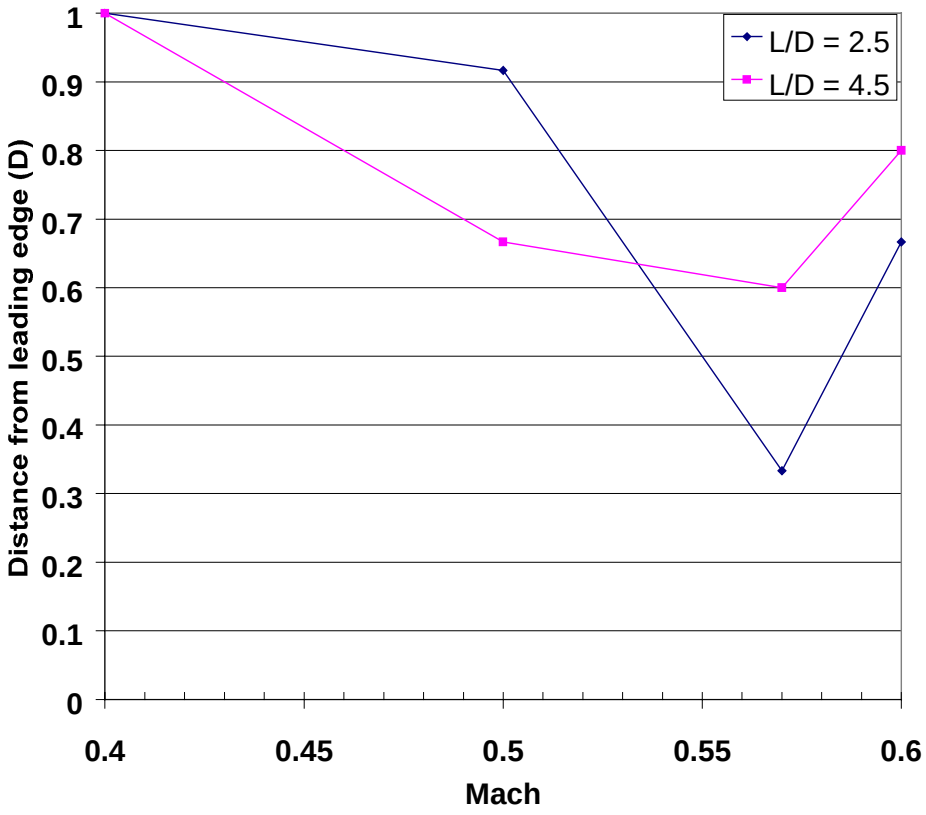

Figure 5.27 Distance from Leading Edge at which Non Linear Shear Layer Growth Begins

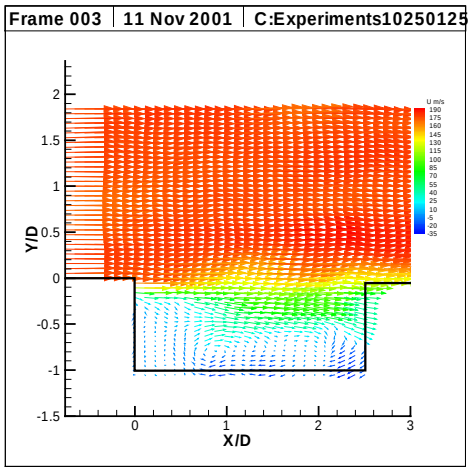

(a)

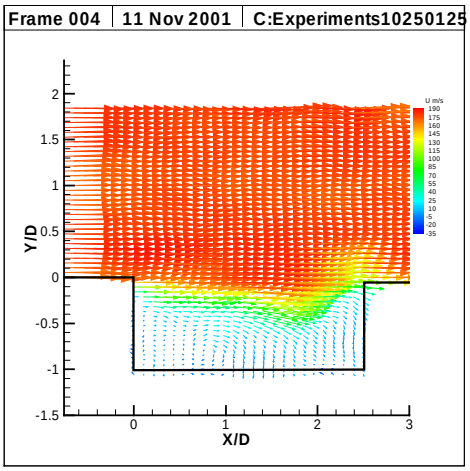

(b)

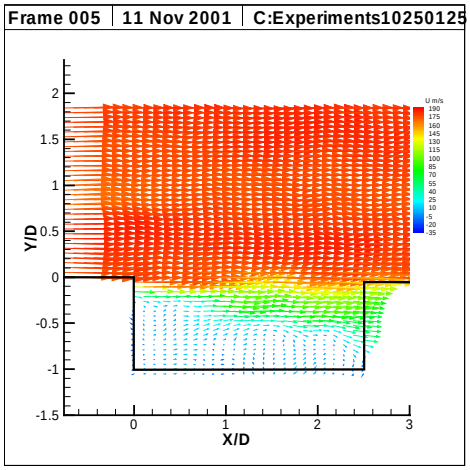

(c)

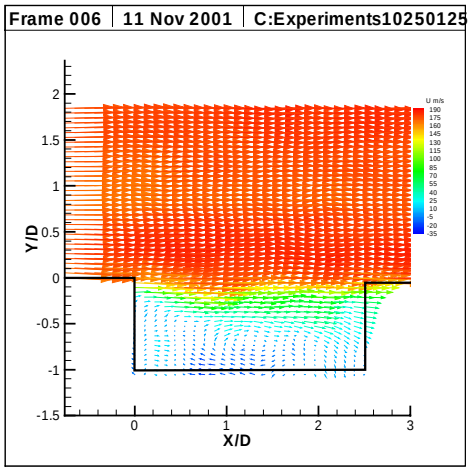

(d)

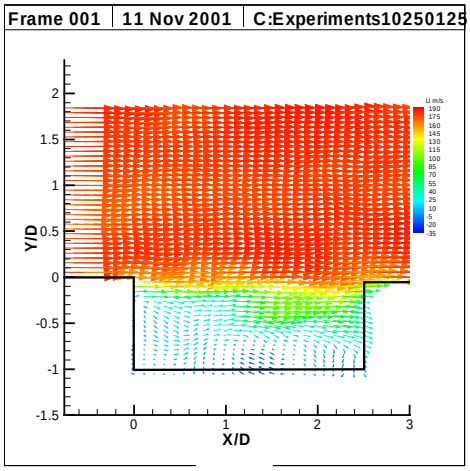

(e)

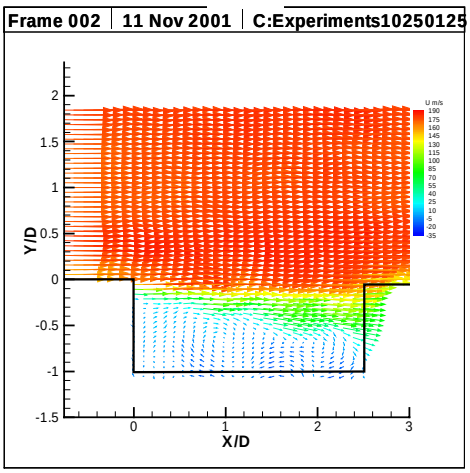

(f)

Figure 5.28 Instantaneous Velocity Vectors, Cavity L/D = 2.5, M = 0.57

A similar wall jet like flow is encountered near the floor of the cavity that extends well upstream of the trailing edge. This jet adjacent to the floor then turns in the upward direction over a short distance to satisfy the large entrainment demands of the shear layer. This jet plays an important role in modulating the shear layer at the leading edge of the cavity. The velocity vectors in Figure 5.28 (b) show an upward oriented outflow of fluid at the trailing edge corner. This outflow is associated with the arrival of the cluster of vorticity as seen in Figure 5.28 (a). On the other hand, Figure 5.28 (f) plots the downward oriented inflow of fluid at the trailing edge corner. Two recirculating zones can be observed within the cavity and they tend to occupy the right half of the cavity. These recirculating zones are not stationary, and they interact with the vortical structures in the shear layer to cause variations in the inflow and outflow of fluid mass.

Figures 5.29 (a-f) show the velocity contours corresponding to the velocity vectors plotted in Figures 5.28 (a-f). The velocity contours clearly demonstrate the motion of the shear layer with mass entrainment and ejection at the trailing edge of the cavity. Figures 5.30 (a) shows the averaged velocity vectors for the given flow conditions. Many of the features that were observed in the instantaneous velocity vector plots can also be observed in the averaged plot. The mean velocity profile clearly shows the growth and spreading of the shear layer along the length of the cavity. A jet like flow near the cavity trailing edge wall, the cavity floor and near the leading edge region can be noticed in the mean velocity. The existence of two recirculating zones that occupy the right half of the inside of the cavity can also be observed from the plot. The mean non-dimensional vorticity contours shown in Figure 5.30 (b) confirm the nonlinear growth of the shear layer with the early onset of the non-linear shear layer growth clearly demarcated in the contour plot.

Figure 5.31 (a) plots the turbulence intensity for cavity L/D = 2.5 at m = 0.57. The region immediately above the shear layer shows a turbulence intensity value of about 5%. Figure 5.31 (b) shows a contour plot of the Reynolds stress. It is evident from the Reynolds Stress contours

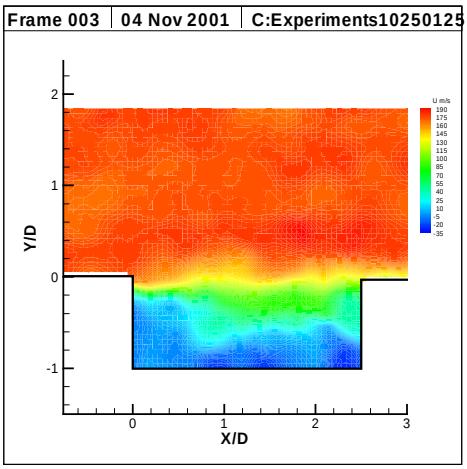

(a)

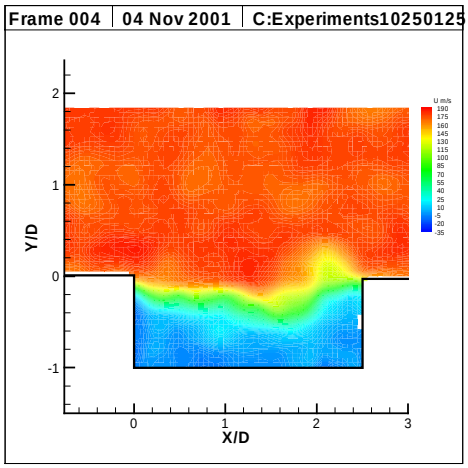

(b)

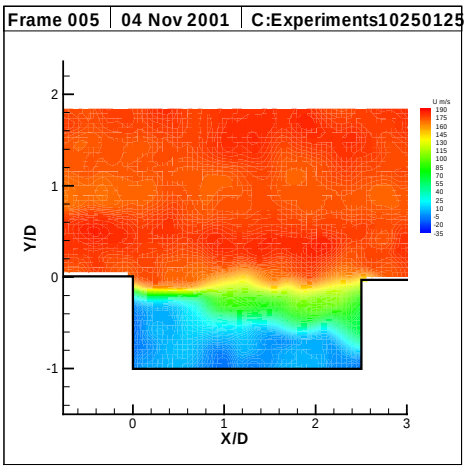

(c)

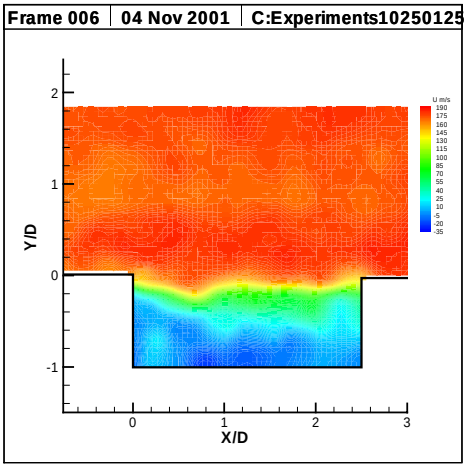

(d)

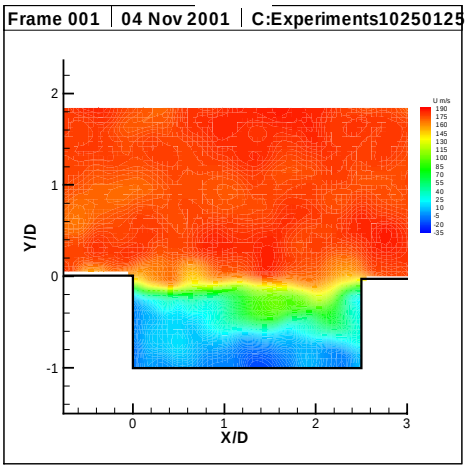

(e)

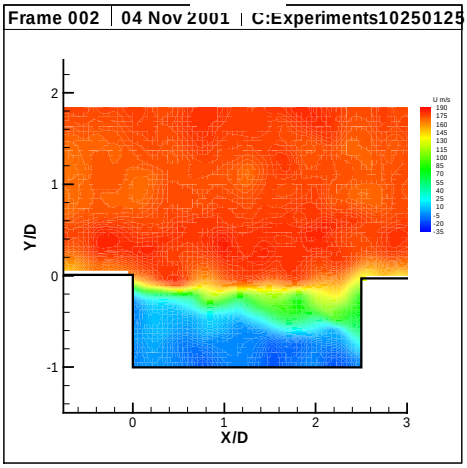

(f)

Figure 5.29 Instantaneous Velocity Contours, Cavity L/D = 2.5, M = 0.57

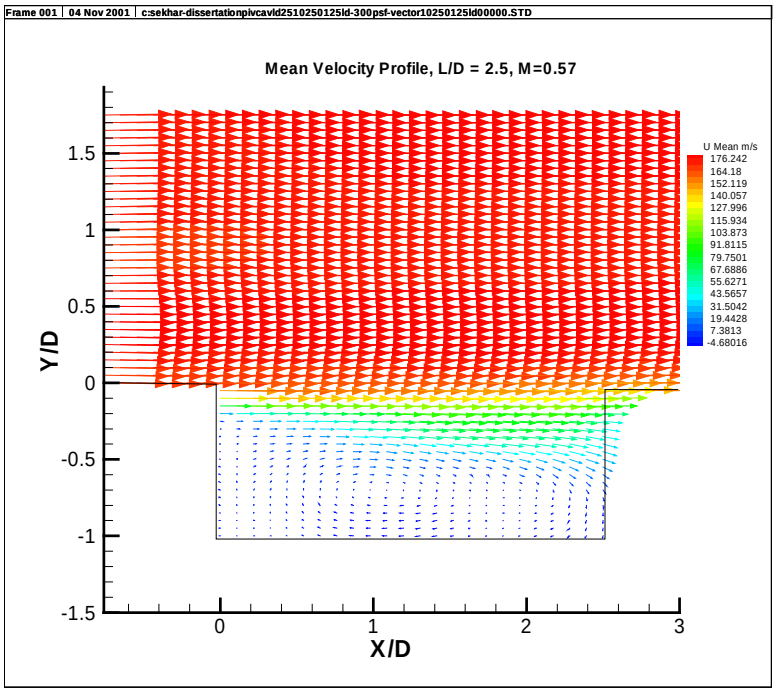

(a)

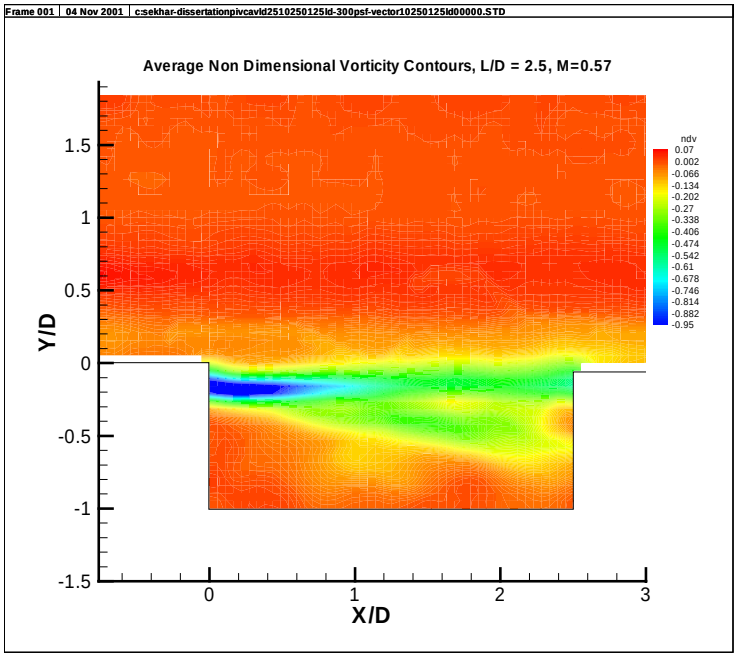

(b)

Figure 5.30 Averaged Velocity and Vorticity Field, Cavity L/D = 2.5, M = 0.57, (a) Velocity Vectors, (b) Vorticity Contours

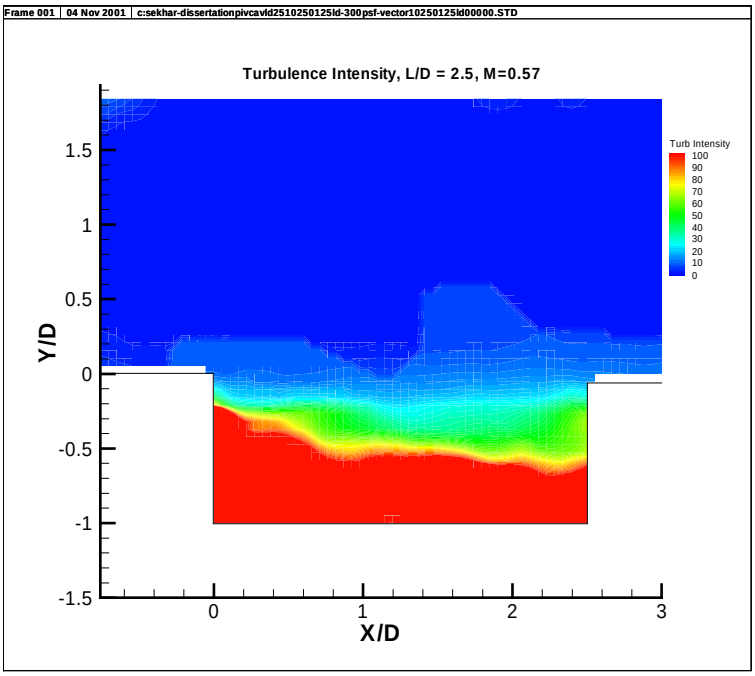

(a)

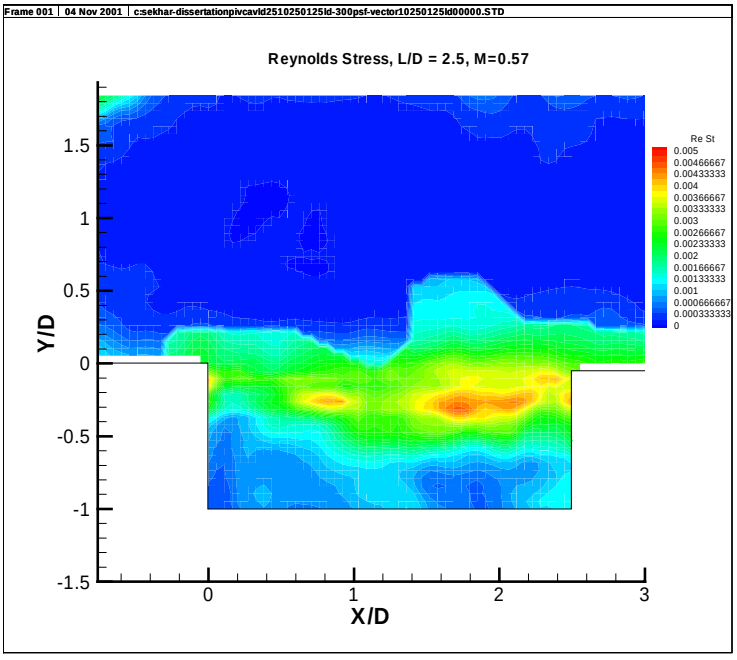

(b)

Figure 5.31 Averaged Velocity Fluctuations and Reynolds Stress, Cavity L/D = 2.5, M = 0.57, (a) Velocity Fluctuations (Turbulence Intensity), (b) Reynolds Stress

that the shear layer becomes non-linear at a distance of about 0.4 D from the leading edge of the cavity.

5.2.2.4 PIV Results, L/D = 2.5, M = 0.6

Figures 5.32 (a-f) show the vorticity contours of the cavity L/D = 2.5 with the freestream Mach number set at 0.6. The vorticity concentrations immediately downstream of the cavity leading edge show very high values and continue to have high values throughout the shear layer that spans the cavity. This suggests a well-organized system of vortical structures in the shear layer. The impingement of the shear layer vortices with the cavity trailing edge is observed from figure 5.32 (d). Cavity L/D = 2.5 at a freestream Mach number of 0.6 represents a coherent interaction of the flow with the cavity that produced a well defined peak at 1617 Hz in the spectrum of the pressure signal.

From figure 5.27 it can be seen that the non-linear growth of the shear layer starts at a distance of 0.8 D from the leading edge as compared to a distance of 0.4 D observed for the M = 0.57 case. This implies that about 68% of the cavity length is spanned by a non-linearly growing shear layer in the M = 0.6 configuration. This value is less than the 85% length that is spanned by the non linear shear layer in the M = 0.57 case. The reduction of the cavity length spanned by a non-linear shear layer may be the reason for the dominance of the fundamental mode of oscillation over the subsequent modes for cavity L/D = 2.5 at M = 0.6. That this is indeed the case is evident from the SPL peak at a frequency of 1617 Hz (fundamental mode) displayed in the power spectrum plotted in Figure 5.15 (h). Figures 5.33 (a-f) plot the velocity vectors for cavity L/D = 2.5 with freestream M = 0.6. The vectors show the characteristic spreading of the shear layer along the length of the cavity. The inflow and outflow of fluid mass associated with the motion of the shear layer can be seen in figure 5.33 (a) and (b) respectively. The vector plots also show the existence of two well- defined recirculating zones inside the cavity. Also evident are jet-

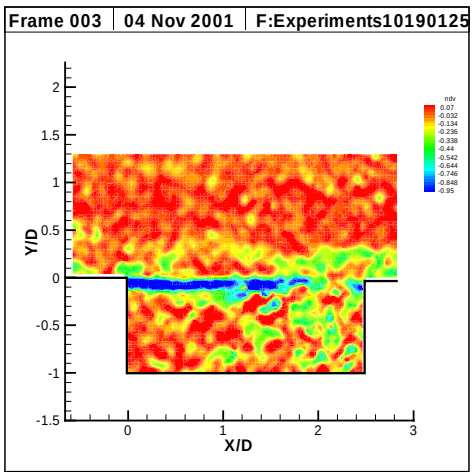

(a)

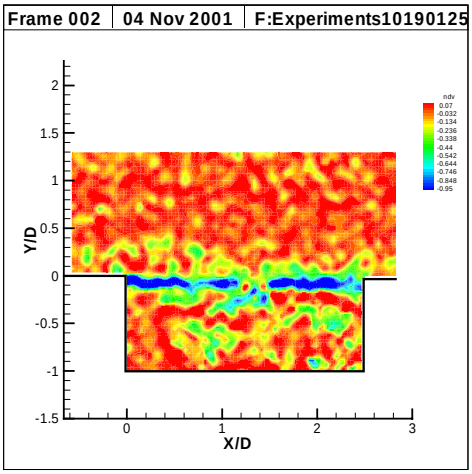

(b)

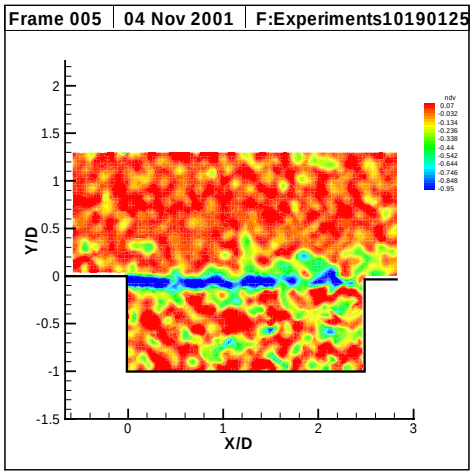

(c)

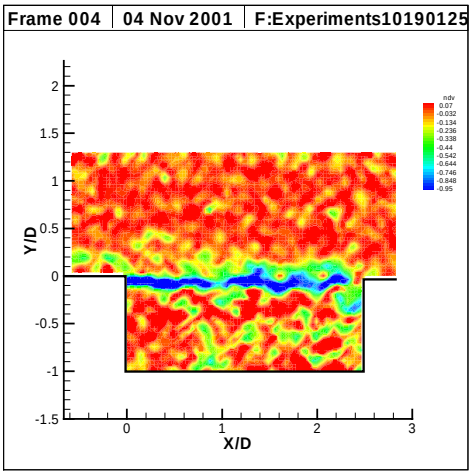

(d)

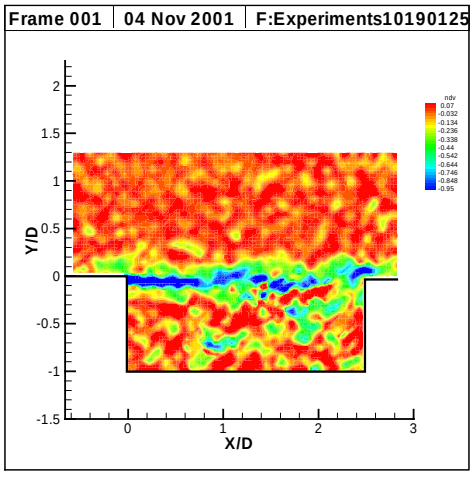

(e)

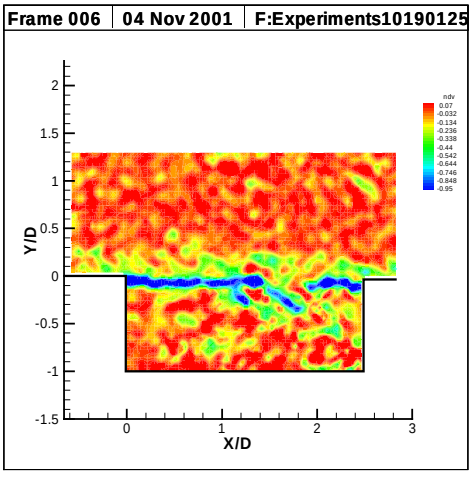

(f)

Figure 5.32 Instantaneous Non-Dimensional Vorticity Contours, cavity L/D = 2.5, M = 0.6

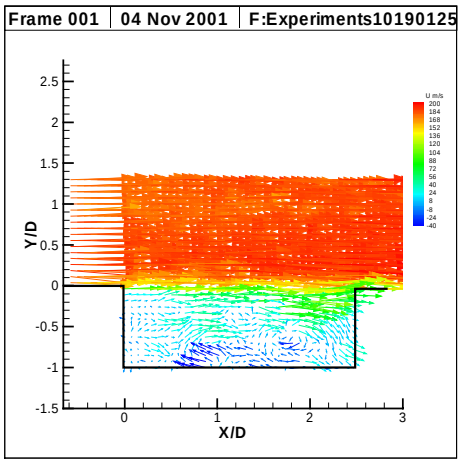

(a)

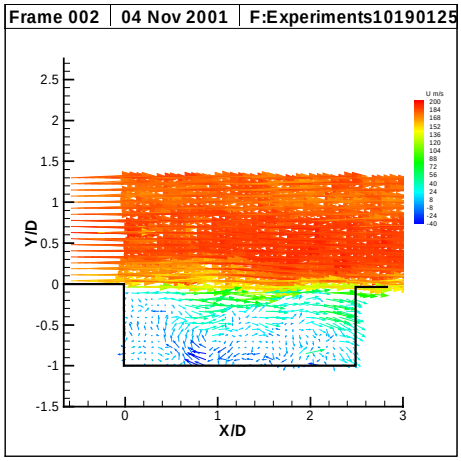

(b)

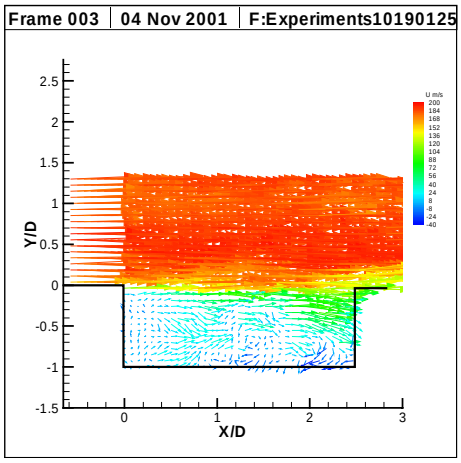

(c)

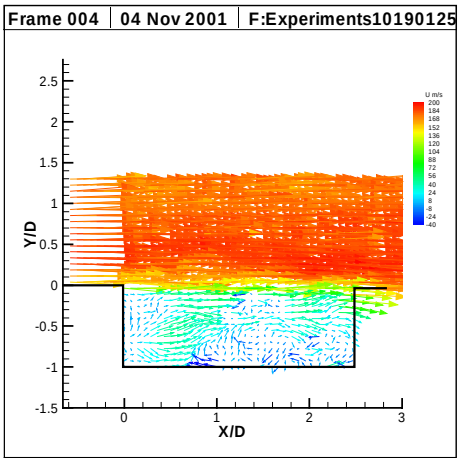

(d)

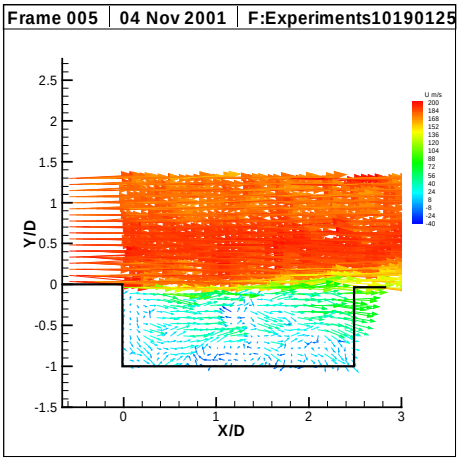

(e)

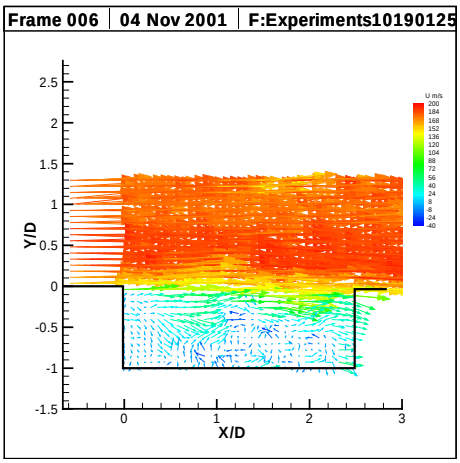

(f)

Figure 5.33 Instantaneous Velocity Vectors, Cavity L/D = 2.5, M = 0.6

like flows along the vertical trailing edge and the cavity floor, and the entrainment of fluid mass from the inside of the cavity into the shear layer adjacent to the leading edge. The velocity contours plotted in figures 5.34 (a-f) show the motion of the shear layer in the vertical direction.

The averaged velocity and vorticity plots shown in figures 5.35 (a) and 5.35 (b) respectively capture most of the features of the flow as discussed for the instantaneous plots.

Figure 5.36 (a) shows the turbulence intensity obtained from averaging the velocity vectors. The freestream turbulence intensity was measured as 5%. The plot for the Reynolds Stress is shown in figure 5.36 (b).

5.2.2.5 PIV Results, L/D = 4.5, M = 0.4

Figures 5.37 (a-f) plot the non-dimensional vorticity contours for cavity L/D = 4.5 and freestream Mach number set at 0.4. The plots show that the vorticity is weakly scattered inside the cavity, and vortical structures are relatively ill organized in the shear layer, indicating a weak interaction of the flow with the cavity geometry. The non-coherent interaction between the flow and the cavity explains the absence of a well-defined SPL peak in the corresponding spectra displayed in figures 5.16 (e) and 5.16 (f). The corresponding instantaneous velocity vectors are plotted in figures 5.38 (a-f). The velocity vectors display the spreading of the shear layer as we travel downstream along the length of the cavity. A number of ill-defined weakly recirculating vortices are observed within the cavity. The ejection (figure 5.38 (a)) and entrainment (figure 5.38 (d)) of fluid mass from and into the cavity is also observed. Overall, the vortical structures in the shear layer and the weak recirculating zones show a lack of organization that explains the weakly coherent interaction of the flow with the cavity geometry.

From figure 5.27, it is observed that the non-linear growth of the shear layer for cavity L/D 4.5 occurs at a distance larger than that observed for cavity L/D = 2.5. However, the rate of

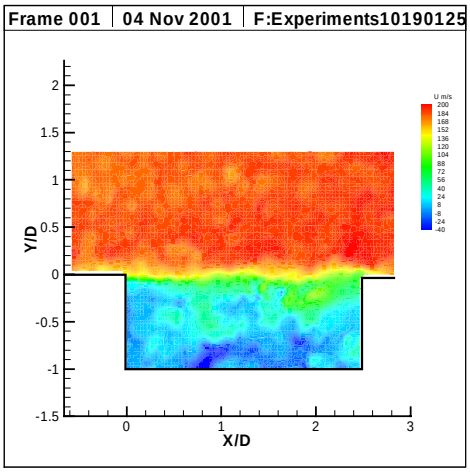

(a)

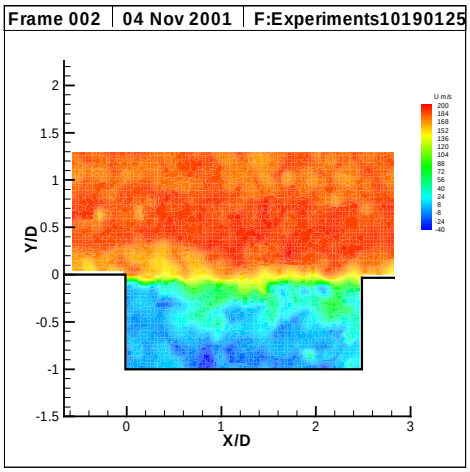

(b)

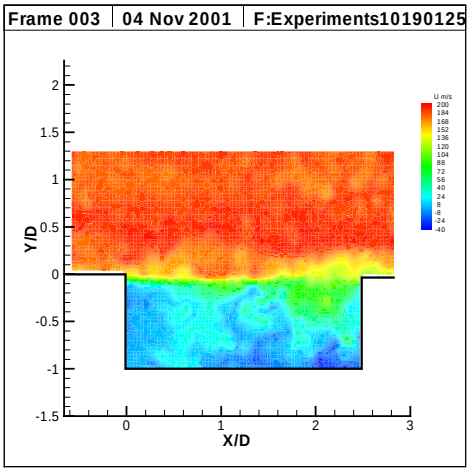

(c)

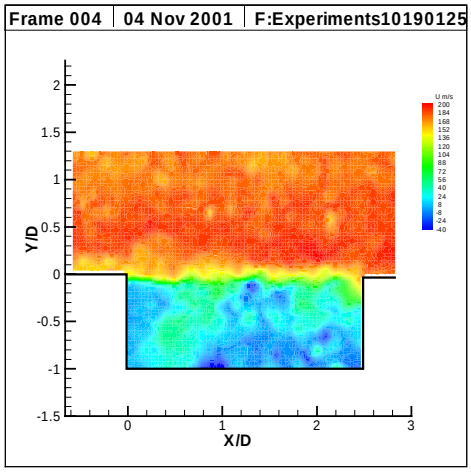

(d)

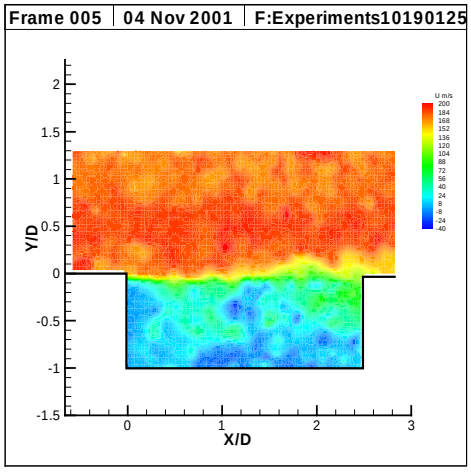

(e)

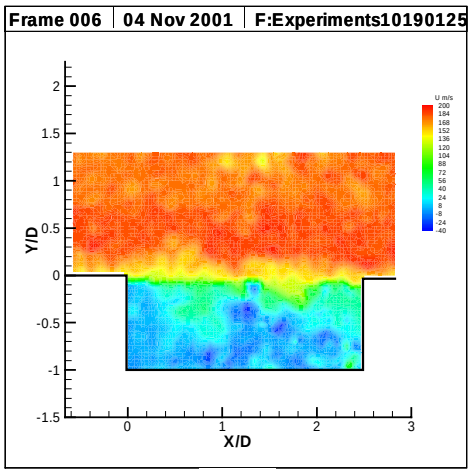

(f)

Figure 5.34 Instantaneous Velocity Contours, Cavity L/D = 2.5, M = 0.6

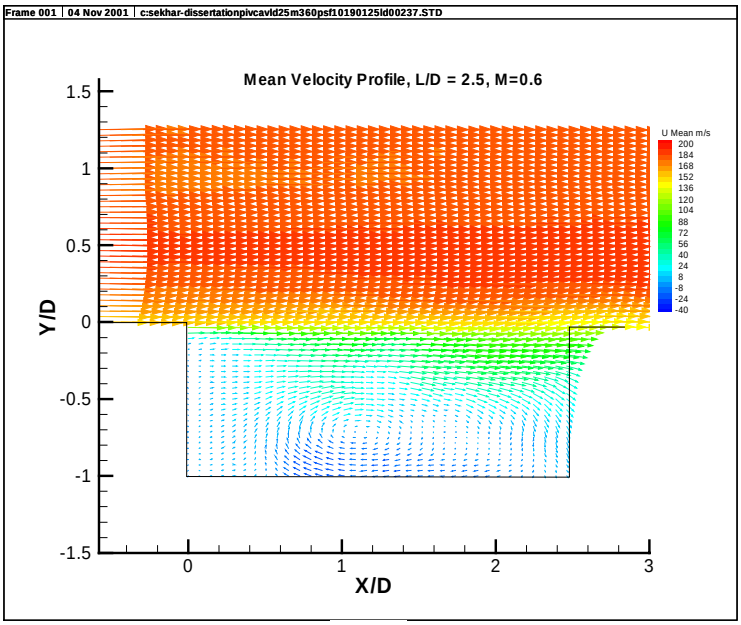

(a)

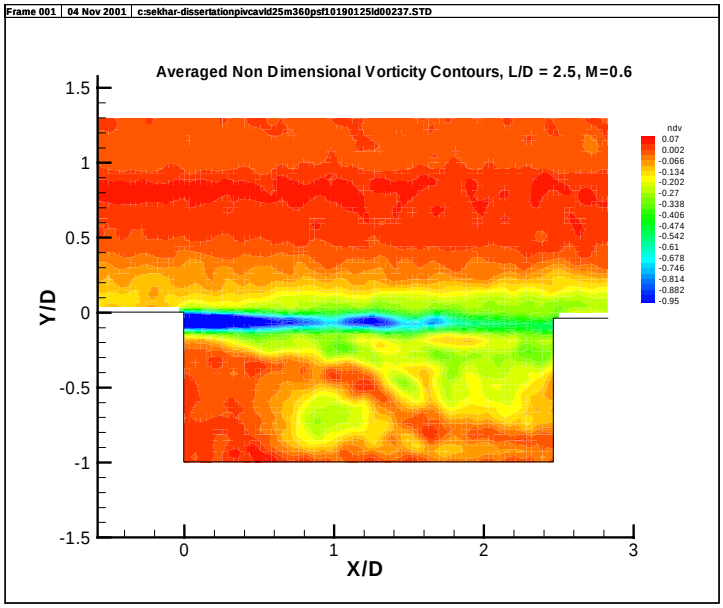

(b)

Figure 5.35 Averaged Velocity and Vorticity Field, Cavity L/D = 2.5, M = 0.6, (a) Velocity Vectors, (b) Vorticity Contours

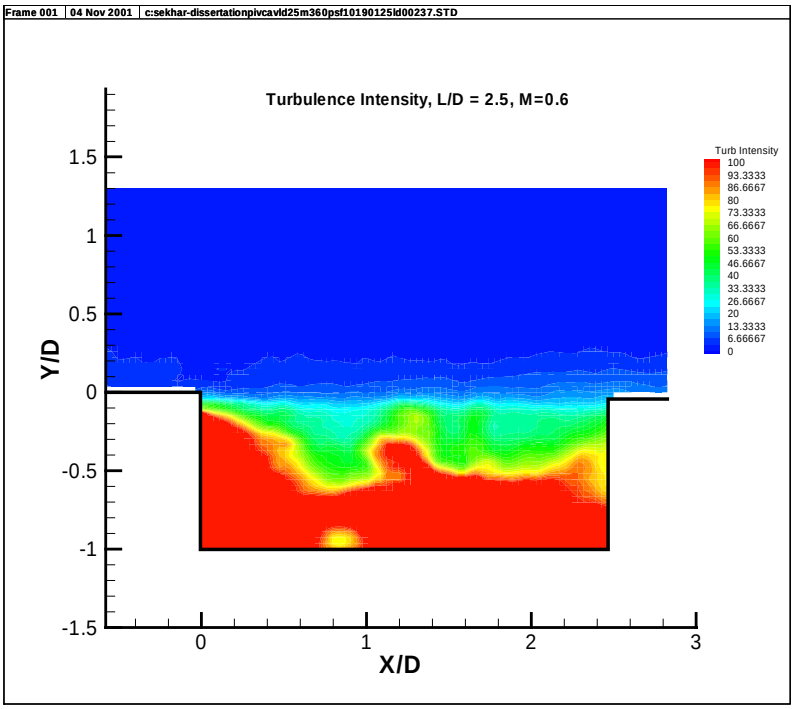

(a)

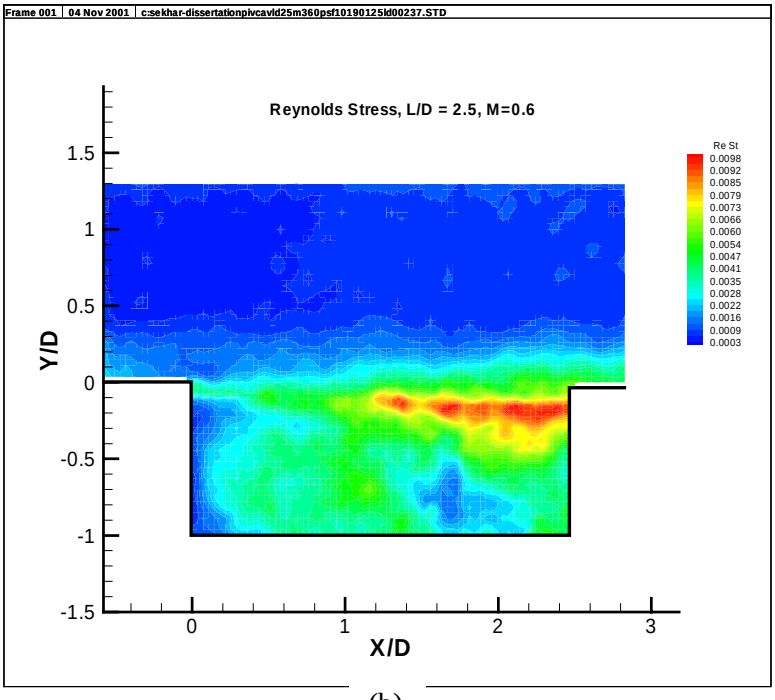

(b)

Figure 5.36 Averaged Velocity Fluctuations and Reynolds Stress, Cavity L/D = 2.5, M = 0.6, (a) Velocity Fluctuations (Turbulence Intensity), (b) Reynolds Stress

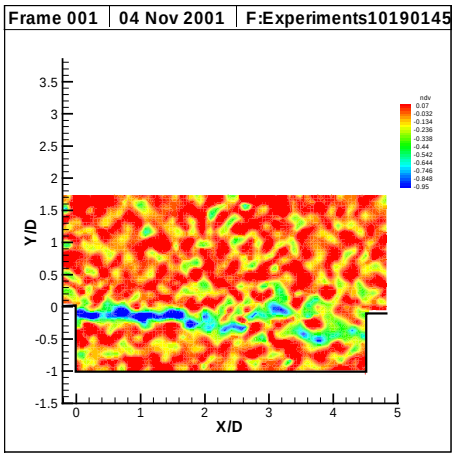

(a)

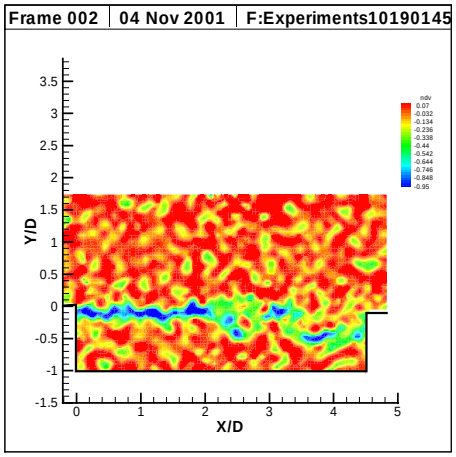

(b)

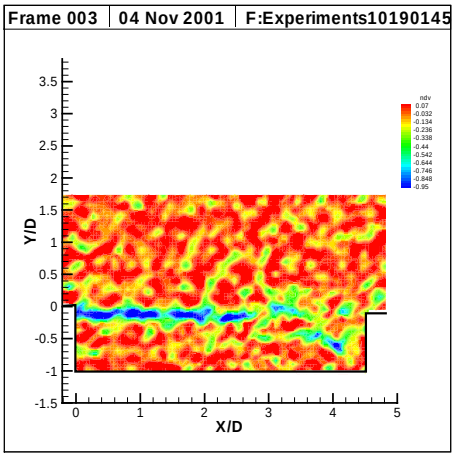

(c)

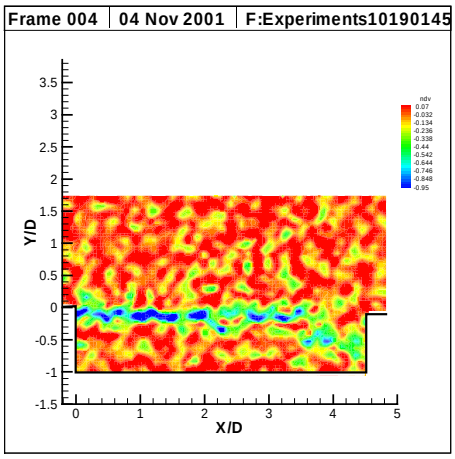

(d)

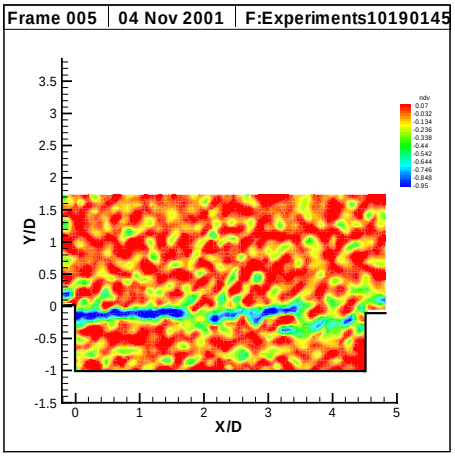

(e)

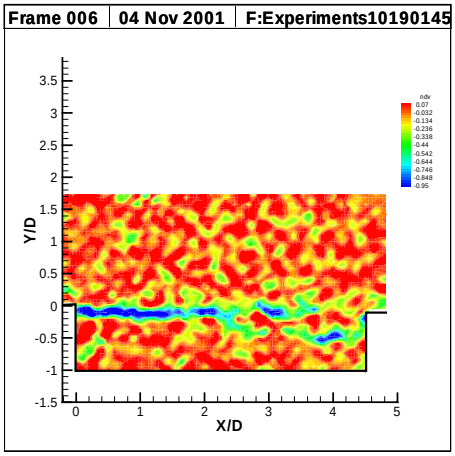

(f)

Figure 5.37. Instantaneous Non-Dimensional Vorticity Contours, Cavity L/D = 4.5, M = 0.4

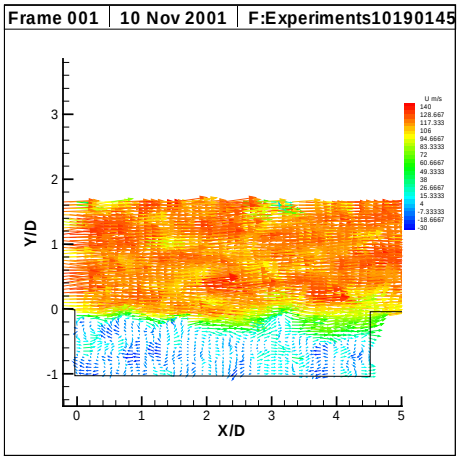

(a)

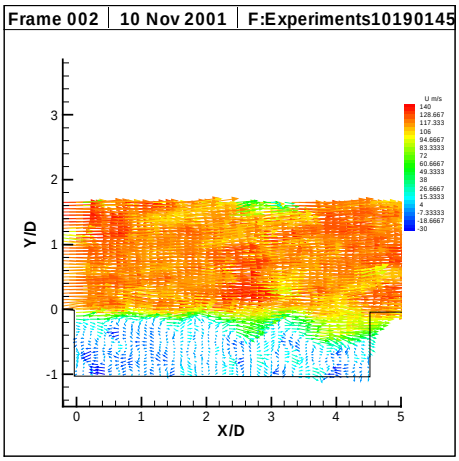

(b)

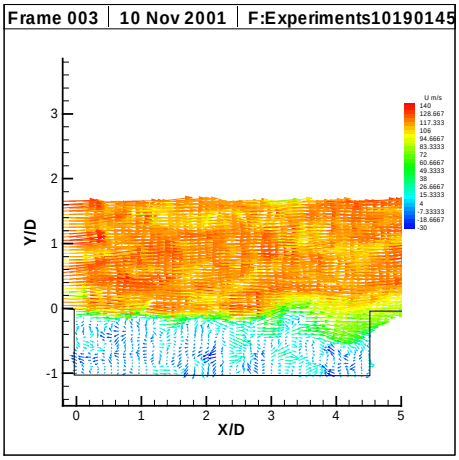

(c)

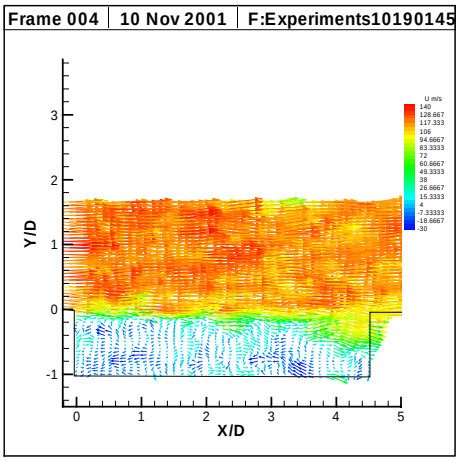

(d)

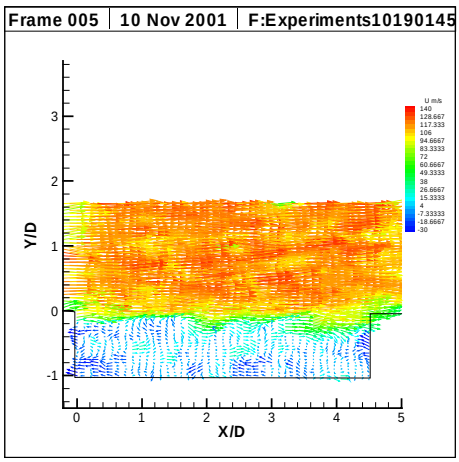

(e)

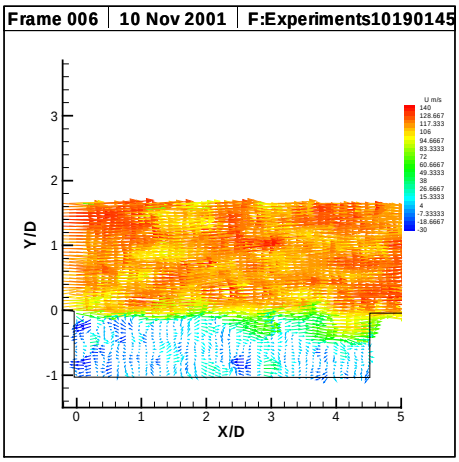

(f)

Figure 5.38. Instantaneous Velocity Vectors, Cavity L/D = 4.5, M = 0.4

growth of the shear layer is not as high as is observed for cavity L/D = 2.5. This could explain the absence of mode switching over this Mach number range for cavity L/D 4.5. For L/D = 4.5, the percentage variation in distance at which the shear layer starts growing non-linearly for various Mach numbers is relatively small as compared to L/D = 2.5. This further explains the absence of mode switching for cavity L/D = 4.5 over this mach number range.

Instantaneous velocity contours are shown in figure 5.39 (a-f). The motion of the shear layer in the vertical direction is apparent from the plots. However, the shear layer is seen to be relatively ill-defined.

Figures 5.40(a) shows the averaged velocity vectors for the given flow conditions. Many of the features that were observed in the instantaneous velocity vector plots can also be observed in the averaged plot. The mean non-dimensional vorticity contours are shown in Figure 5.40 (b). The averaged recirculation zone inside the cavity is represented by a green contour with a non-dimensional vorticity value of about -.202.

Figure 5.41 (a) and 5.41 (b) plot the turbulence intensity and the Reynolds stress respectively.

5.2.2.6 PIV Results, L/D = 4.5, M = 0.6

Figures 5.42 (a-f) plot the non-dimensional vorticity contours for cavity L/D = 4.5 and freestream Mach number set at 0.6. In sharp contrast to the cavity configuration corresponding to cavity L/D = 4.5, M = 0.4, the vorticity plots for this configuration show that the vorticity is concentrated in the shear layer region, and the vortical structures are highly organized in the shear layer. This indicates a coherent interaction of the flow with the cavity geometry. The coherent is the reason for the presence of a well-defined SPL peak at a frequency of 1863 Hz in the corresponding spectra displayed in figures 5.16 (i) and 5.16 (j).

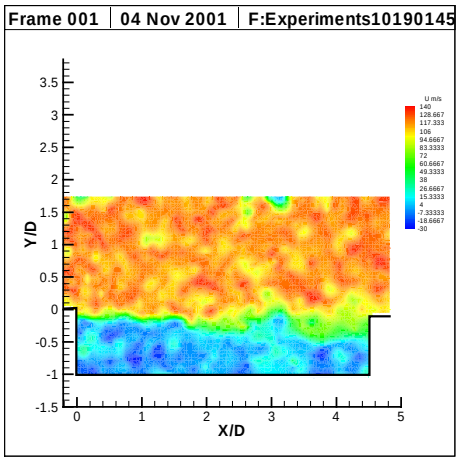

(a)

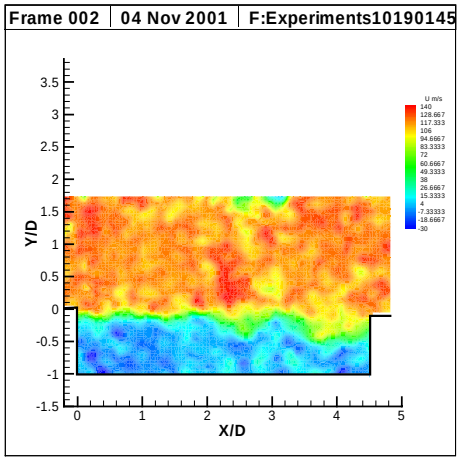

(b)

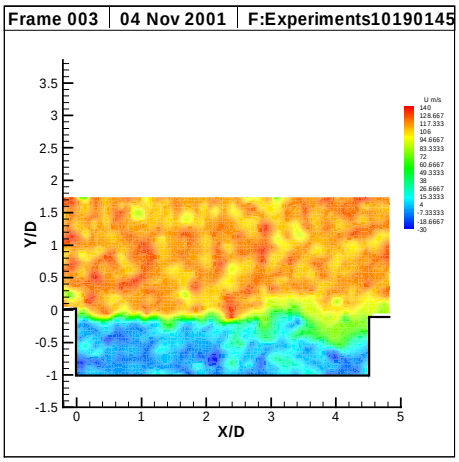

(c)

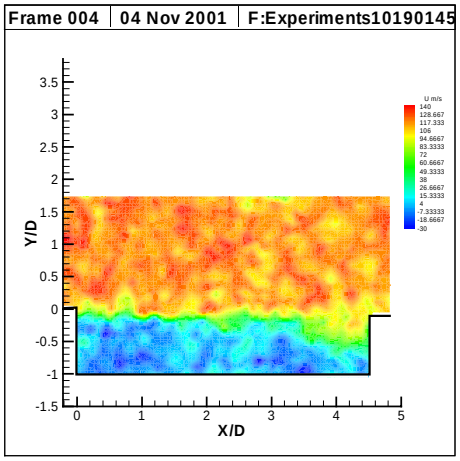

(d)

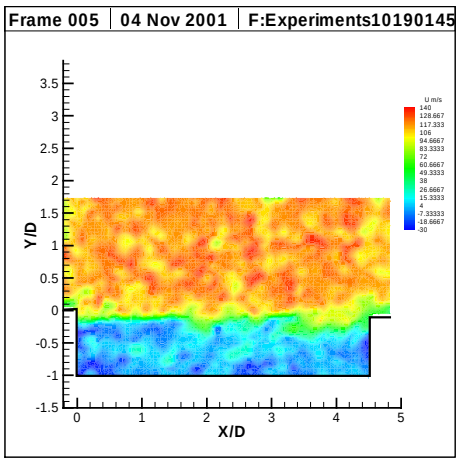

(e)

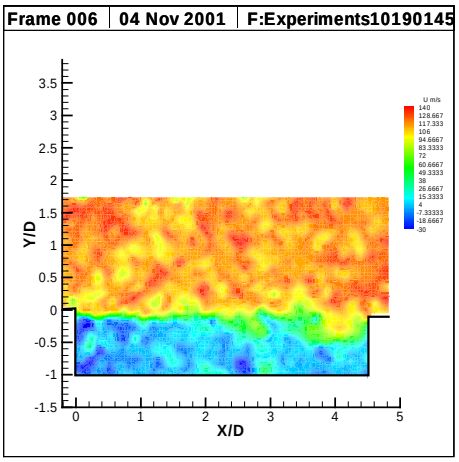

(f)

Figure 5.39. Instantaneous Velocity Contours, Cavity L/D = 4.5, M = 0.4

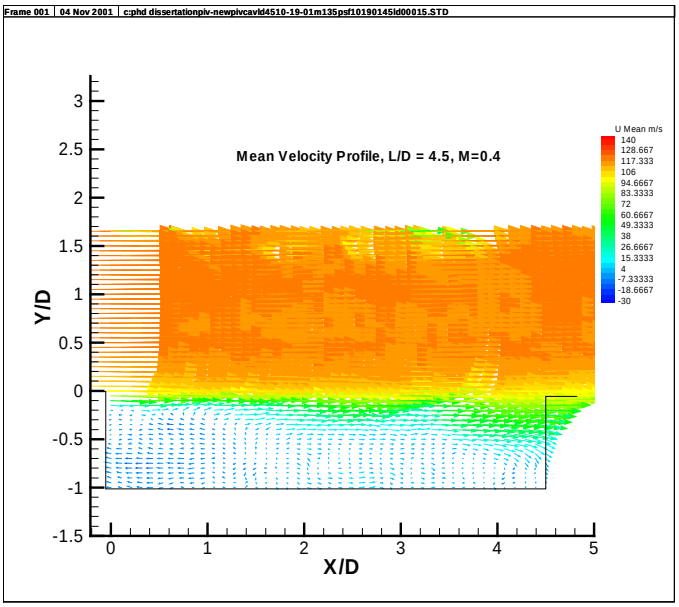

(a)

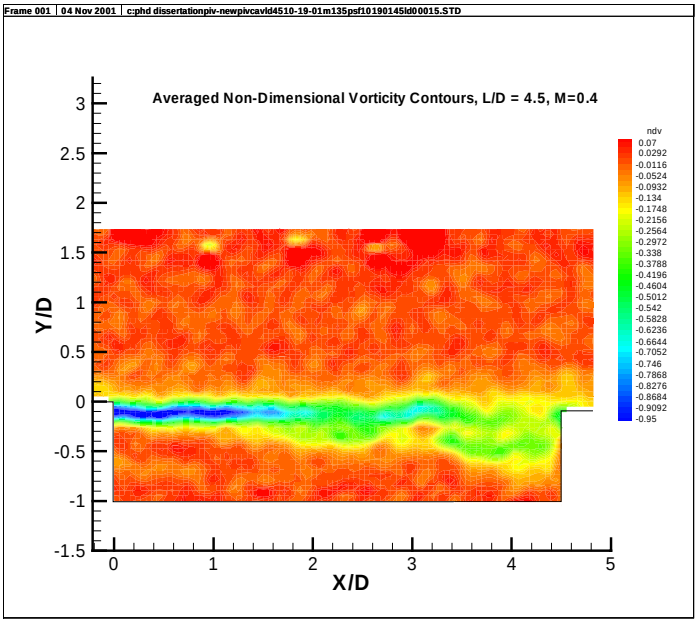

(b)

Figure 5.40 Averaged Velocity and Vorticity Field, Cavity L/D = 4.5, M = 0.4, (a) Velocity Vectors, (b) Vorticity Contours

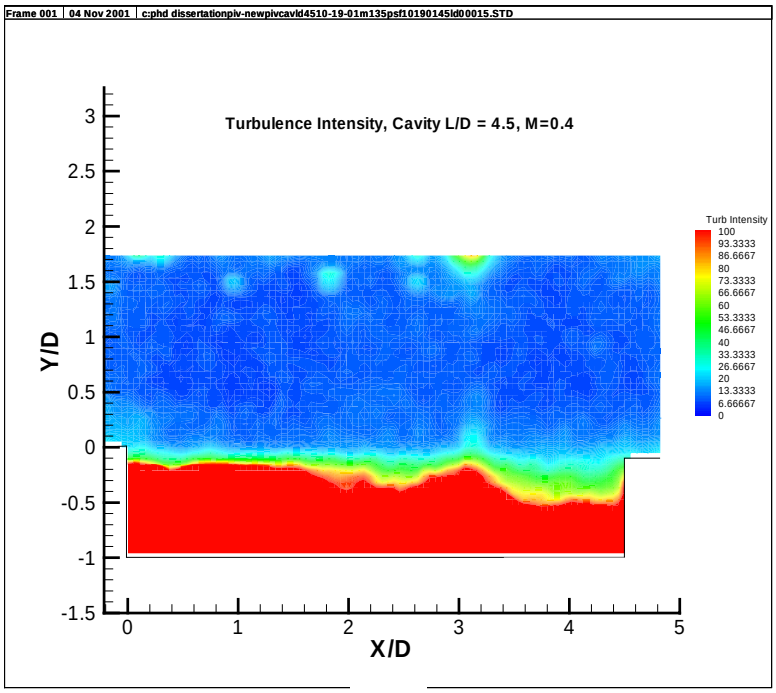

(a)

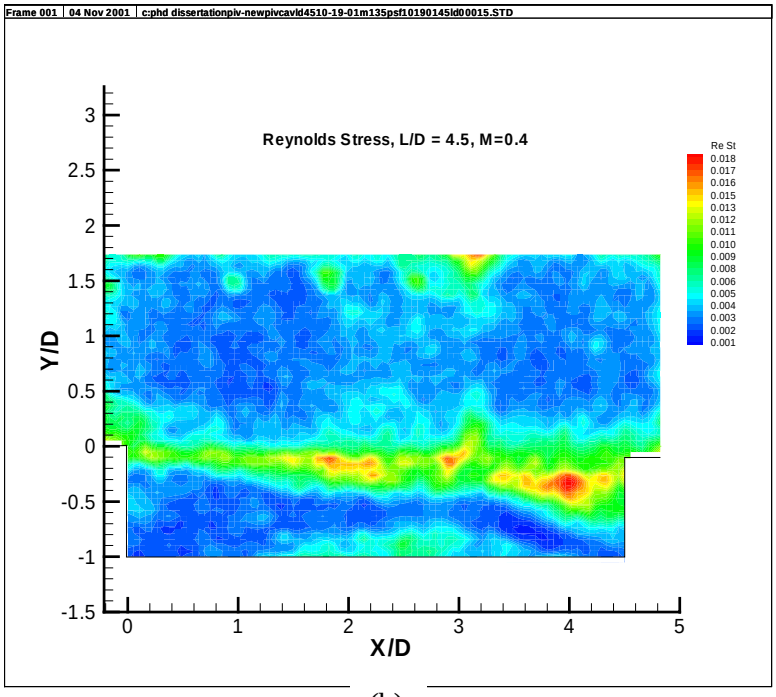

(b)

Figure 5.41 Averaged Velocity Fluctuations and Reynolds Stress, Cavity L/D = 4.5, M = 0.4, (a) Velocity Fluctuations (Turbulence Intensity), (b) Reynolds Stress

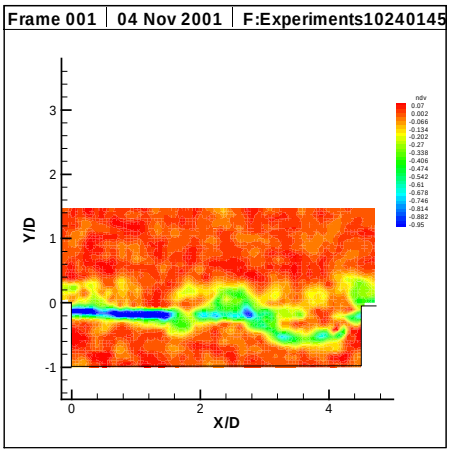

(a)

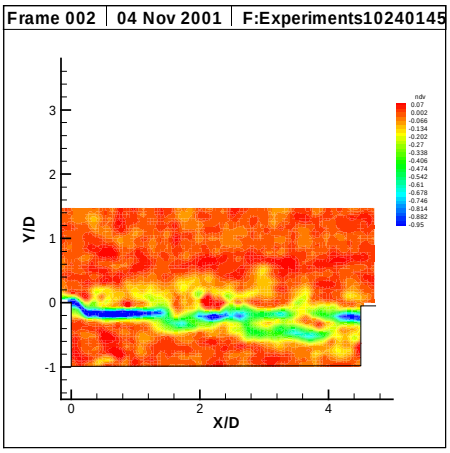

(b)

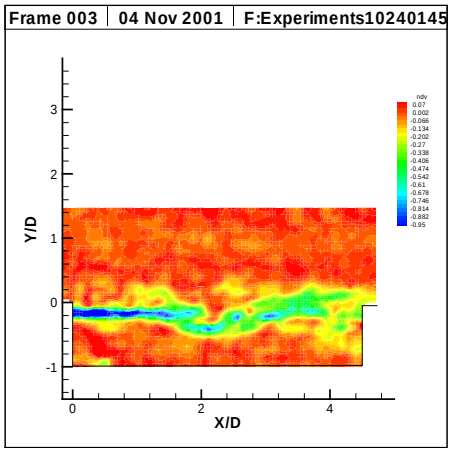

(c)

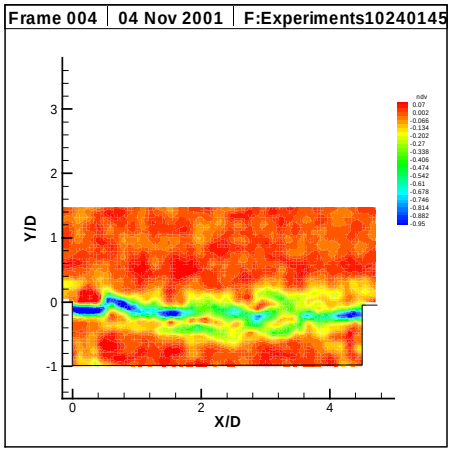

(d)

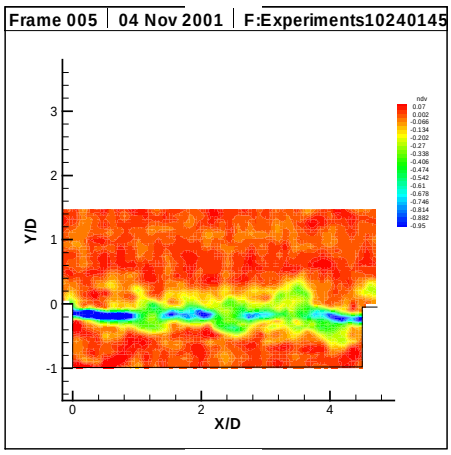

(e)

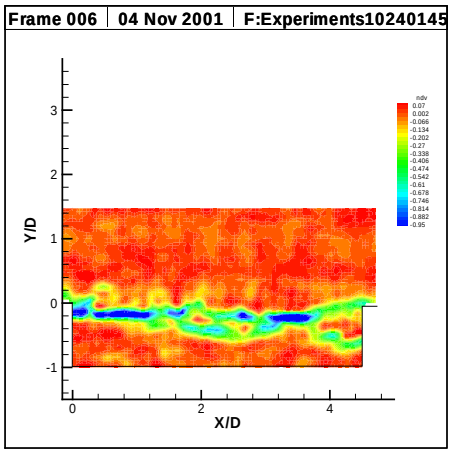

(f)

Figure 5.42. Instantaneous Non-Dimensional Vorticity Contours, Cavity L/D = 4.5, M = 0.6

Figures 5.43 (a-f) show the corresponding instantaneous velocity vectors plotted for cavity L/D = 4.5 with the freestream Mach number set at 0.6. Clearly seen from the vector plots is the formation of a vortex at the leading edge (figure 5.43 (a)) that travels downstream along the shear layer and coalesces with the vortex produced in the shear layer at a distance of approximately half the length of the cavity (figure 5.43 (c)). The merged vortex then travels downstream, impinges on the cavity trailing edge, and gets entrained in the recirculation zone adjacent to the vertical wall of the trailing edge. Other well-defined recirculation zones can also be seen within the cavity. This is in contrast with the velocity vector fields for cavity L/D = 2.5, M = 0.6 (figures 5.33 (a-f)) that show the existence of two recirculating zones within the cavity. On the whole, the flow features for this cavity flow configuration, that represents a strong flow cavity interaction, are in sharp contrast to the flow features seen in the case for cavity L/ D = 4.5, M = 0.4. This comparison serves to highlight the marked differences that exist for a flow field that interactsnon coherently with the cavity, and a flow field that is strongly coherent with the cavity.

The instantaneous velocity contours shown in figures 5.44 (a-f) display the existence of a relatively well defined shear layer that spreads along the streamwise coordinate of the cavity.

The averaged velocity profile displayed in figure 5.45(a) shows the formation of the leading edge vortex, and its convection downstream. However, the multiple number of recirculating zones found within the cavity are averaged out such that only two recirculating zones show within the cavity. Thus, the average velocity profile is able to capture the essential features of the instantaneous velocity field. The averaged non-dimensional vorticity contours shown in figure 5.45(b) exhibits the high concentration of vorticity immediately downstream of the cavity leading edge and the formation of a sharply defined shear layer spanning the cavity.

The turbulence intensity value in the freestream is about 5% as shown in figure 5.46 (a). The Reynolds stress plot in Figure 5.46 (b) shows a high stress region near the leading edge of the cavity indicating the roll up of the leading edge vortex. A high value of Reynolds stress is also

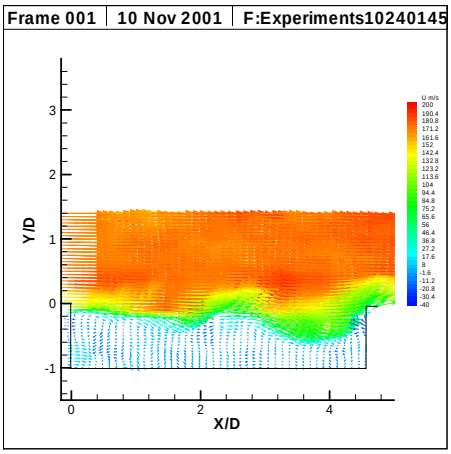

(a)

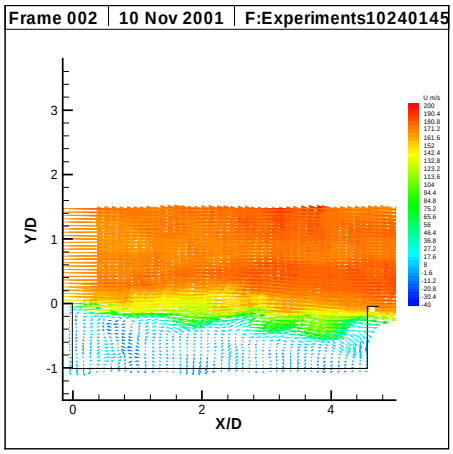

(b)

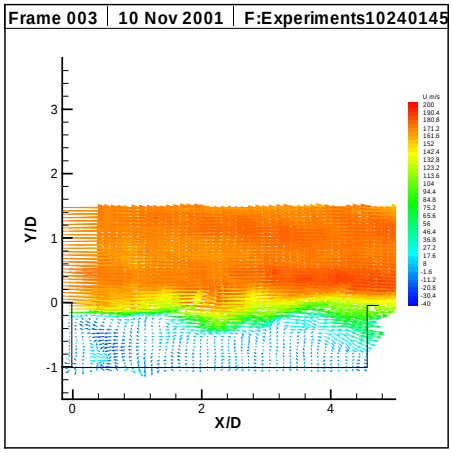

(c)

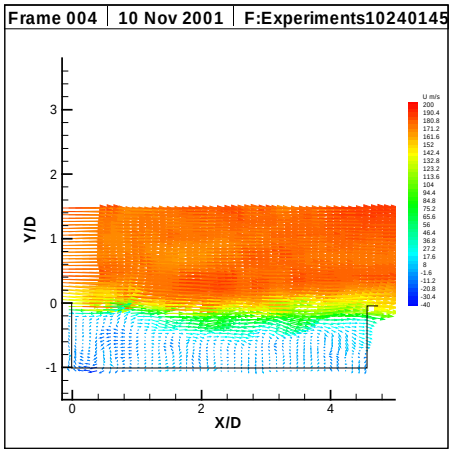

(d)

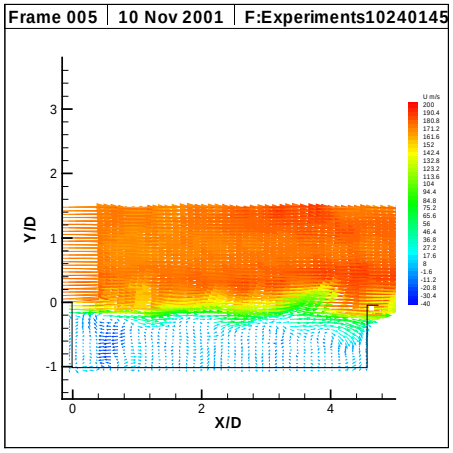

(e)

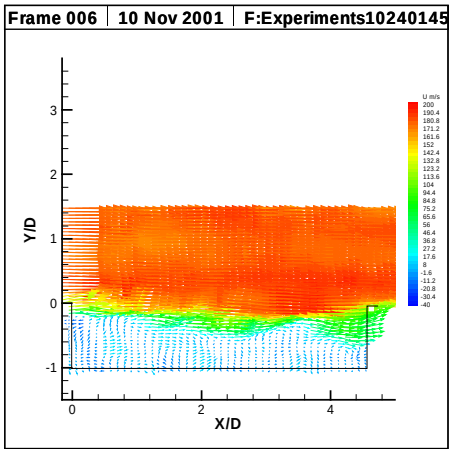

(f)

Figure 5.43. Instantaneous Velocity Vectors, Cavity L/D = 4.5, M = 0.6

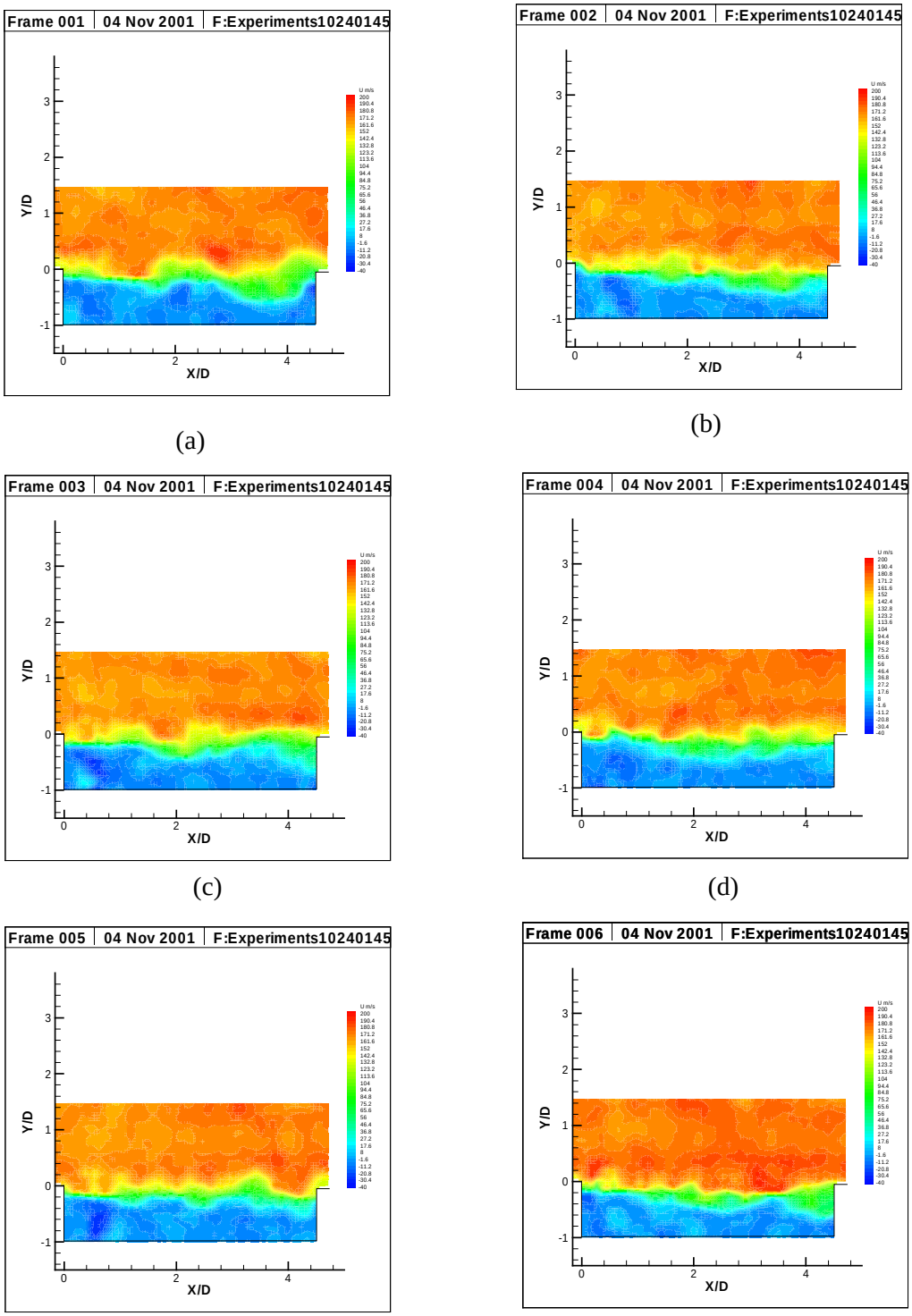

Figure 5.44. Instantaneous Velocity Contours, Cavity L/D = 4.5, M = 0.6

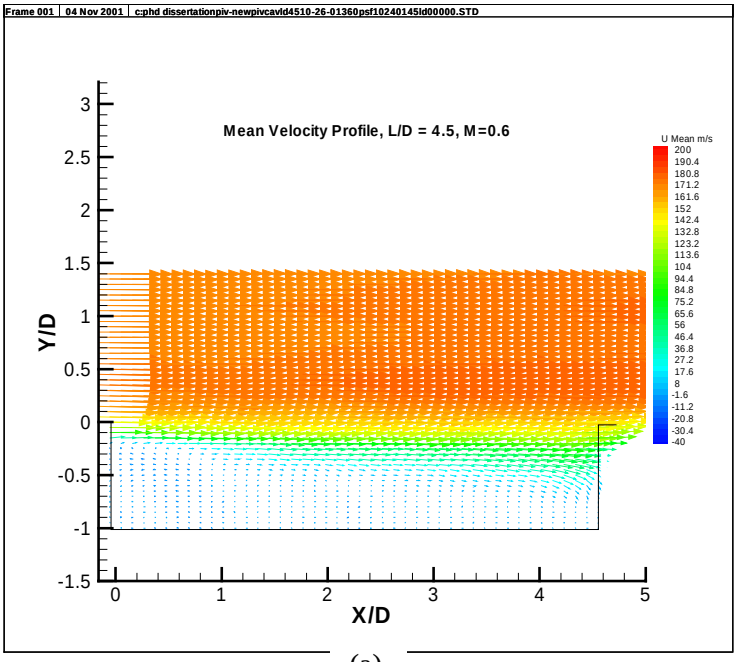

(a)

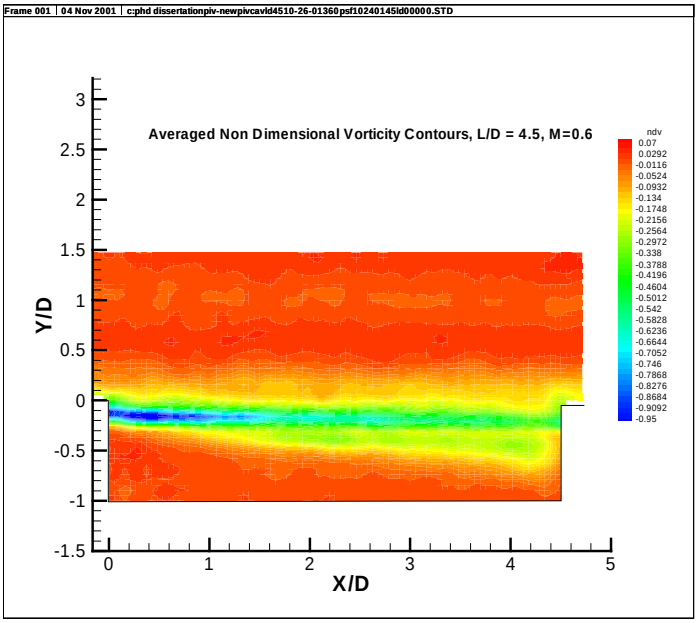

(b)

Figure 5.45 Averaged Velocity and Vorticity Field, Cavity L/D = 4.5, M = 0.6, (a) Velocity Vectors, (b) Vorticity Contours

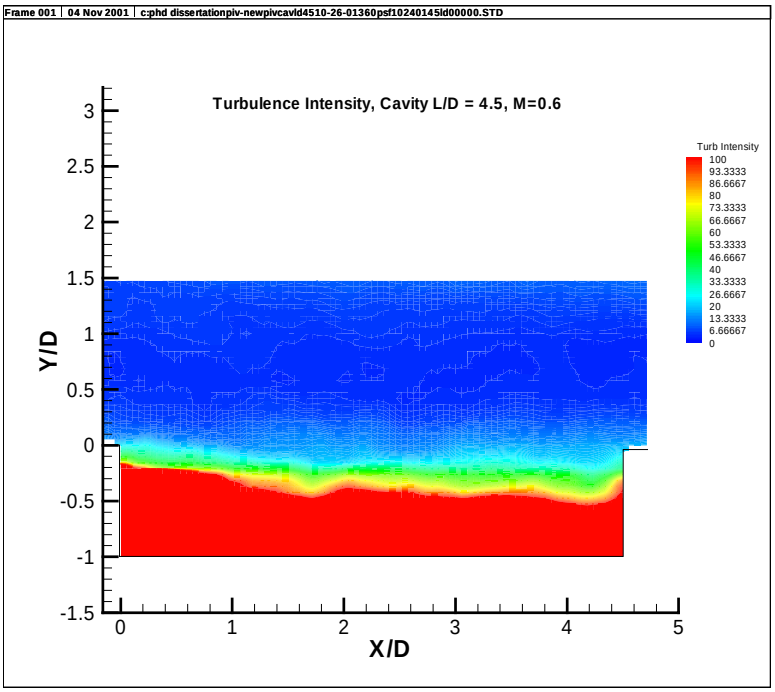

(a)

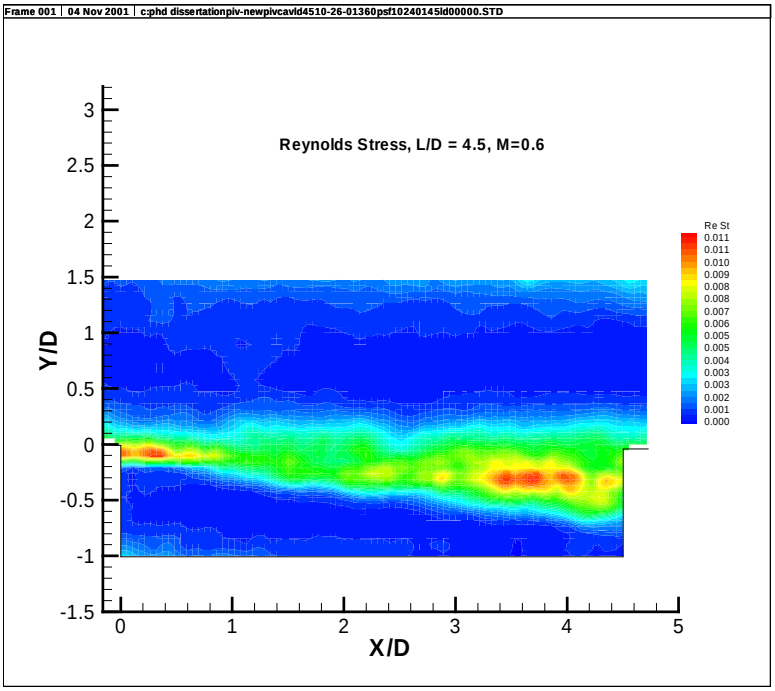

(b)

Figure 5.46 Averaged Velocity Fluctuations and Reynolds Stress, Cavity L/D = 4.5, M = 0.6, (a) Velocity Fluctuations (Turbulence Intensity), (b) Reynolds Stress

seen near the trailing edge of the cavity that corresponds to the entrainment of the vortical structures in the shear layer by the recirculating zone adjacent to the trailing wall.

5.2.3 Grid Convergence

A grid convergence study was performed for both cavity L/D ratios 2.5 and 4.5. Based on the study, a grid that was fine enough was chosen for each one of the L/D ratios such that the numerical results obtained from the numerical simulations were independent of the grid resolution. For both the cavity L/D ratios, pressure oscillations were measured on the floor of the cavity at a distance of L = 2D (0.0381 m) from the leading edge of the cavity at a freestream Mach number of 0.6. The grid resolution was made finer and finer until the variation in pressure amplitudes between two successive grids was less than 1% of the mean value of oscillations.

Figure 5.47 shows the comparison in pressure oscillations on the floor of cavity L/D = 2.5 measured for three grid sizes. Each one of the three grids had 10714 points, 16514 points, and 26044 points respectively. In order of increasing resolution, the grids are called the coarse grid, the intermediate grid, and the fine grid respectively. The percentage variation in pressure amplitudes between the coarse grid and the intermediate grid was 3.7 percent and the variation between the intermediate grid and the fine grid was 0.89 percent. Therefore, the fine grid with 26044 grid points was chosen for the numerical simulations. The fine grid is shown in figure 5.48 for cavity L/D = 2.5. A quadratic power law was used for grid stretching. To resolve boundary layers and to capture the features of the shear layer over the length of the cavity, the grid points were clustered near the walls and the shear layer region over the cavity. Following a similar procedure, a grid with 32924 points was selected and used for the cavity L/D = 4.5 computations. The grid is shown in figure 5.49.

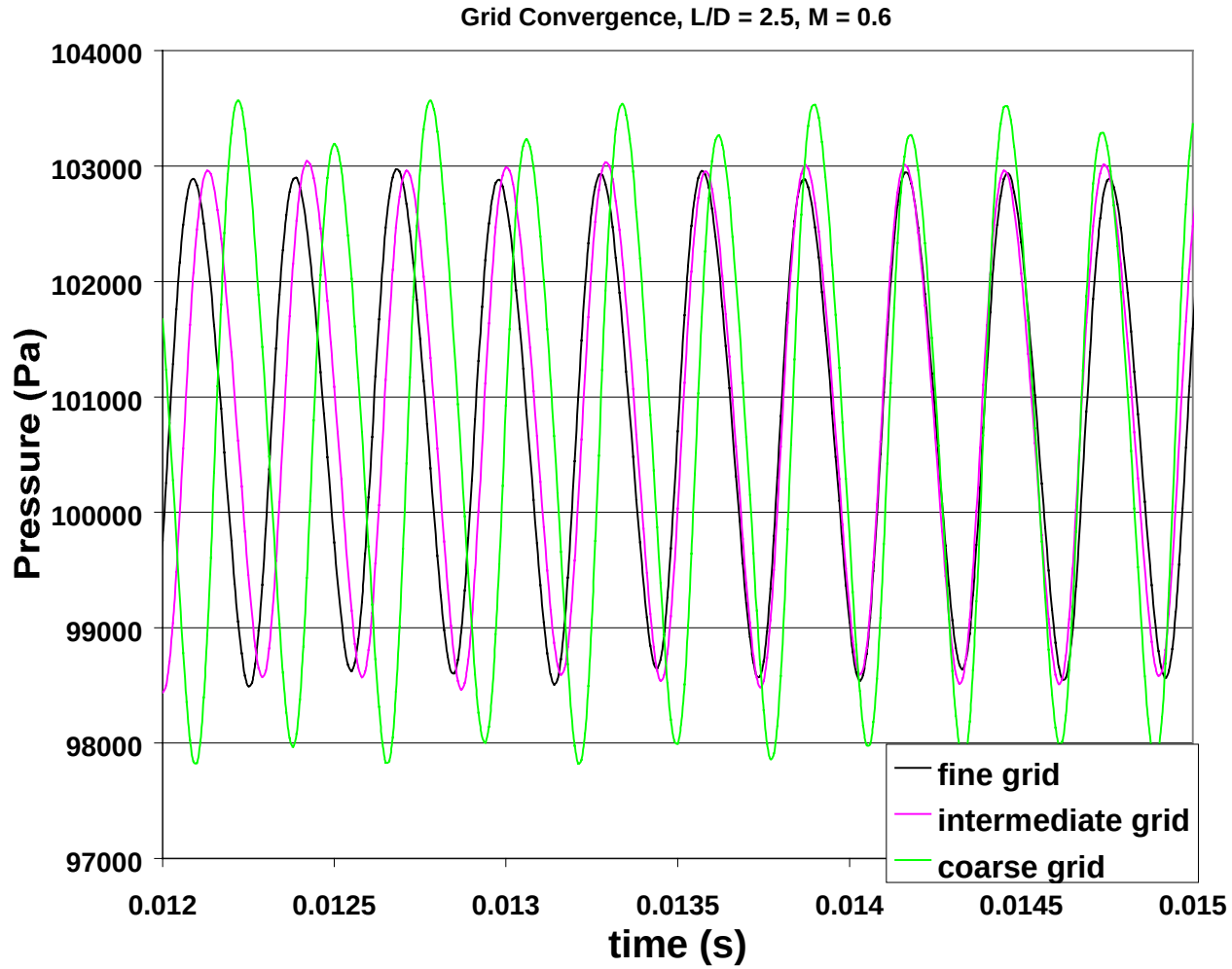

Figure 5.47 Grid Convergence Study, Pressure Oscillations on Floor of Cavity L/D = 2.5, M = 0.6

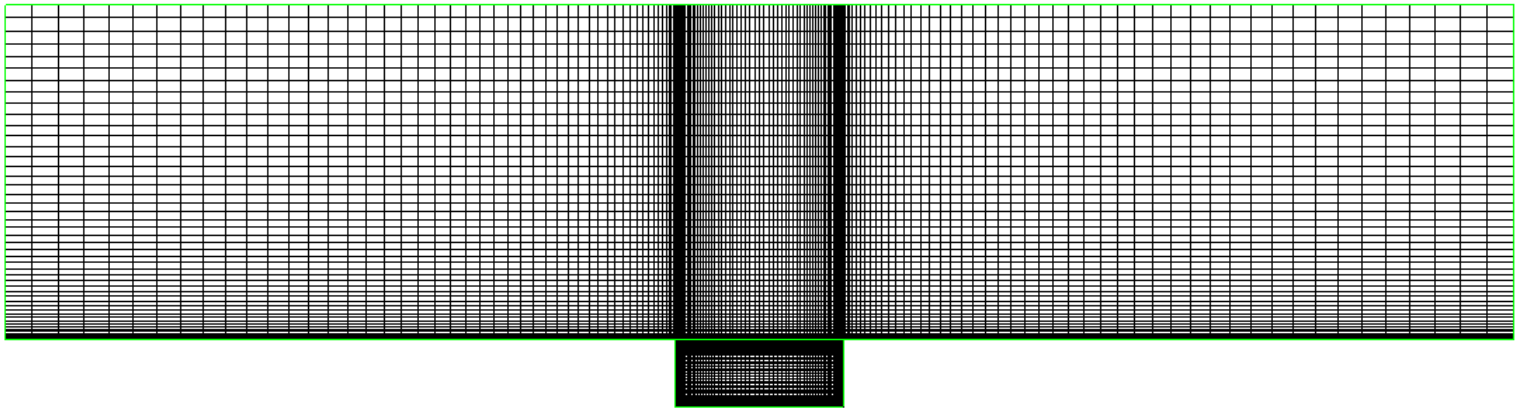

Figure 5.48 Fine Grid for Cavity L/D = 2.5 Geometry

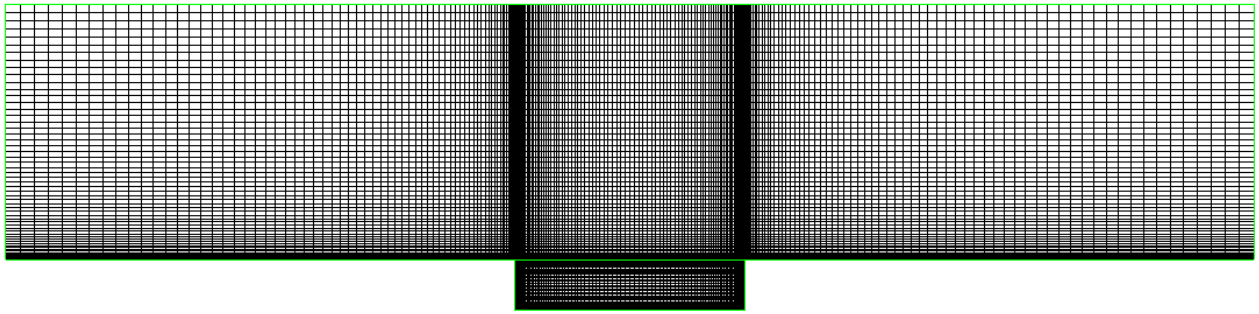

Figure 5.49 Fine Grid for Cavity L/D = 4.5 Geometry

The unsteady numerical simulations for the cavity were run on the CFD-ACE(U) commercial software. Second order differencing was used to solve for the velocities and a first-order differencing scheme was employed to solve for the turbulence quantities. The Crank-Nicholson scheme with a blending of 0.7 was used for the time stepping. The k-ε model was used to obtain turbulence closure. Experimental values of turbulence intensity obtained at positions upstream of the cavity were used as inlet boundary conditions in the numerical simulations. The sections following detail the dynamic pressure results and velocity field results obtained by CFD as compared with the corresponding data obtained experimentally.

5.2.4 Boundary Layer Comparisons

The boundary layer profiles were extracted from the numerical simulations at a position 0.0127 m (0.5 inch) upstream of the leading edge of the cavity for Mach numbers of 0.4, 0.57 and 0.6 respectively. The position corresponded to the position of boundary layer measurements made with the PIV system. The comparison of the numerical boundary layer profiles for Mach numbers 0.4, 0.57, and 0.6 with the experimental boundary layer profiles are shown in figures 5.50, 5.51 and 5.52 respectively. The comparison of the boundary layer thickness, displacement thickness, momentum thickness and shape factor for the experiments and numerical simulations can be found in table 5.2. From the comparison, it can be observed that the experimentally measured boundary layer profiles differ from the numerically simulated boundary layer profiles near the wall. This may be due to the fact that the two-dimensional, numerically simulated boundary layers were unaffected by the unsteadiness found in the three-dimensional flow field of the wind tunnel. The boundary layer profile close to the wall contains the kinetic energy available at the onset of the formation of the shear layer. This profile determines the stability criteria of the shear layer and the rate of growth of instabilities along the cavity length. Therefore, the boundary layer profile immediately upstream of the cavity leading edge plays an important role in the growth of

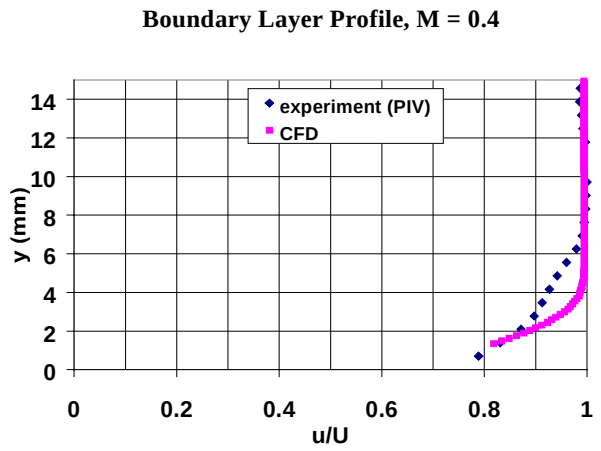

Figure 5.50 Numerically Simulated Boundary

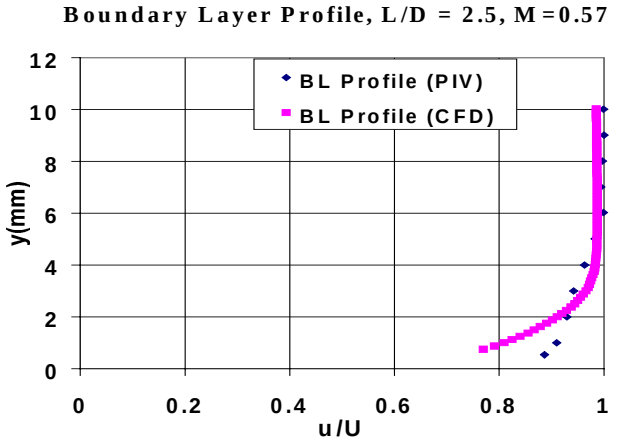

Figure 5.51 Numerically Simulated Boundary Layer Profile, M = 0.57

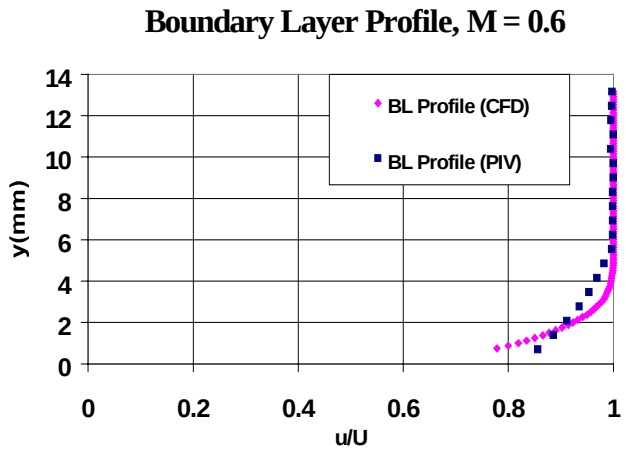

Figure 5.52 Numerically Simulated Boundary Layer Profile, M = 0.6

Table 5.2 Comparison of Boundary Layer Data

Mach	δ (mm), PIV	δ (mm), CFD	δ^* (mm), PIV	δ^* (mm), CFD	θ (mm), PIV	θ (mm), CFD	H, PIV	H, CFD
0.4	6.93	5.46	0.85	0.72	0.79	0.65	1.08	1.11
0.57	6.03	5.13	0.72	0.61	0.68	0.56	1.06	1.09
0.6	5.54	4.63	0.62	0.55	0.60	0.52	1.03	1.05

the shear layer and the nature of its interaction with the cavity. Therefore, the differences observed between the experimental and numerical results is a direct consequence of the differences in their corresponding upstream boundary layer profiles near the wall.

5.2.5 Numerically Simulated Pressure Histories

In the numerical simulations, a pressure monitor was placed on the floor of the cavity of L/D = 2.5 at a distance of L = 2D (0.0381 m) from the leading edge of the cavity. This corresponded to the position of the pressure transducer on the floor of cavity of L/D = 2.5 in the dynamic pressure measurements. The numerical simulations were run for freestream Mach numbers of 0.3, 0.4, 0.5, 0.57 and 0.6 respectively. Unsteady pressure data points were obtained at time intervals of 1×10^{-5} s corresponding to a sampling rate of 100000 data points per second. Time histories and the power spectra of the pressure data are shown in Figures 5.53 (a-e) and 5.54 (a-e) respectively. As is evident from the time history of the pressure data for freestream M = 0.3 (figure 5.53(a)), the flow is not coherent with the cavity geometry at this speed. The lack of coherent interaction between the flow and the cavity fails to produce self-sustained oscillations. Figure 5.53 (b) shows that the onset of self-sustained oscillations occurs at M = 0.4. A visual inspection of the time histories shows that the frequency of oscillations changes as the Mach number increases. More information about the exact values of frequency can be obtained by performing a Fast Fourier Transform (FFT) on the time history data.

Figures 5.54 (a-e) depict the corresponding power spectra of the pressure time histories shown in figures 5.53 (a-e). It is observed from the power spectra that the numerical onset of oscillations occurs at a Mach number lower that that observed in experiments. This discrepancy between the experiments and the numerical simulations may be explained as follows. For laminar boundary layers, the onset of oscillations in a given cavity geometry occurs above a certain value of the ratio L/θ, where L is the cavity length and θ is the momentum thickness [27]. This implies

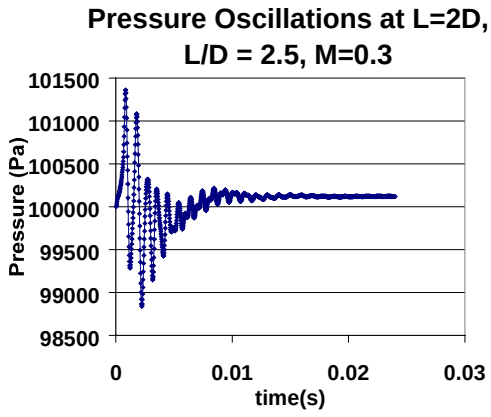

(a)

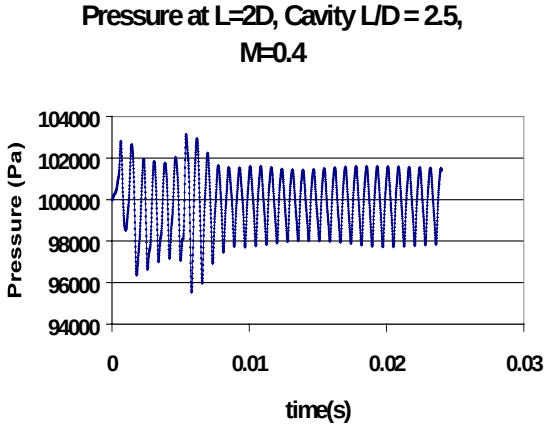

(b)

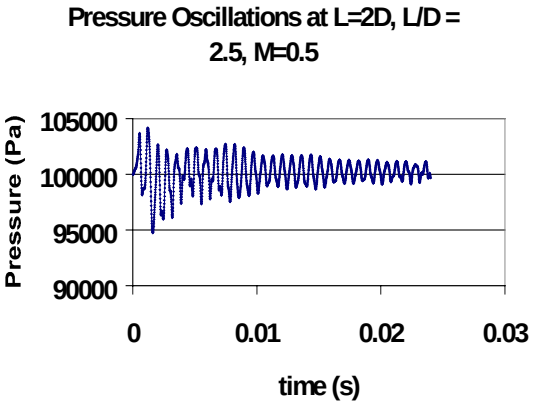

(c)

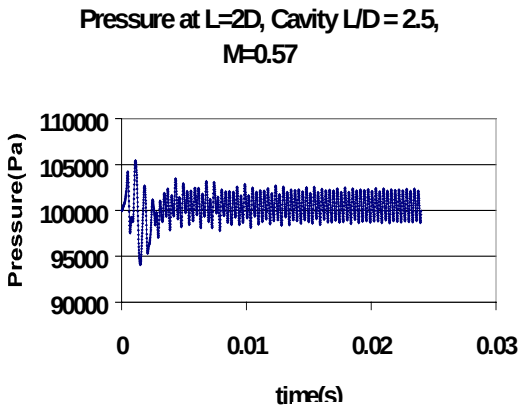

(d)

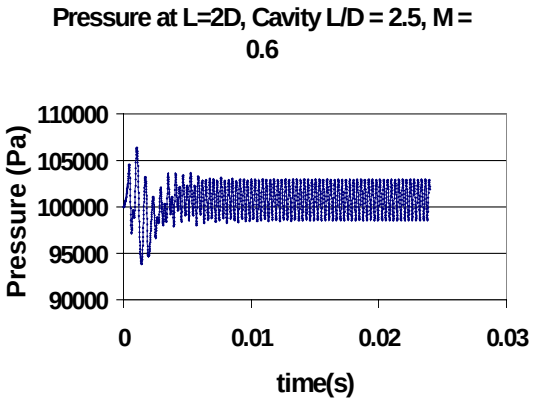

(e)

Figure 5.53 Pressure Time History at L=2D, Cavity L/D = 2.5, (a) M=0.3, (b) M = 0.4, (c) M = 0.5, (d) M = 0.57, (e) M = 0.6

(a)

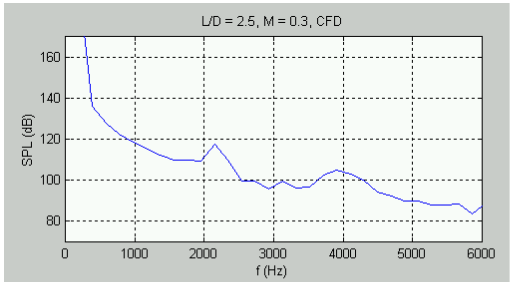

(b)

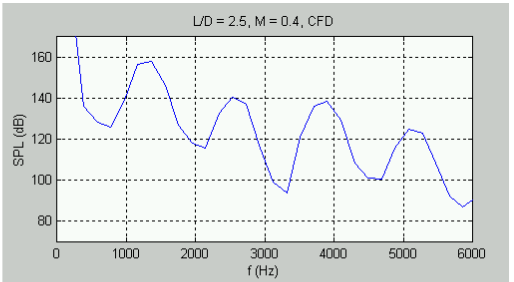

(c)

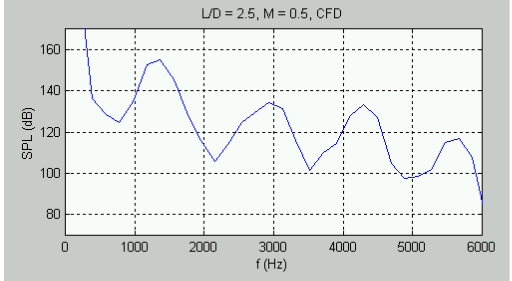

(d)

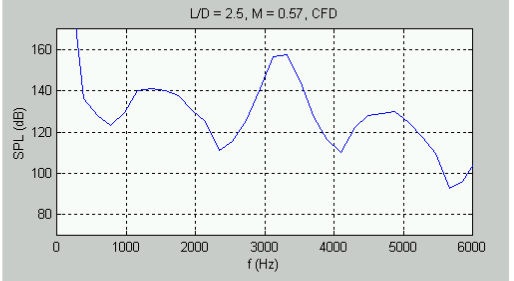

(e)

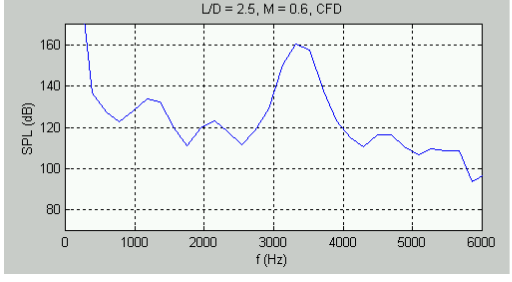

Figure 5.54 Power Spectra of the Pressure Time History, Cavity L/D = 2.5, (a) M = 0.3, (b) M = 0.4, (c) M = 0.5, (d) M = 0.57, (e) M = 0.6

that a lower value of the momentum thickness for a given Mach number in either of the numerical simulations or the experiments is indicative of an earlier onset of oscillations. By analogy, for turbulent boundary layers, as is the case in this study, smaller momentum thickness values shown by numerical simulations as compared to momentum thickness values measured by experiments (table 5.2) result in the earlier onset of oscillations in numerical simulations.

The power spectrum of M = 0.3 (figure 5.54 (a)) does not produce a well-defined SPL peak and this corresponds to the absence of self-sustained oscillations on the floor of the cavity as is evident from figure 5.53 (a). The power spectrum for a Mach number of 0.4 shows SPL peaks corresponding to frequencies of 1269 Hz, 2539 Hz, 3906 Hz, and 5175 Hz. The four frequencies correspond to the first four Rossiter modes of oscillation respectively. The dominant peak at 1269 Hz has a SPL of 160 dB as compared to the experimentally measured peak at 1139 Hz that is ill defined, and has an amplitude 140 dB (figure 5.15 (d)). The frequency of the numerically predicted peak agrees closely with the experiments. However, the SPL obtained by the numerical simulations is about 14% off the experimentally measured SPL. The lower value of the SPL measured in the experiments may be due to the three dimensional nature of the shear layer oscillation over the length of the cavity, whereas the numerical computations were performed in a two- dimensional domain. The numerical power spectra show a mode switch between freestream Mach numbers 0.5 and 0.57 (figures 5.54 (c) and (d)), whereas the experimental power spectra show mode switching between Mach numbers 0.57 and 0.6 (figures 5.15 (g) and (h)). The occurrence of mode switching at a lower Mach number for numerical spectra as compared to the experimental spectra is consistent with the observation that, for numerical simulations, the onset of oscillations occurs at a lower Mach number too. The numerical simulations switch from the first mode (f = 1269 Hz, figure 5.54 (c)) at M = 0.5 to the second mode (f = 3222 Hz, figure 5.54 (d)) at M = 0.57. However, the experimental spectra show that the cavity oscillations switch from the third mode (f = 4722 Hz, figure 5.15 (g)) at M = 0.57 to the first mode (f = 1617 Hz, figure

5.15 (h)) at M = 0.6. The phenomenon of mode switching occurs as a result of the non-linear growth of the unstable shear layer over the cavity. It is known that the higher modes become dominant over the fundamental mode at a distance well into the non-linear region [13].

Figures 5.55 (a-e) display the time histories of the pressure oscillations on the floor of the cavity L/D = 4.5 at positions L = 2D (0.0381 m) and L = 4D (0.0762 m) from the leading edge of the cavity. The positions of the numerical pressure monitors corresponded to the position of the pressure transducers on the floor of cavity in the dynamic pressure measurements. Unsteady pressure data points were obtained at time intervals of 2×10^{-5} s corresponding to a sampling rate of 50000 data points per second. Figure 5.55 (a) shows that the cavity is not coupled with the flow field at a freestream Mach number of 0.3. The onset of self-sustained oscillations occurs at a Mach number of 0.4 (figure 5.55 (b)). For each Mach number, the amplitude of the pressure oscillation for the pressure monitor placed at L = 4D, is higher than the amplitude measured by the pressure monitor placed at L = 2D. This observation is consistent with the fact that the pressure monitor at L = 4D is nearer to the trailing edge of the cavity than the pressure monitor at L = 2D. Another important observation made from the time histories is that the pressure signal at L = 4D leads the pressure signal at L = 2D. The time lag is equal to the amount of time that is required for an acoustic wave to travel the distance between the pressure monitors. This numerical finding indicates the upstream propagation of an acoustic wave inside the cavity as postulated by Rossiter's theory for cavity oscillations [5]. This upstream traveling acoustic wave modulates the shear layer at its separation point in a feedback cycle, and is instrumental in the selective amplification of frequencies within the cavity. Figures 5.56 (a-j) exhibit the power spectra for the pressure signals obtained at L = 2D and L = 4D on the floor of cavity L/D = 4.5. As was expected by inspecting the time history for M = 0.3 in figure 5.55 (a), the corresponding power spectrum for M = 0.3, figure 5.56 (a), shows the absence of a well-defined SPL peak. The spectra for M = 0.4, 0.5, 0.57, and 0.6 all show the existence of at least the first four modes of

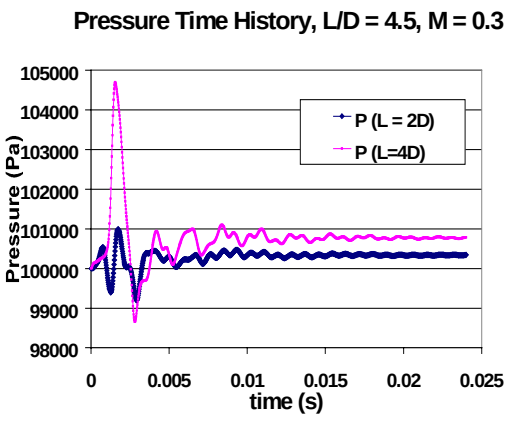

(a)

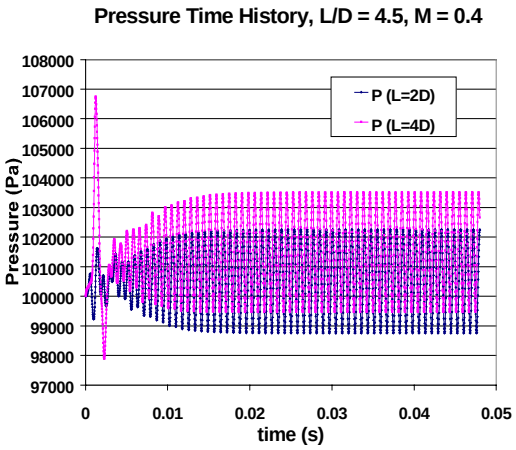

(b)

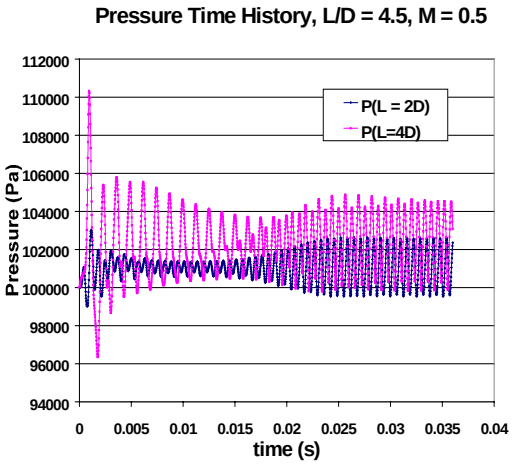

(c)

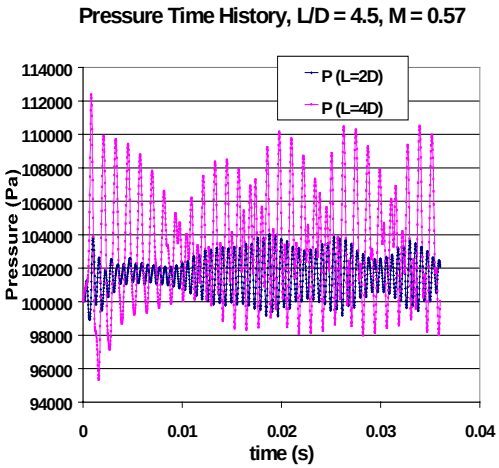

(d)

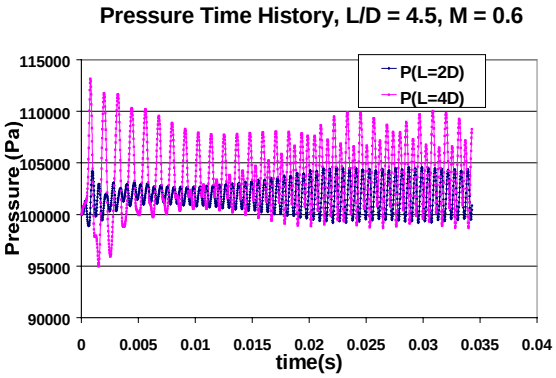

Figure 5.55 Pressure Time History at L=2D and L =4D, Cavity L/D =4.5, (a) M=0.3, (b) M = 0.4, (c) M = 0.5, (d) M = 0.57, (e) M = 0.6

(a)

(b)

(c)

(d)

(e)

(f)

(g)

(h)

(i)

(j)

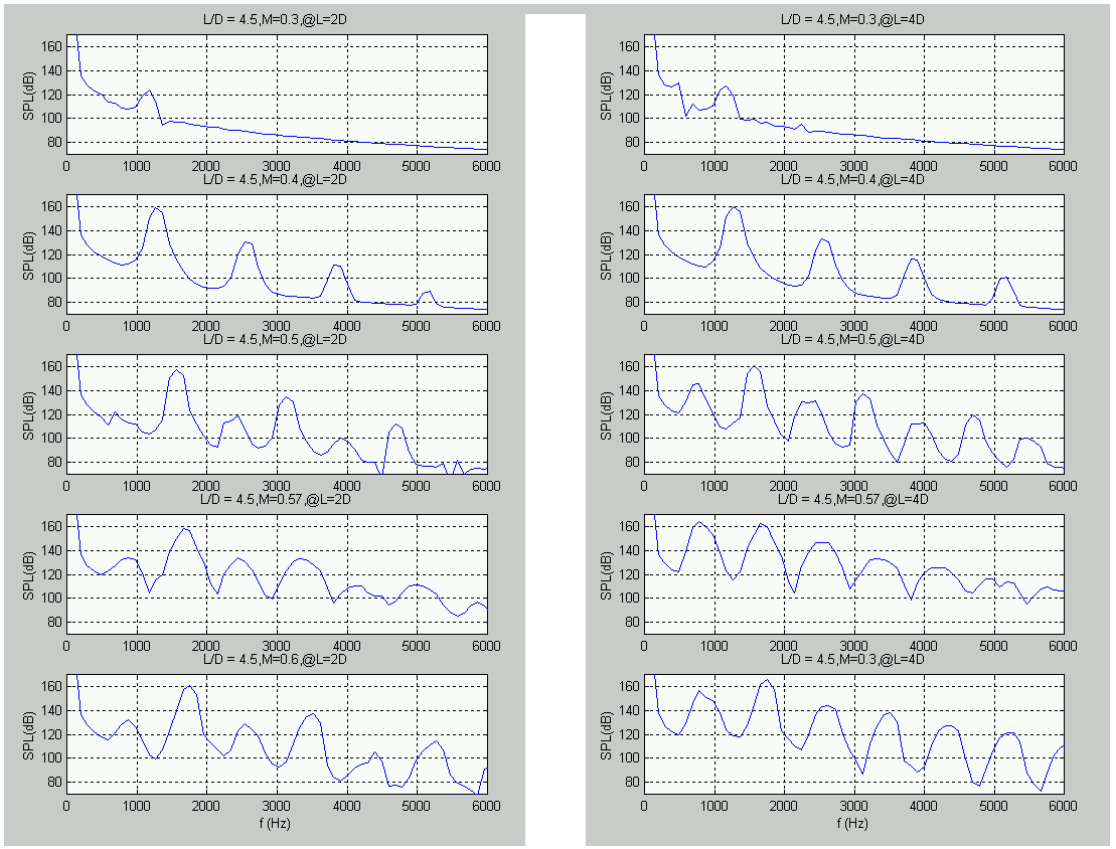

Figure 5.56 Power Spectra of the Pressure Time History, Cavity L/D = 4.5, (a) M = 0.3 at L=2D, (b) M = 0.3 at L = 4D, (c) M = 0.4 at L=2D, (d) M = 0.4 at L = 4D (e) M = 0.5 at L = 2D, (f) M = 0.5 at L = 4D, (g) M = 0.57 at L = 2D, (h) M = 0.57 at L = 4D, (i) M = 0.6 at L = 2D, (j) M = 0.6 at L = 4D

cavity oscillation. The dominant SPL peak in the spectra for M = 0.6 lies at a frequency of 1757 Hz and has an amplitude of about 160 dB for both the pressure monitors (figures 5.56 (i) and (j)). These values of the frequency and the SPL show excellent agreement with the corresponding experimental frequency and SPL values of 1863 Hz and 160 dB (figures 5.16 (i) and (j)) respectively. Also, in accordance with the experimental observations, for a given Mach number, the pressure monitor at L = 4D that is near the cavity trailing edge produces a higher level of background noise than the one at L = 2D.

The amplitude and frequency of the peaks were extracted from the spectra, and the non-dimensional Strouhal number, St (fL/U), of the oscillations was calculated. These were compared to the modified Rossiter's formula

$$St = \frac{fL}{U} = \frac{m - n}{1/K_v + \dfrac{M_\infty}{\sqrt{1 + \dfrac{\gamma - 1}{2} M_\infty^2}}}$$

Figure 5.57 shows the comparison of the numerically simulated data for cavity L/D = 2.5 and 4.5 with the Rossiter's formula. As seen in the figure, the agreement is very good, verifying that the numerical simulations of the cavity oscillations behave as expected.

5.2.6 Numerically Simulated Velocity Fields

In the following sections, flow field data obtained by numerical simulations is presented for cavity L/D ratio of 2.5 with the freestream Mach numbers set at 0.4, 0.5, 0.57 and 0.6 respectively. Velocity field data is also presented for cavity L/D ratio 4.5 for freestream Mach numbers of 0.4 and 0.6 respectively. The data is interpreted and analyzed using both instantaneous velocity fields and non-dimensional vorticity contours.

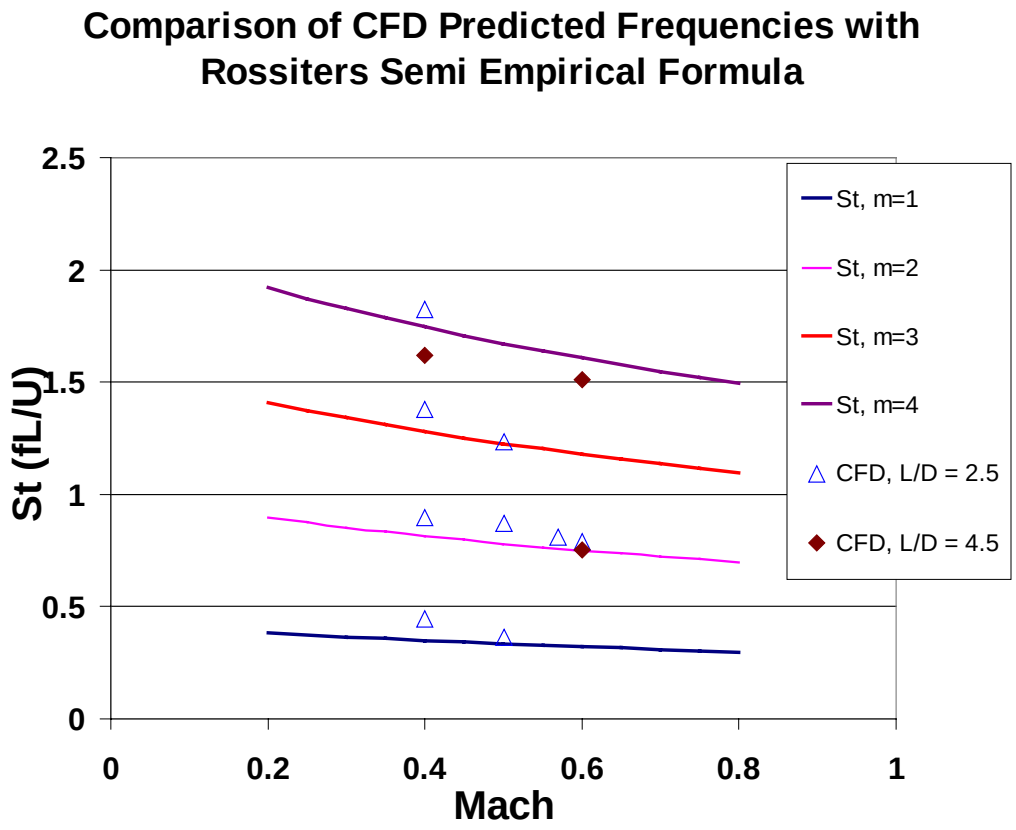

Figure 5.57 Comparison of Numerical Data with Rossiter's Semi-Empirical Formula

5.2.6.1 CFD, L/D = 2.5, M = 0.4

Figure 5.58 (a-f) plots the instantaneous non-dimensional vorticity contours for cavity L/D = 2.5 with the freestream Mach number set at 0.4. The six plots represent one cycle of cavity oscillations. The impingement of the shear layer with the downstream trailing edge is apparent from figure 5.58 (d). Figures 5.59 (a-f) show the corresponding velocity vectors. In accordance with experiments, the instantaneous velocity vectors show the existence of a downward oriented wall jet like flow adjacent to the lower half of the trailing edge of the cavity. A similar wall jet like flow is encountered near the floor of the cavity that extends well upstream of the trailing edge. This jet adjacent to the floor then turns in the upward direction over a short distance to feed the large entrainment demands of the shear layer. The velocity vectors in Figure 5.59 (d) show an upward oriented outflow of fluid at the trailing edge corner. This outflow is associated with the arrival of the cluster of vorticity as seen in Figure 5.58 (d). On the other hand, Figure 5.59 (c) plots the downward oriented inflow of fluid at the trailing edge corner. This is in accordance with the flow pattern seen in the experiments. However, there is only one strong non-stationary recirculation zone seen in the interior of the cavity unlike the two weak recirculation zones seen in the right half of the cavity in the experiments. It is likely that the turbulent viscosity in the simulations decrease the number of vortices resident in the cavity. The velocity contours plotted in figures 5.60 (a-f) display the oscillation of the shear layer that is responsible for the entrainment and ejection of fluid mass from the cavity.

5.2.6.2 CFD, L/D = 2.5, M = 0.5

In numerical simulations, the phenomenon of mode switching occurs between the Mach numbers of 0.5 and 0.57 unlike the experiments in which mode switching occurs between M = 0.57 and 0.6. Therefore, the numerically simulated flow field for M = 0.5 is presented in addition to the flow fields for M = 0.57 and M = 0.6.

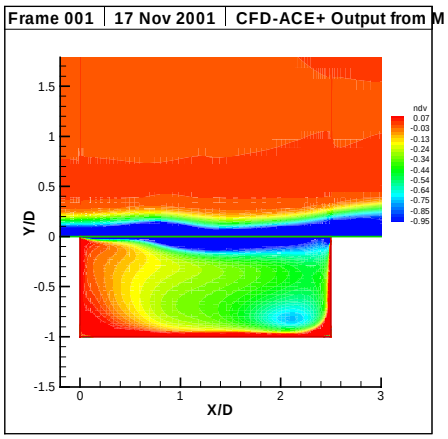

(a)

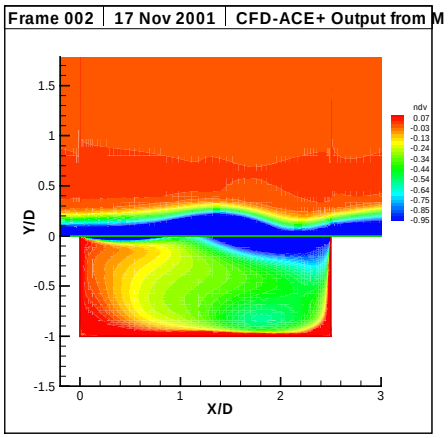

(b)

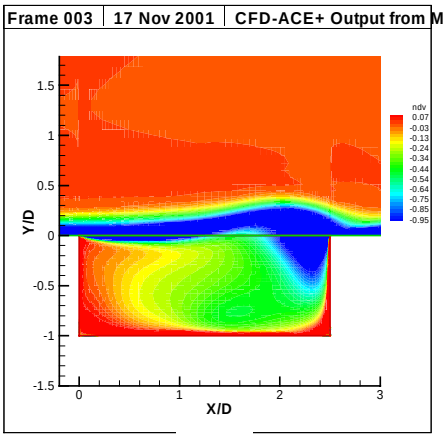

(c)

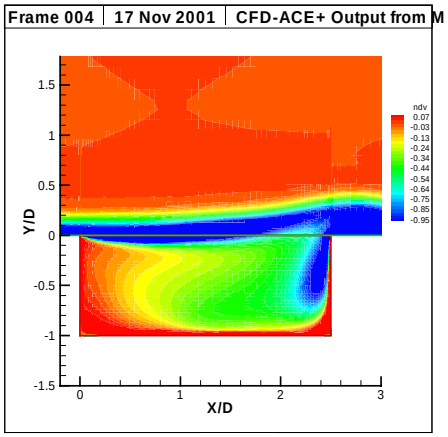

(d)

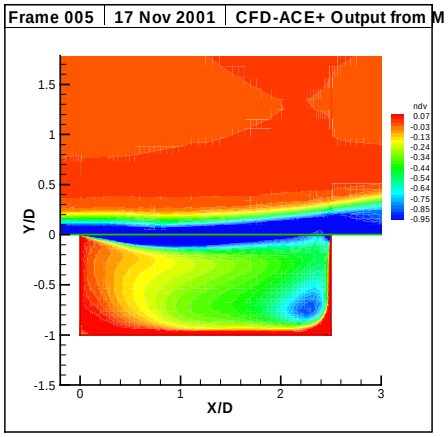

(e)

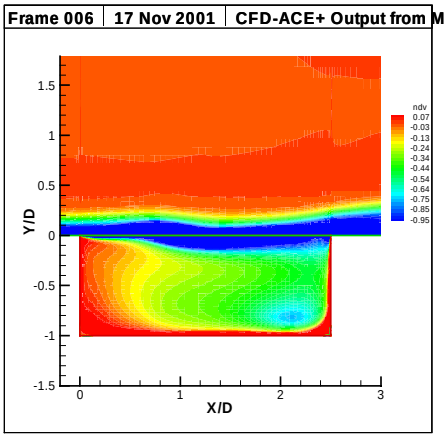

(f)

Figure 5.58 Numerically Simulated Instantaneous Non-Dimensional Vorticity Contours, Cavity L/D = 2.5, M = 0.4

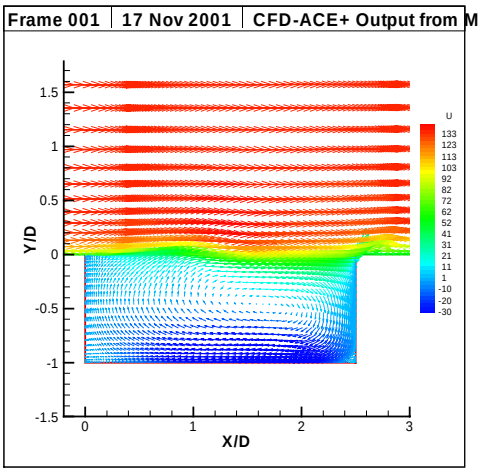

(a)

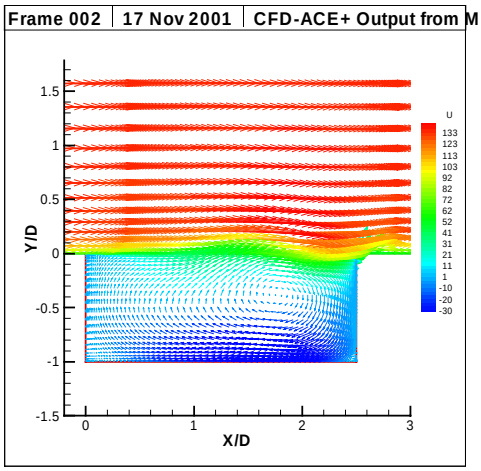

(b)

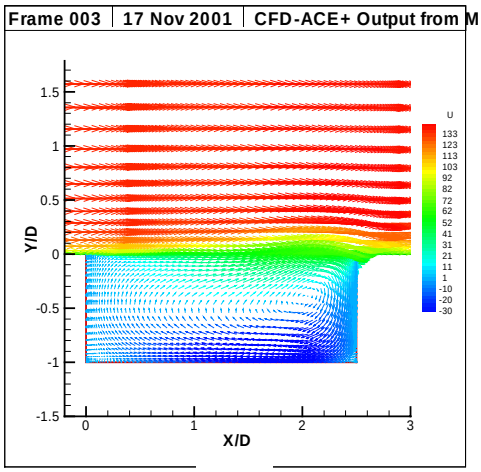

(c)

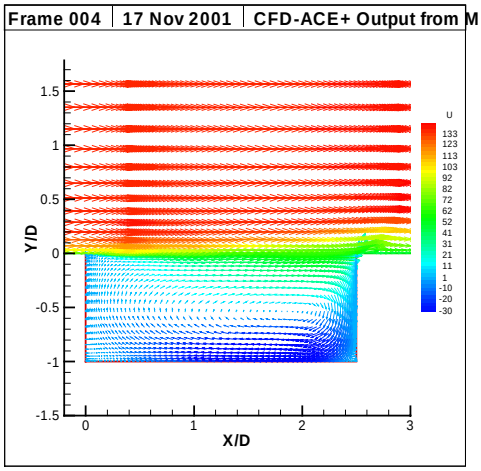

(d)

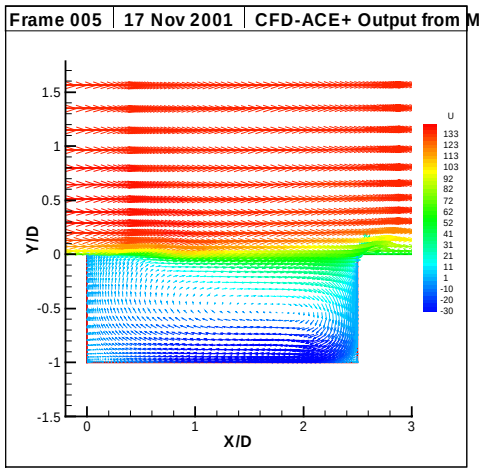

(e)

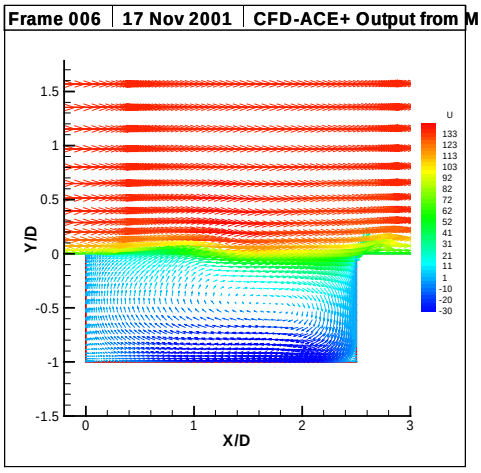

(f)

Figure 5.59 Numerically Simulated Velocity Vectors, Cavity L/D = 2.5, M = 0.4

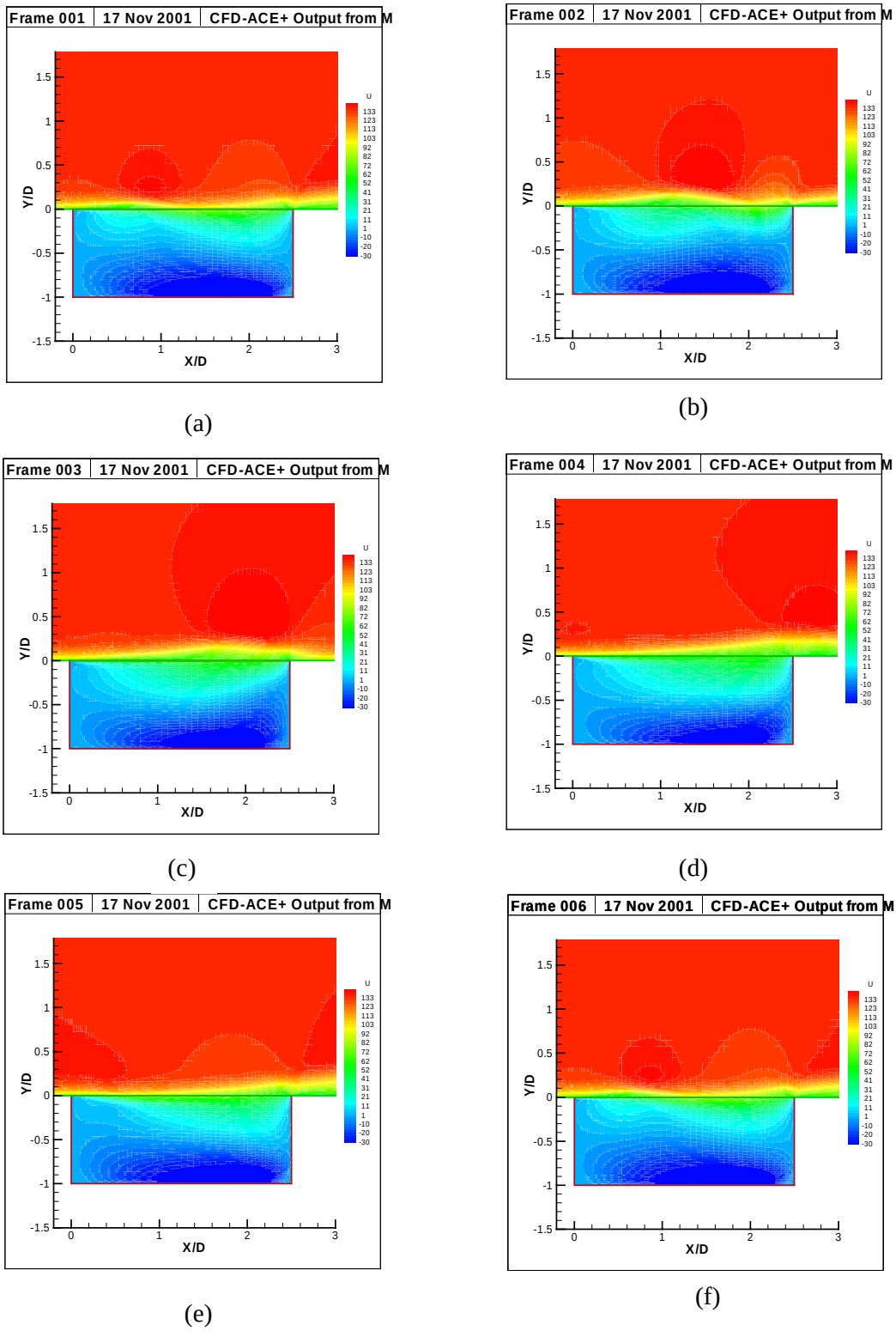

Figure 5.60 Numerically Simulated Instantaneous Velocity Contours, Cavity L/D = 2.5, M = 0.4

Figures 5.61 (a-f) present the non-dimensional vorticity contours over one oscillation cycle of the cavity L/D = 2.5 at a freestream Mach number of 0.5. The contours depict the spreading of the shear layer as it moves downstream. The impingement of the shear layer with the trailing edge of the cavity is noticeably less pronounced than that seen for M = 0.4 (figures 5.58 (a-f)). Also apparent is the relatively low amplitude of shear layer oscillations compared with the shear layer oscillation observed for M = 0.4. These observations may be an indication to the fact that the cavity flow is in transition. However, the highly non-linear growth of the shear layer that was thought to be reason for mode switching in the experimental results of M = 0.57 is not noticeable in the numerical simulation for M = 0.5; the Mach number at which mode switching takes place for numerical simulations. The velocity vectors (figures 5.62 (a-f)) show the usual wall jet like flows along the trailing edge, cavity floor and the leading edge of the cavity. A large recirculation zone centered in the right half of the cavity is also seen in figures 5.62 (a-f). The velocity contours plotted in 5.63 (a-f) depict the reduced amplitude of the shear layer oscillations very clearly.

5.2.6.3 CFD, L/D = 2.5, M = 0.57

Figures 5.64 (a-f) show the non-dimensional vorticity contours over one oscillation cycle for cavity L/D = 2.5 at a freestream Mach number of 0.57. The plots indicate that the vorticity is highly organized in the shear layer and that the oscillation cycle is well defined. Unlike the vorticity contours for M = 0.5 (figures 5.61 (a-f)), the impingement of the shear layer with the trailing edge of the cavity (figures 5.64 (d) and (e)) is prominent and the motion of the shear layer is well defined. This change in the non-dimensional vorticity contours for M = 0.57 indicates that the flow has switched modes and is no longer in the transitional mode seen in the results for M = 0.5. The velocity vectors plotted in figures 5.65 (a-f) exhibit the inflow and outflow of fluid at the trailing edge and the presence of a moving recirculation zone within the right half of the cavity.

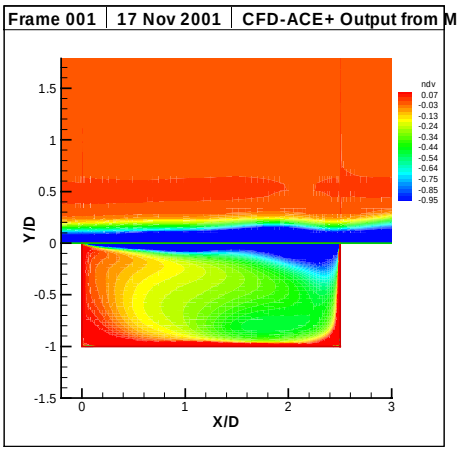

(a)

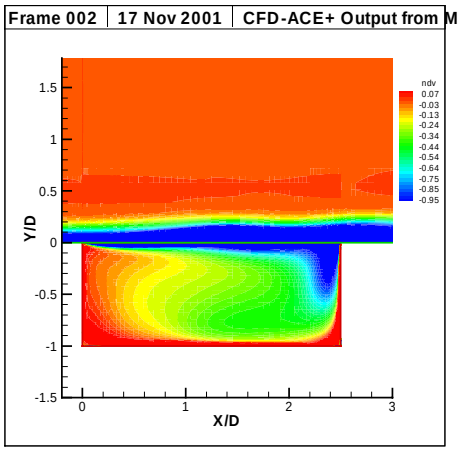

(b)

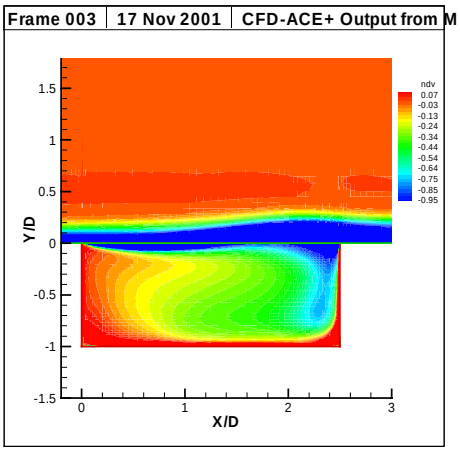

(c)

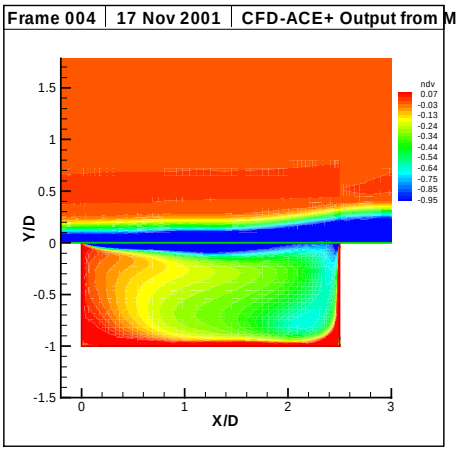

(d)

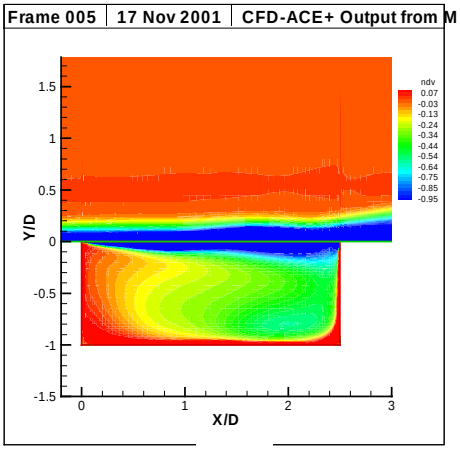

(e)

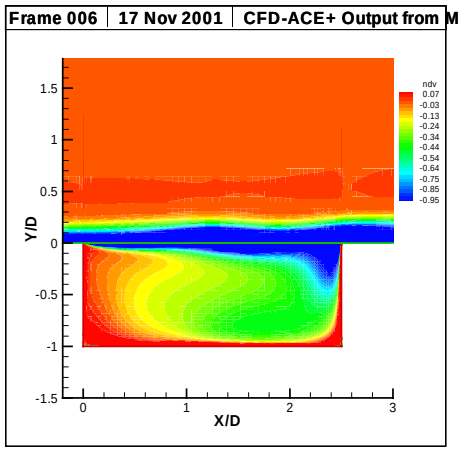

(f)

Figure 5.61 Numerically Simulated Instantaneous Non-Dimensional Vorticity Contours, Cavity L/D = 2.5, M = 0.5

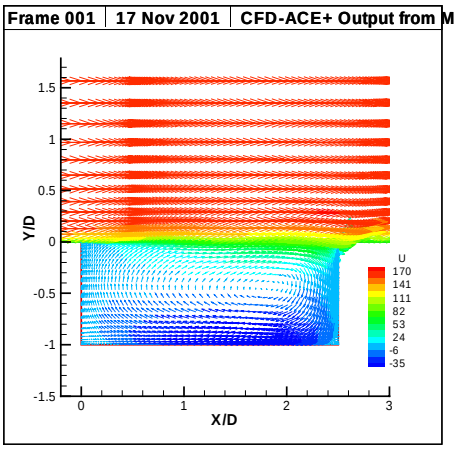

(a)

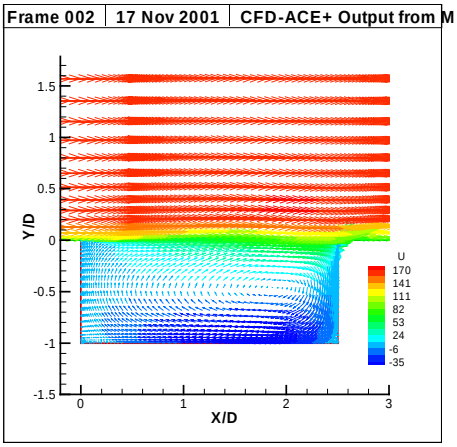

(b)

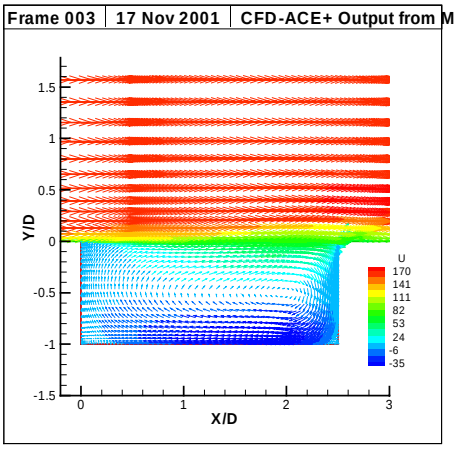

(c)

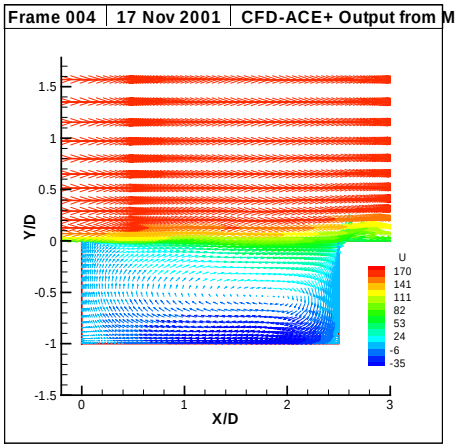

(d)

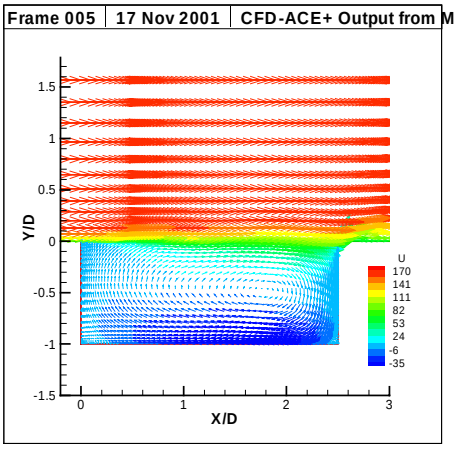

(e)

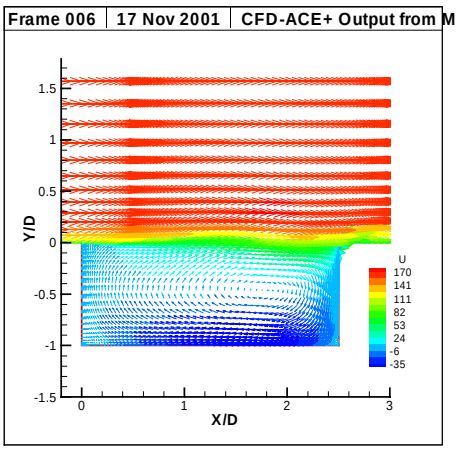

(f)

Figure 5.62 Numerically Simulated Velocity Vectors, Cavity L/D = 2.5, M = 0.5

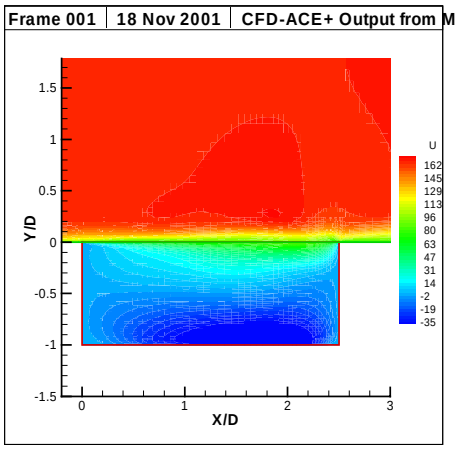

(a)

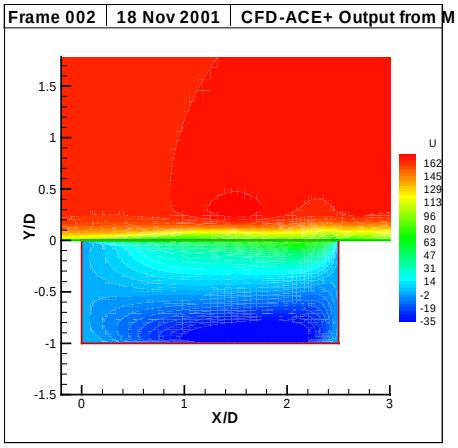

(b)

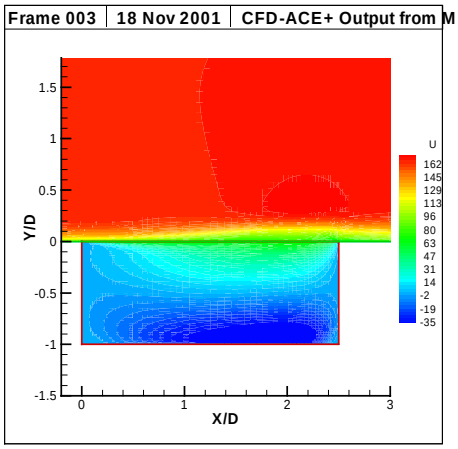

(c)

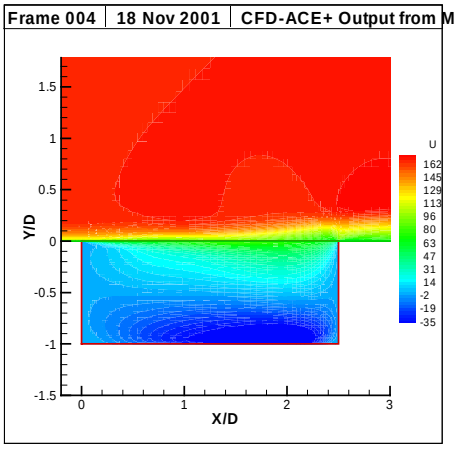

(d)

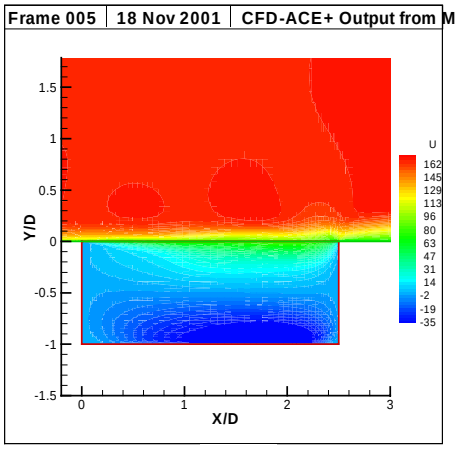

(e)

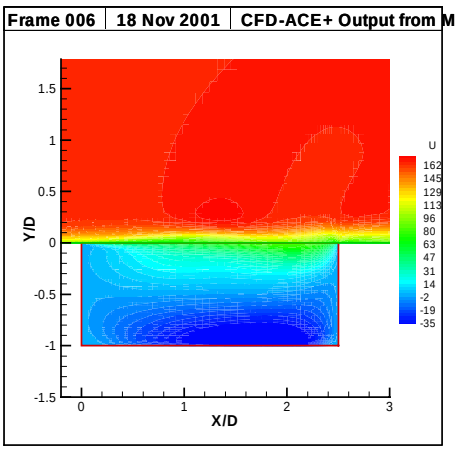

(f)

Figure 5.63 Numerically Simulated Instantaneous Velocity Contours, Cavity L/D = 2.5, M = 0.5

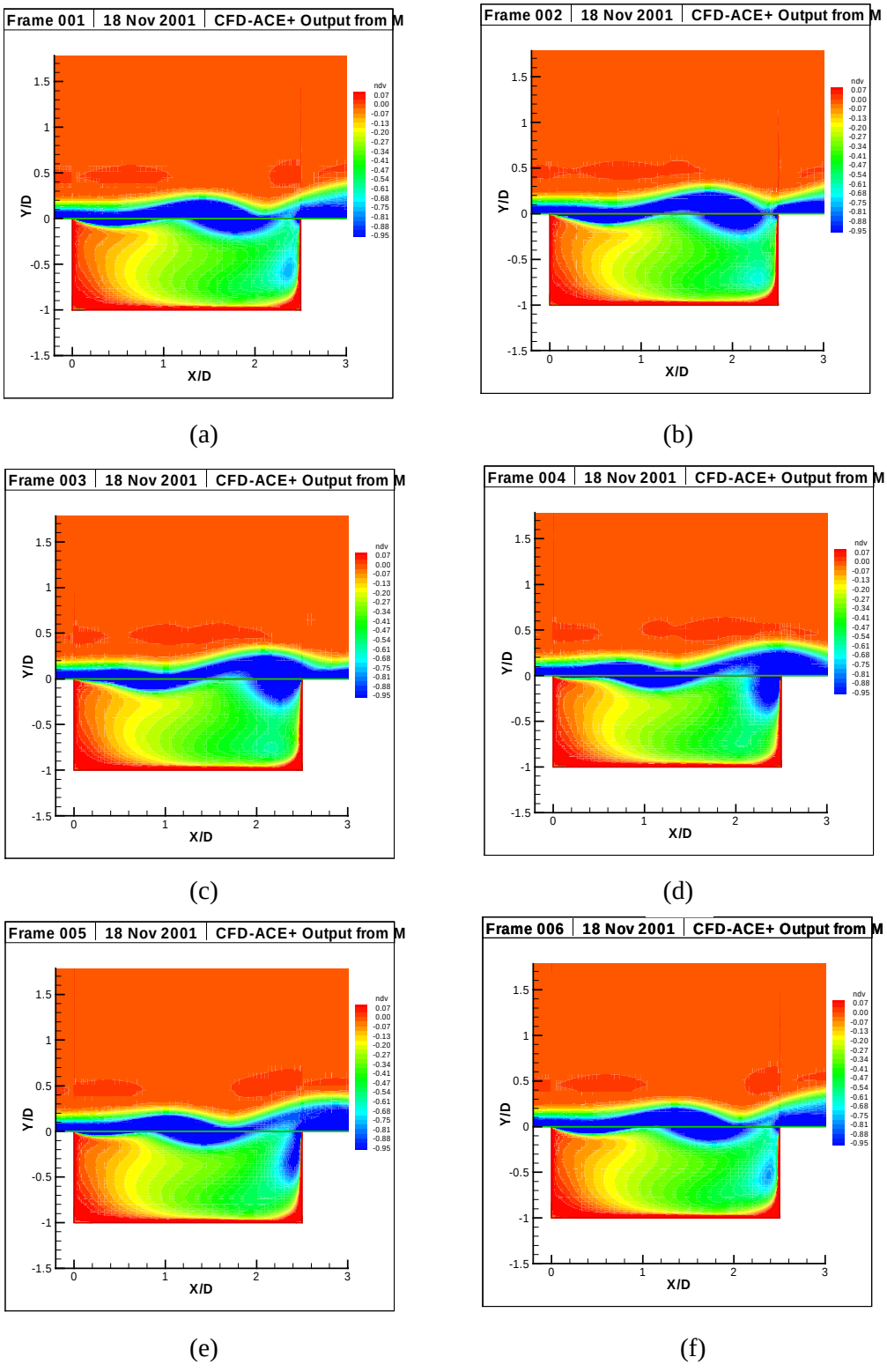

Figure 5.64 Numerically Simulated Instantaneous Non-Dimensional Vorticity Contours, Cavity L/D = 2.5, M = 0.57

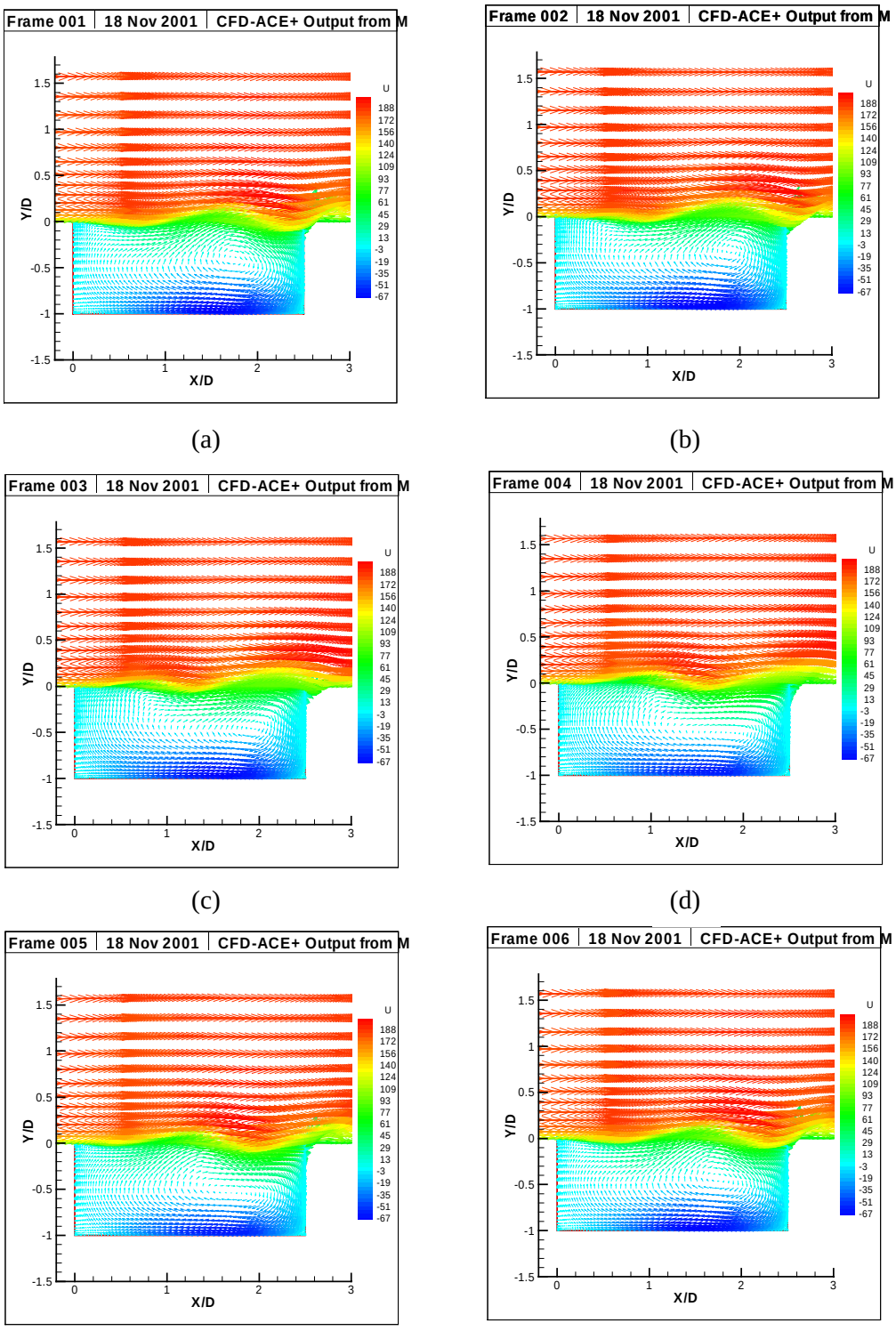

Figure 5.65 Numerically Simulated Velocity Vectors, Cavity L/D = 2.5, M = 0.57

The velocity contours (figures (5.66 (a-f)) demonstrate the motion of the shear layer along the length of the cavity.

5.2.6.4 CFD, L/D = 2.5, M = 0.6

The flow field for cavity L/D = 2.5 at a freestream Mach number of 0.6 exhibited similar trends to those seen for M = 0.57. The non-dimensional vorticity contours, velocity vectors, and velocity contours for cavity L/D = 2.5 at a freestream Mach number of 0.6 are depicted in figures 5.67 (a-f), 5.68 (a-f), and 5.69 (a-f) respectively over one cycle of oscillation.

5.2.6.5 CFD, L/D = 4.5, M = 0.4

The non-dimensional vorticity contours over one cycle of oscillation are plotted in figures 5.70 (a-f) for cavity L/D = 4.5 at a freestream Mach number of 0.4. The vorticity contours in the shear layer compare well with the experimental results shown in Figures 5.37 (a-f) for the corresponding cavity configuration. The velocity vectors plotted in figures 5.71 (a-f) show that a vortex is formed downstream of the leading edge that travels downstream and merges in a non-stationary recirculation zone that occupies the right half of the cavity. This is unlike the presence of a number of recirculation zones seen in the experiments (figures 5.37 (a-f)). The velocity contours plotted in figures 5.72 (a-f) show the characteristic motion of the shear layer.

5.2.6.6 CFD, L/D = 4.5, M = 0.6

Figures 5.73 (a-f) plot the non-dimensional vorticity contours of cavity L/D = 4.5 at a freestream Mach number of 0.6 over one oscillation cycle. The features are similar to the features seen in the case of cavity L/D = 4.5 at M = 0.4 (figures (5.70 (a-f)). The contours compare well with the experimental results shown in figures 5.42 (a-f) with the high values of vorticity concentrated in the shear layer of the cavity. The velocity vectors shown in figures 5.74(a-f)

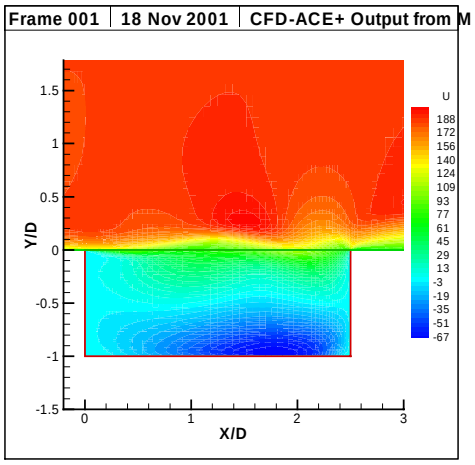

(a)

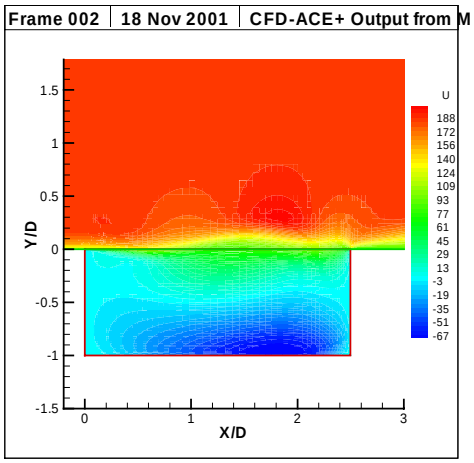

(b)

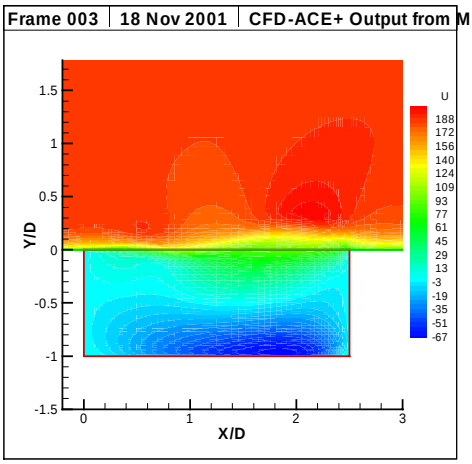

(c)

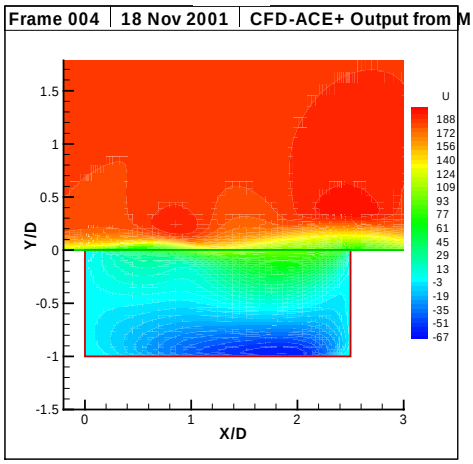

(d)

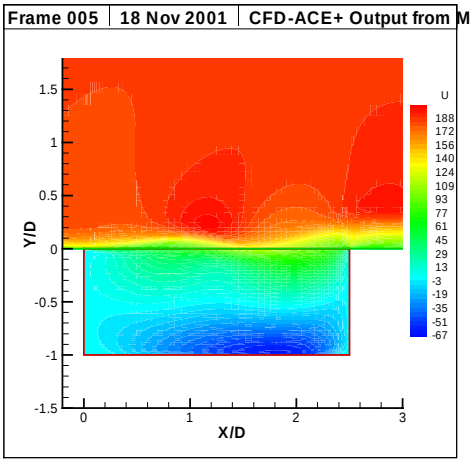

(e)

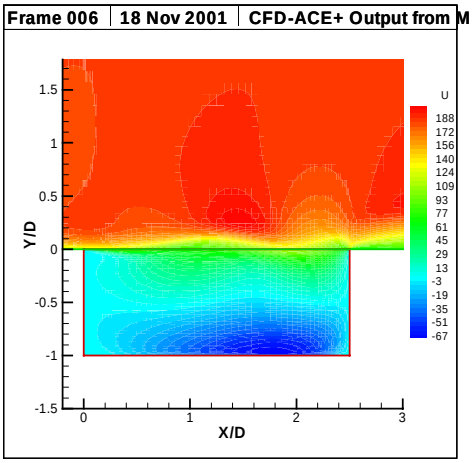

(f)

Figure 5.66 Numerically Simulated Instantaneous Velocity Contours, Cavity L/D = 2.5, M = 0.57

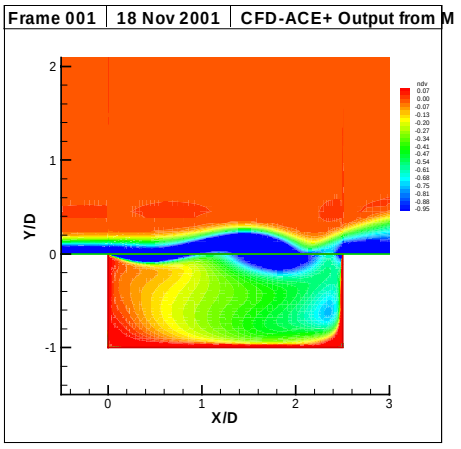

(a)

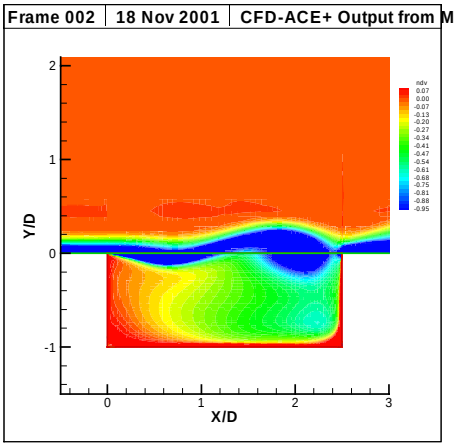

(b)

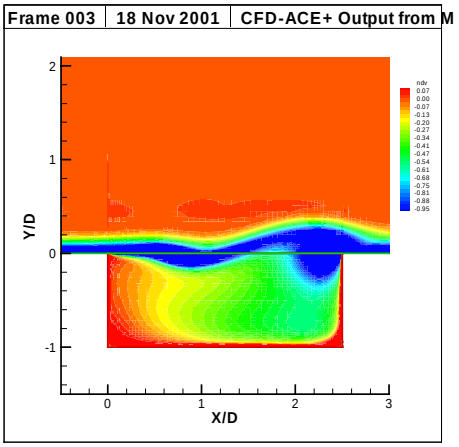

(c)

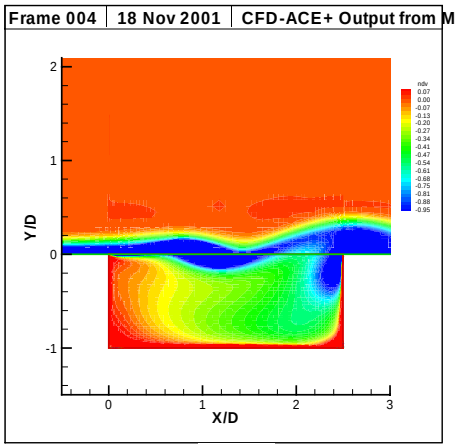

(d)

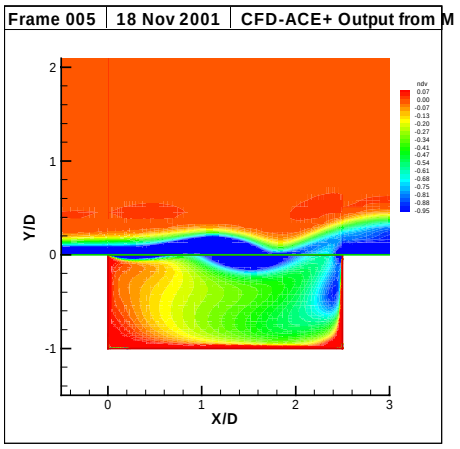

(e)

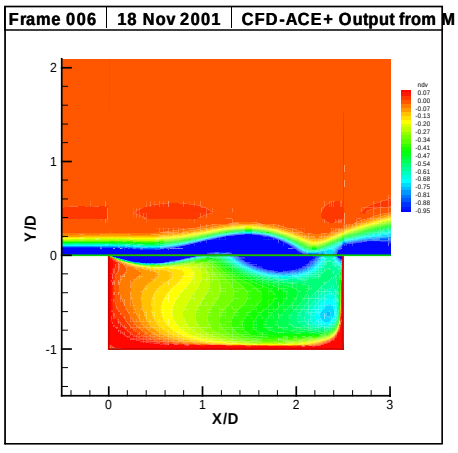

(f)

Figure 5.67 Numerically Simulated Instantaneous Non-Dimensional Vorticity

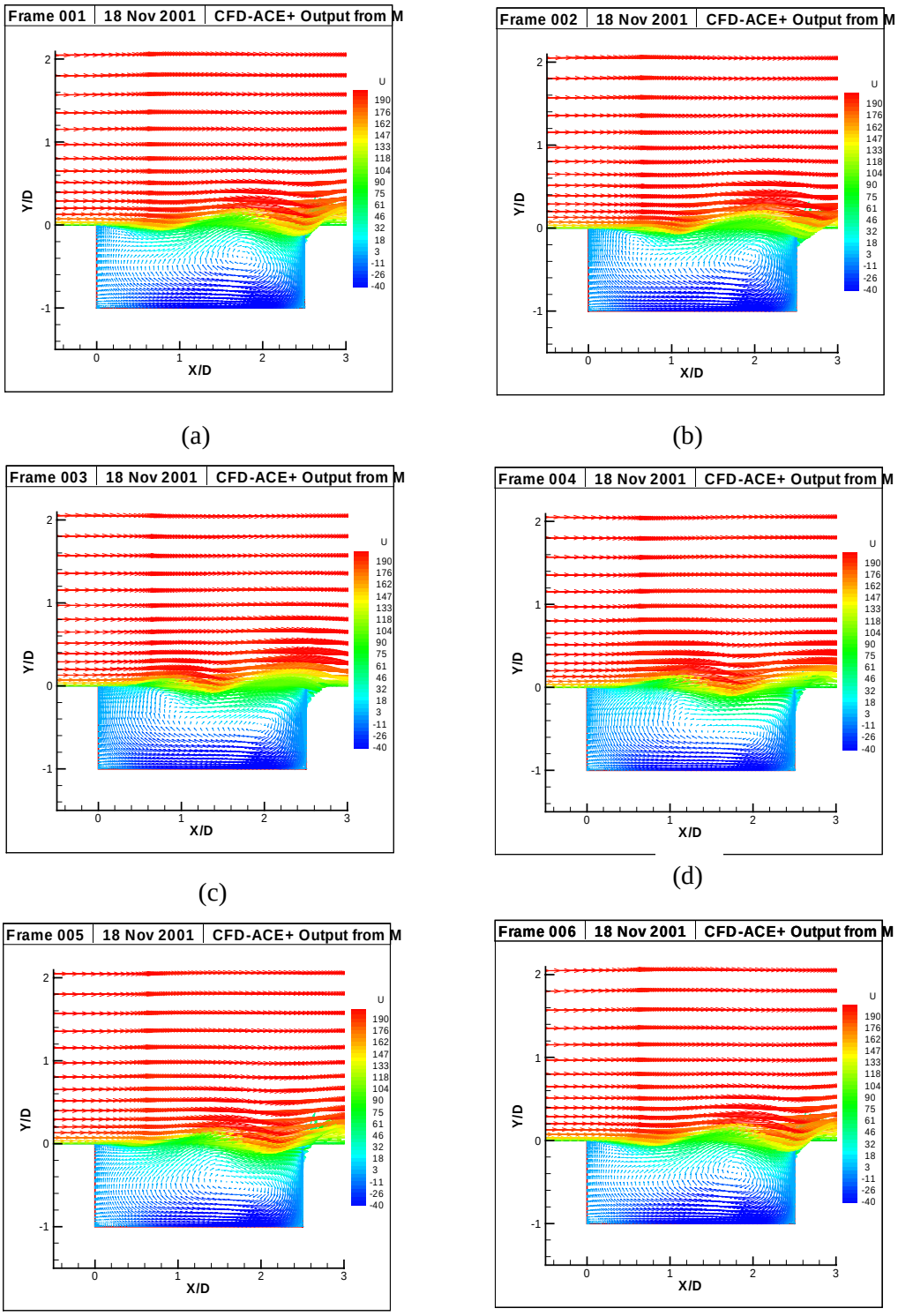

(a) (b)

(c) (d)

(e) (f)

Figure 5.68 Numerically Simulated Velocity Vectors, Cavity L/D = 2.5, M = 0.6

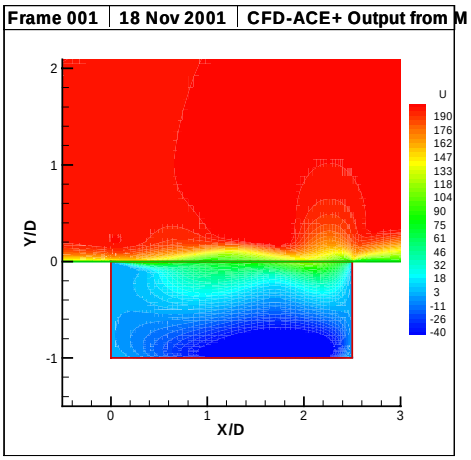

(a)

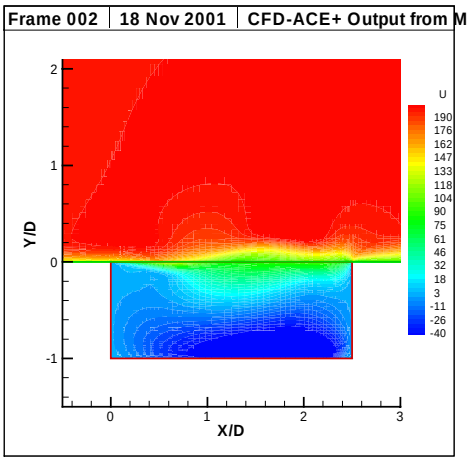

(b)

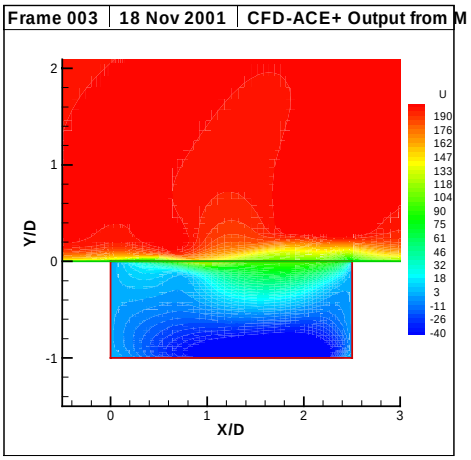

(c)

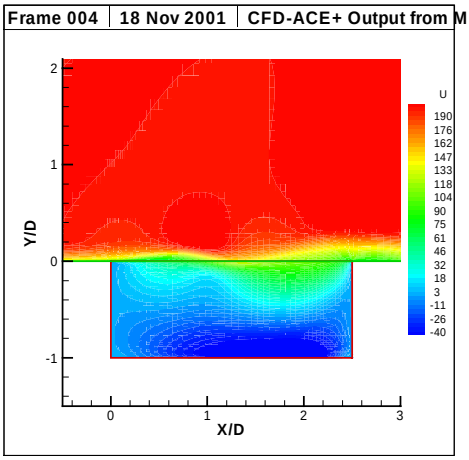

(d)

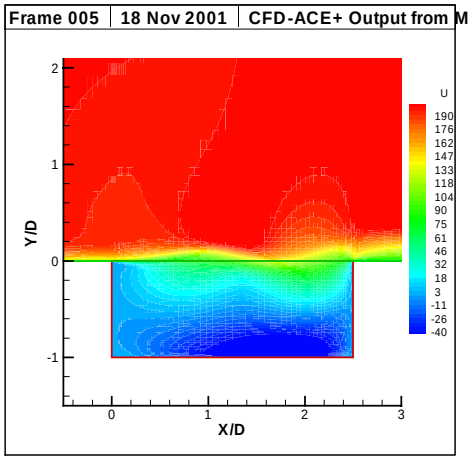

(e)

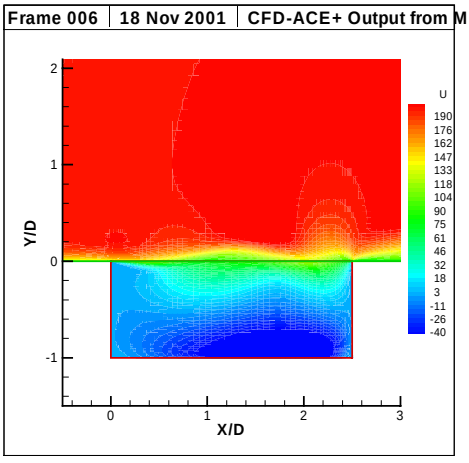

(f)

Figure 5.69 Numerically Simulated Instantaneous Velocity Contours, Cavity L/D = 2.5, M = 0.5

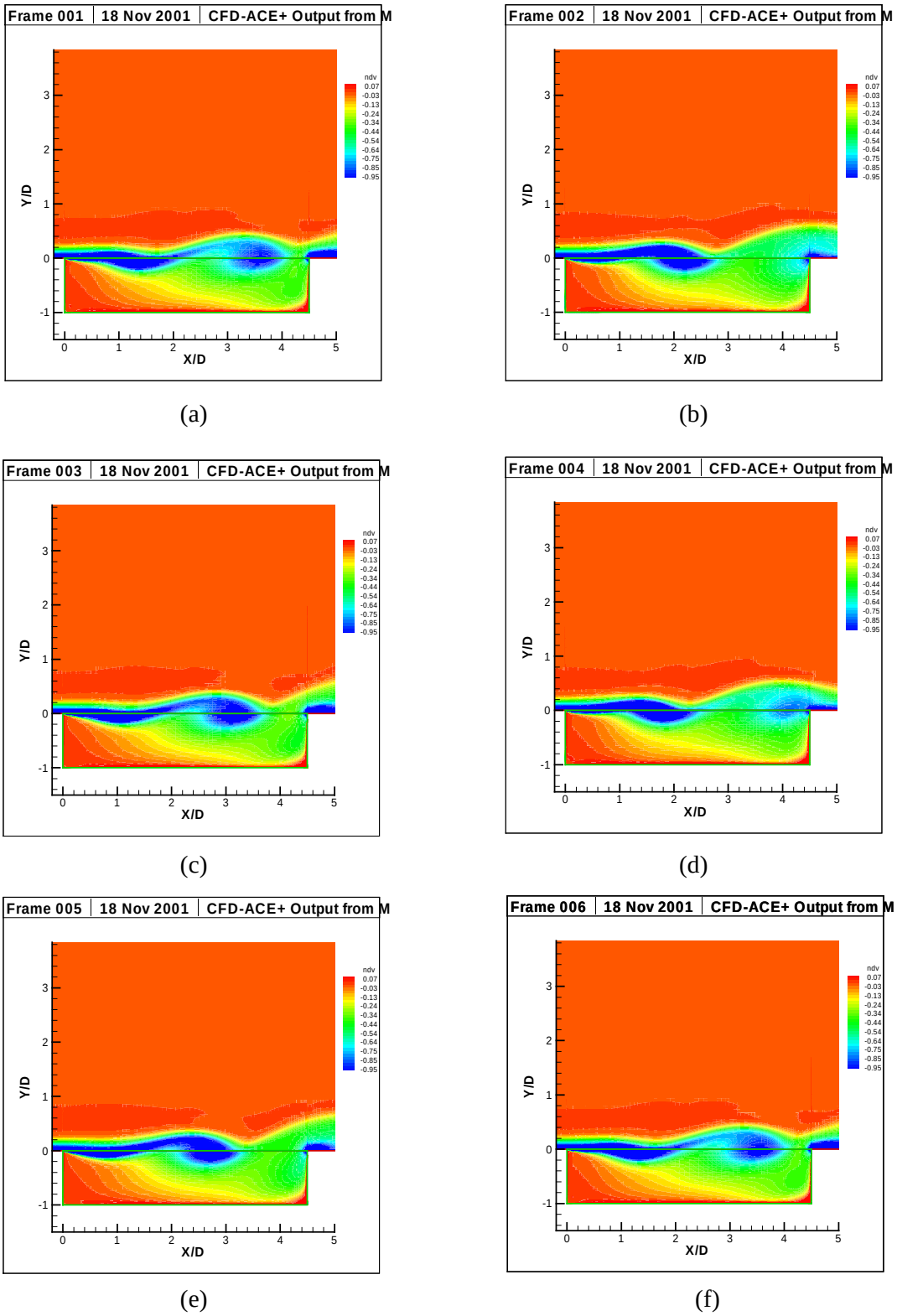

Figure 5.70 Instantaneous Non-Dimensional Vorticity Contours, Cavity L/D = 4.5, M = 0.4

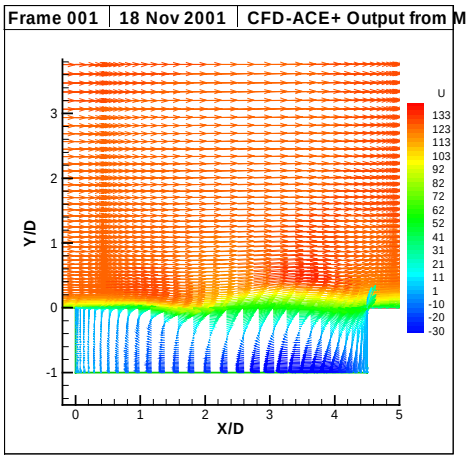

(a)

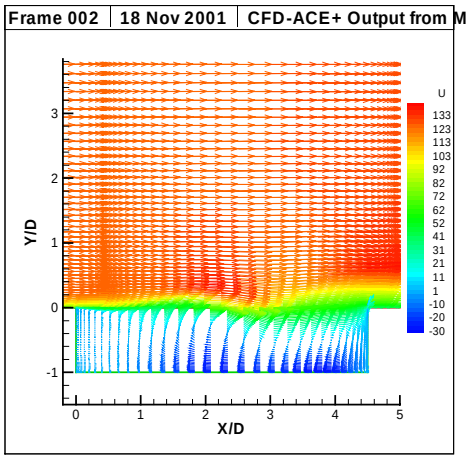

(b)

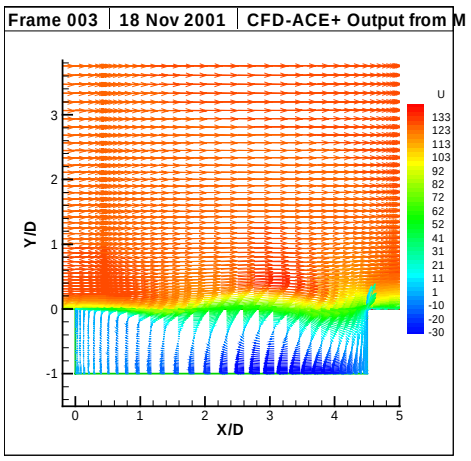

(c)

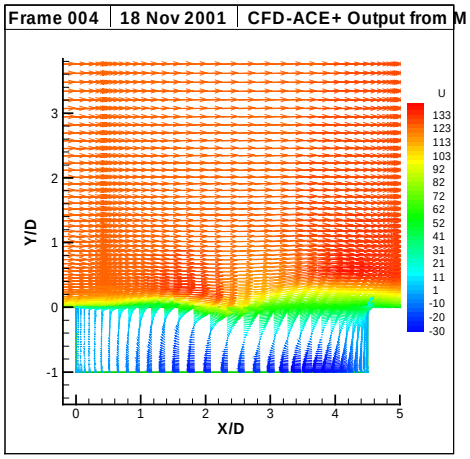

(d)

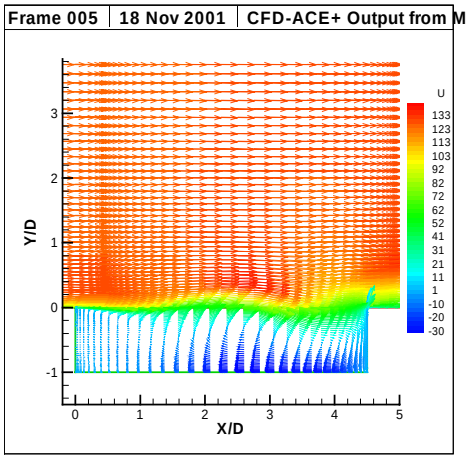

(e)

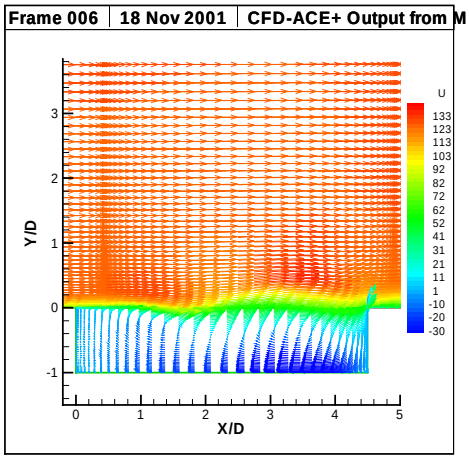

(f)

Figure 5.71 Numerically Simulated Velocity Vectors, Cavity L/D = 4.5, M = 0.4

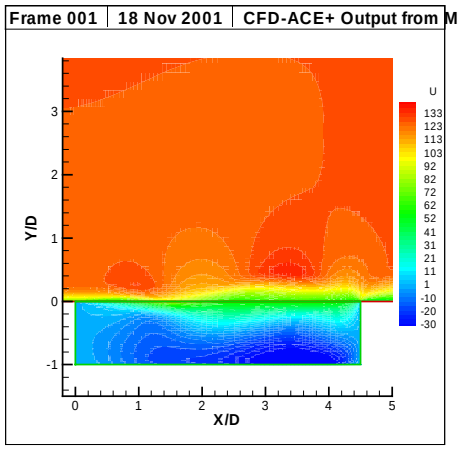

(a)

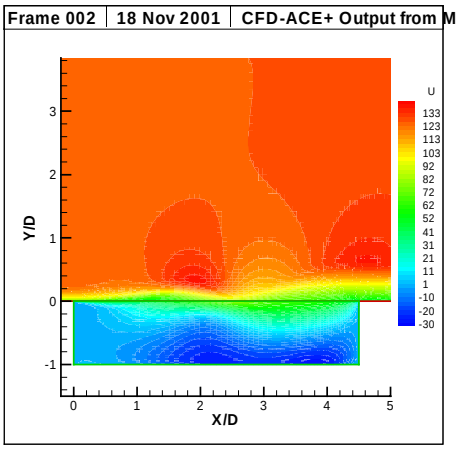

(b)

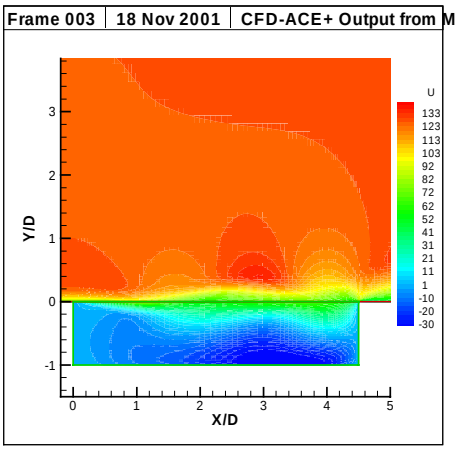

(c)

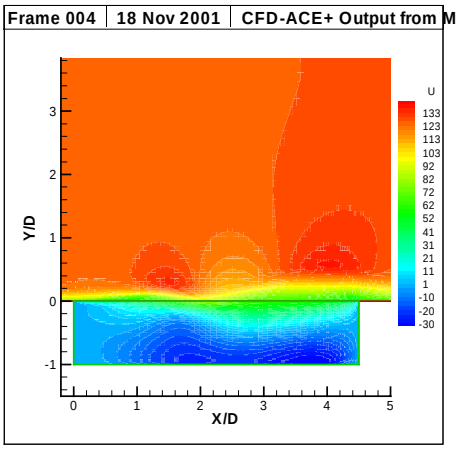

(d)

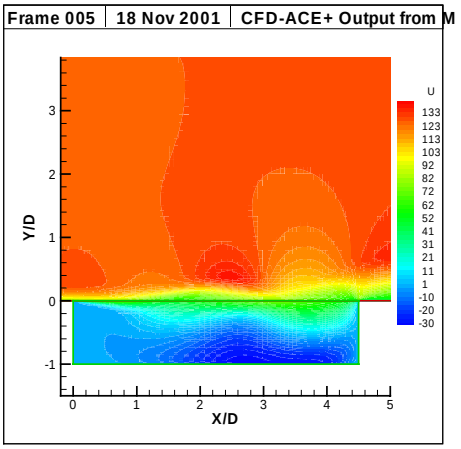

(e)

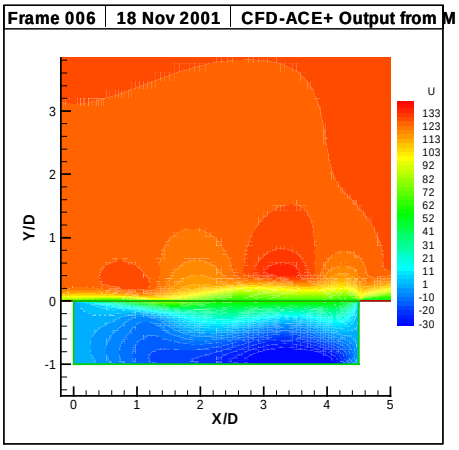

(f)

Figure 5.72 Numerically Simulated Instantaneous Velocity Contours, Cavity L/D = 4.5, M = 0.4

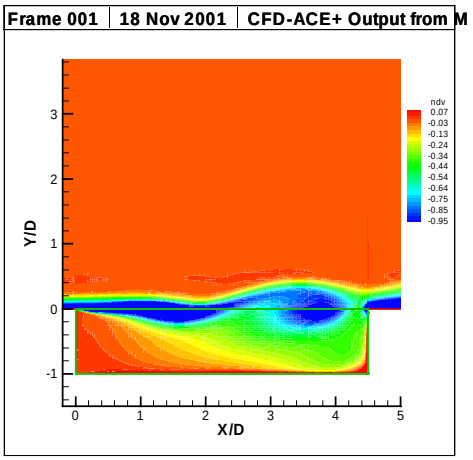

(a)

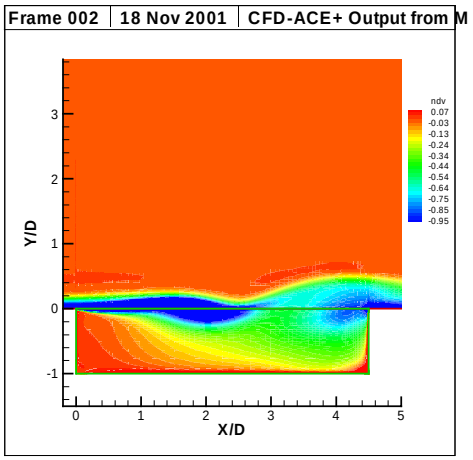

(b)

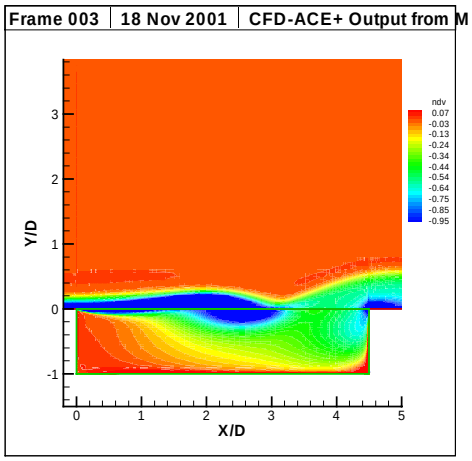

(c)

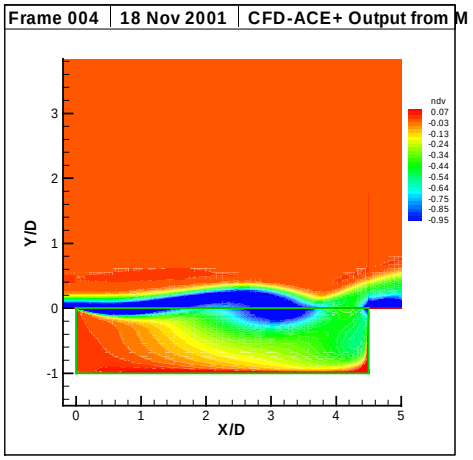

(d)

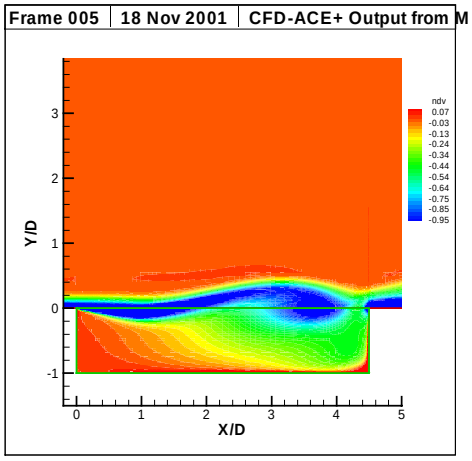

(e)

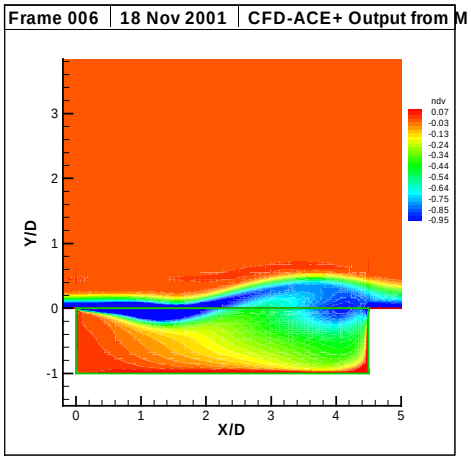

(f)

Figure 5.73 Instantaneous Non-Dimensional Vorticity Contours, Cavity L/D = 4.5, M = 0.6

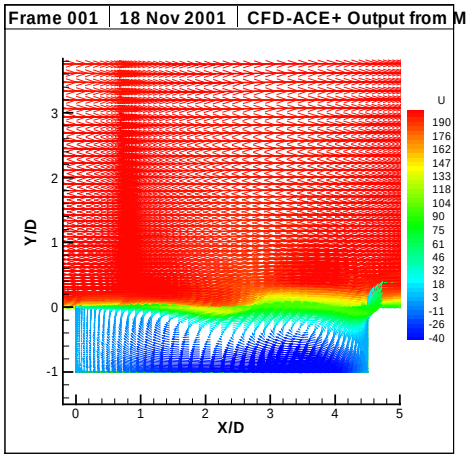

(a)

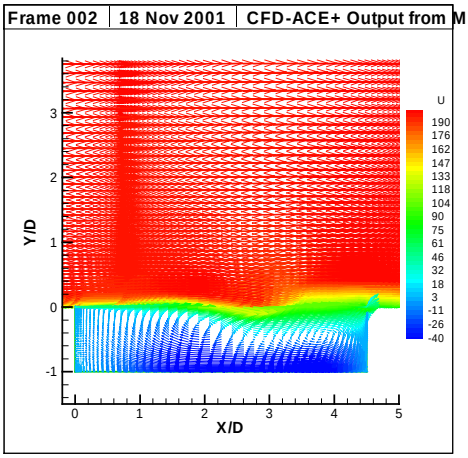

(b)

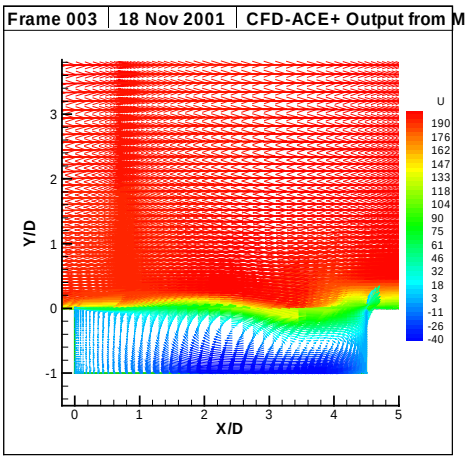

(c)

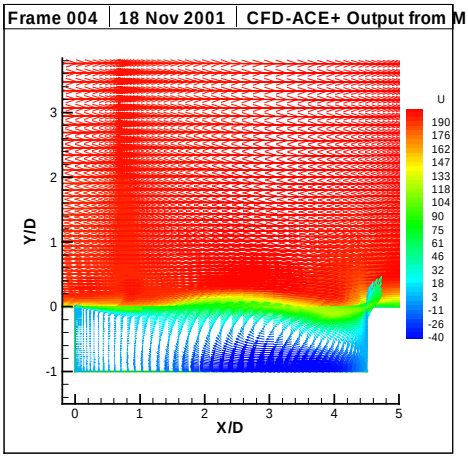

(d)

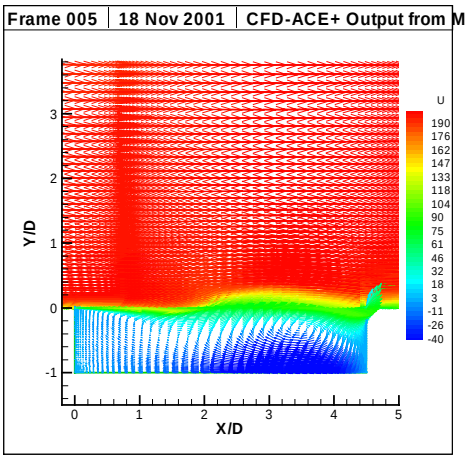

(e)

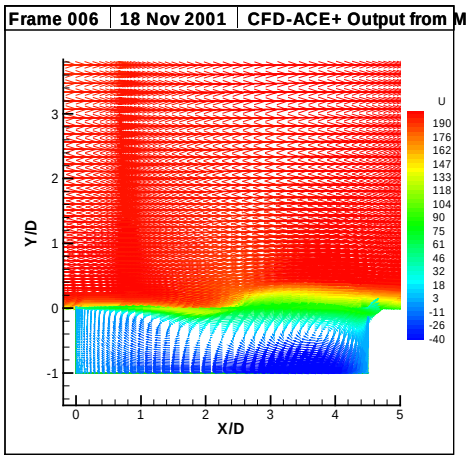

(f)

Figure 5.74 Numerically Simulated Velocity Vectors, Cavity L/D = 4.5, M = 0.6

exhibit excellent agreement with the corresponding experimental results plotted in figures 5.43 (a-f). The velocity vectors clearly show the formation of a vortex immediately downstream of the separation point. This vortex then travels downstream and coalesces with the recirculation zone that exists in the right half of the cavity. However, the experimental results show two non-stationary recirculation zones as opposed to one recirculation zone predicted numerically. This may be attributed to the increased value of turbulent viscosity in the computations. Velocity contours for cavity L/D = 4.5 at a freestream Mach number of 0.6 are plotted in figures 5.75 (a-f).

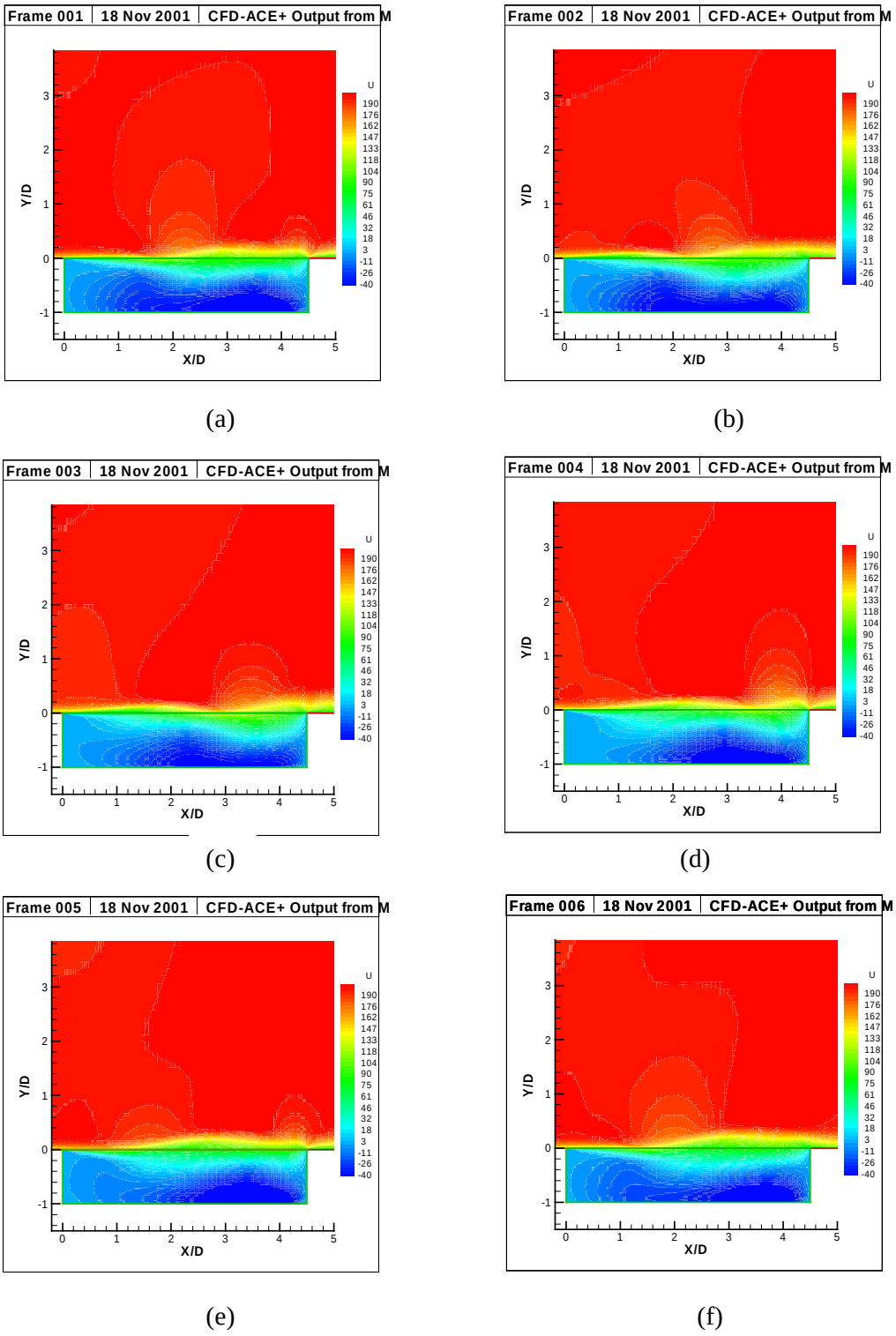

Figure 5.75 Numerically Simulated Instantaneous Velocity Contours, Cavity L/D = 4.5,

Chapter 6

Conclusions and Recommendations for Future Work

6.1 Conclusions

The following conclusions have been drawn from an experimental and numerical study of pressure oscillations in flow over cavities with L/D = 2.5 and 4.5, for freestream Mach numbers of 0.3-0.6, and the corresponding Reynolds numbers ranging from 1.5 x 10^6 to 3.27 x 10^6 . Conclusions drawn from the velocity field data obtained by Particle Image Velocimetry measurements for cavity L/D = 2.5 and 4.5 are also presented in the following sections.

Time histories of dynamic pressure data were obtained by placing a pressure transducer on the floor of a cavity with L/D = 2.5, W/D = 3.333, at a position of L = 2D. The corresponding spectra of the dynamic pressure data showed that the measured cavity oscillation frequencies were in good agreement with the frequencies predicted by the modified Rossiter's semi-empirical formula for cavity oscillations. The onset of oscillations occurred at a freestream Mach number of 0.5. Cavity L/D = 2.5 exhibited the phenomenon of mode switching between freestream Mach numbers of 0.57 and 0.6. The cavity oscillation mode switched from the third mode (f = 4722Hz) at M = 0.57 to the first mode (f = 1617 Hz) at M = 0.6.

Using Particle Image Velocimetry (PIV), boundary layer measurements were made for freestream Mach numbers of 0.4, 0.57 and 0.6 at a position upstream of the cavity. The boundary layer profiles showed that the incoming boundary layer was fully turbulent for all three Mach numbers.

At a freestream Mach number of 0.4, PIV measurements performed for cavity L/D = 2.5 showed no organized vorticity structures in the shear layer spanning the length of the cavity. This corresponded with no significant peaks in the power spectrum of the pressure signal.

Averaged vorticity contours obtained for a freestream Mach number of 0.57 showed that the shear layer was developing non-linearly approximately along 85 % of the length of the cavity. The early onset of non-linear shear layer growth appeared to be instrumental in the selective amplification of the third mode of oscillation in preference to its fundamental mode. Vorticity was well defined in the shear layer, as calculated from the PIV measurements. Velocity vectors exhibited periodic entrainment and ejection of fluid at the trailing edge of the cavity and the existence of two non-stationary recirculation zones that tended to occupy mostly the right half of the cavity.

Vorticity contours calculated for a freestream Mach number of 0.6 showed a well-organized shear layer that corresponded to a well-defined Sound Pressure Level (SPL) peak in the power spectrum at M = 0.6. Averaged vorticity contours obtained for a freestream Mach number of 0.6 showed that the shear layer was developing non-linearly approximately along 68 % of the length of the cavity. This is 17 % less than what is observed for the cavity configuration at M = 0.57. This amplification of the fundamental mode of oscillation appeared related to shear layer nonlinear development distance.

The onset of oscillations in cavity L/D = 4.5 occurred at a freestream Mach number of 0.6. For a given Mach number, the transducer at L = 4D produced a higher level of background noise than the pressure transducer at L = 2D. The frequency of the SPL peaks displayed in the spectra for cavity L/D = 4.5 corresponded to the second mode of cavity oscillations.

Vorticity contours obtained from velocity field measurements made for cavity L/D = 4.5 at a freestream Mach number of 0.4 showed no organized vorticity structures in the shear layer. No large SPL peak was observed in the power spectrum of the corresponding dynamic

pressure data. At a freestream Mach number of 0.6, vorticity was well organized in the shear layer and this corresponded to the well-defined SPL peak in the power spectrum. The velocity vectors show the formation of a vortex immediately downstream of the leading edge of the cavity that travels downstream and merges with the recirculation zone occupying the right half of the cavity.

Numerically simulated power spectra of the dynamic pressure data on the floor of cavity L/D = 2.5 showed that the measured cavity oscillation frequencies were in good agreement with the frequencies predicted by the Rossiter semi-empirical formula. The numerical onset of self-sustained oscillations occurred at a freestream Mach number of 0.4 as compared with a freestream Mach number of 0.5 observed in experiments. The phenomenon of mode switching was observed at an earlier freestream Mach numbers of 0.5 and 0.57 in the numerical simulations, whereas experiments showed that mode switching occurred between freestream Mach numbers of 0.57 and 0.6.

For a given freestream Mach number, the numerically calculated boundary layers momentum thickness was smaller than that measured in experiments. This may be related to the two-dimensionality of numerical computations, whereas the experiments were affected by the influence of freestream energy in the spanwise direction. The thinner shear layers predicted in computations could have been responsible for the onset of numerical oscillations at lower Mach numbers, when compared with the onset of oscillations in the experimentally measured spectra.

Numerically predicted velocity field data for cavity L/D = 2.5 at freestream Mach numbers of 0.4, 0.5, 0.57 and 0.6 showed periodic formation and convection of the shear layer vortices over the length of the cavity. Contours of vorticity compared well with the vorticity contours obtained experimentally. Numerical data showed the presence of one recirculation zone within the cavity in contrast with two unsteady recirculation zones observed in

experiments. This may be due to the effect of viscous diffusion and additional turbulent viscosity in the numerical simulations.

Numerically predicted flow field for cavity L/D = 4.5 captured most of the flow features of the cavity as observed from experimental data. Pressure Time histories, at corresponding points of experiments, indicated the upstream propagation of an pressure disturbance.

6.2 Future Work

It is recommended that experiments designed to study the three-dimensionality effects on cavity oscillations be performed.

PIV image acquisition should be time controlled and phase coupled with a periodic (pressure) signal in the flow, such that a set of images is acquired at a predetermined phase of the pressure signal. Phase-correlated velocity fields of the cavity oscillation cycle can be obtained then. A sequence of velocity fields that represent one oscillation cycle of the cavity would be of better use in comparison with numerical predictions, and in design of cavity oscillation suppression techniques. Furthermore, the effects of upstream mass injection on the vortical structures in the shear layer and the flow field as a whole could be better studied using phase conditioned PIV.

Performing three-dimensional numerical simulations of the cavity flow field in addition to the two-dimensional results that are presented in this work would serve to highlight the similarities and differences between 2-D and 3-D cavity simulations. It would also be useful to model the effect of the upstream mass injection on the cavity flow field using CFD and compare it with the experimental results.

LIST OF REFERENCES

[1] Rockwell, D., " Oscillation of Impinging Shear Layers", AIAA Journal, Vol. 21, No.5, May 1983, pp. 645-664

[2] Wilcox, F.J.Jr, "Passive Venting System for Modifying Cavity Flow Fields at Supersonic Speeds", AIAA Journal, Vol. 26, No. 3, March 1998, pp. 374-376

[3] Sarohia, V., and Massier, P.F., "Control of Cavity Noise", AIAA Journal of Aircraft, Vol. 14, No. 9, September 1977, pp. 833-837

[4] Franke, M.E., and Carr, D.L., "Effect of Geometry on Open Cavity Flow Induced Pressure Oscillations", AIAA Paper No. 75-492, March 1975

[5] Rossiter, J.E., "Wind Tunnel Experiments on the Flow Over Rectangular Cavities at Subsonic and Transonic Speeds", ARC R&M No. 3438, October 1964

[6] Heller, H.H., and Bliss, D.B., "The Physical Mechanism of Flow Induced Pressure Fluctuations in Cavities and Concepts for their Suppression", AIAA Paper No. 75-491, March 1975

[7] Vakili, A.D., Wu, J.M., and Taylor, M., "Shear Flow Control Applied to Suppress Cavity Oscillations and Improve Store Separation", Weapons Carriage and Separation Workshop, Wright Patterson AFB, Dayton, OH, April 1988

[8] Vakili, A.D., and Gauthier, C., "Control of Cavity Flow by Upstream Mass Injection", AIAA Journal of Aircraft, Vol.31, No.4, January-February 1994, pp. 169-174

[9] Robert C. Wolfe, "An Investigation of the Effects of Upstream Mass Injection on Cavity Oscillations", Master's Thesis, University of Tennessee, Knoxville, May 1995

[10] Chen, C.H., "Study of Subsonic and Transonic Flow Separation – With and Without Upstream Influence", Doctoral Dissertation, University of Tennessee, Knoxville, 1975

[11] Blair, A.B.Jr, and Stallings, R.L., "Supersonic Axial Flow Characteristics of a Rectangular-Box Cavity with various Length-to-Depth ratios in a Flat Plate", NASA TM-87659, April 1986

[12] Maureen B. Tracy and E. B. Plentovich, "Cavity Unsteady-Pressure Measurements at Subsonic and Transonic Speeds", NASA TP-3669, December 1997

[13] Micahel J. Lucas., "Handbook of the Acoustic Characteristics of Turbomachinery Cavities", 1997

[14] Rockwell, D., and Naudascher, E., "Review – Self Suataining Oscillations of Flow Past Cavities", ASME Journal of Engineering, Vol. 100, No. 2, June 1978, pp. 152-165.

[15] Krishnamurthy, K., "Acoustic Radiation from Two-Dimensional Rectangular Cutouts in Aerodynamics Surfaces", NACA TN 3487, August 1955.

[16] Roshko, A., “Some Measurements of Flow in Rectangular Cutout”, NACA TN 3488, August 1955

[17] Plumblee, H.E., Gibson, J.S., and Lassiter, L.W., “A Theoreticl and Experimental Investigation of the Acoustic Response of cavities in an Aerodynamic Flow”, WADD-TR-16-75, March 1962

[18] Heller, H., Holmes, D.G., and Covert, E.E., “Flow Induced Pressure Oscillations in Shallow Cavities”, Journal of Sound and Vibration, Vol. 18, No.4, 1971, pp. 545-553

[19] Bilanin, A.J., and Covert, E.E., “Estimation of Possible excitation Frequencies for Shallow Rectangular Cavities” AIAA Journal, Vol. 11, No. 3, March 1973, pp 347-351

[20] Heller, H., and Bliss, D., Aerodynamically Induced Pressure Oscillations: Physical Mechanism and Suppression Concepts”, Wright-Patterson Airforce Base, Ohio, AFFDL-TR-74-133, February 1975

[21] Sarohia, V., “Experimental Investigation of Oscillations in Flows over Shallow Cavities”, AIAA Journal, Vol. 15, No.7, July 1977, pp. 984-991

[22] Tam, C.K.W., and Block, P.J.W., “On the Tones and Pressure Oscillations Induced by Flow Over Rectangular Cavities”, Journal of Fluid Mechanics, Vol. 89, Part 2, 1978, pp. 373-399

[23] Cattafesta et al., “Experiments on Compressible Flow-Induced Cavity Oscillations”, AIAA Paper No. 98-2912

[24] Spina, E.F. et al., “An Experimental Investigation of Flow-Induced Cavity Oscillations”, AIAA Paper No. 3705

[25] Zhang, Xin, “Compressible Cavity Flow Oscillation due to Shear Layer Instabilities and Pressure Feedback, AIAA Journal, Vol. 33, No. 8, August 1995, pp. 1404 – 1411.

[26] Rona, A., and Dieudonne, W., “Unsteady Laminar and Turbulent Cavity Flow Models by Second Order Upwind Methods, AIAA Paper No. A99-16521.

[27] Colonius, T., Basu, A.J., and Rowley, C.W., “Numerical Investigation of the Flow Past a Cavity”, AIAA Paper No. 99-1912.

[28] Chung-Jen Tam, Orkwis, P.D., and Disimile, P.J., “A Comparison of Several Standard Turbulence Models for 2-D Open Cavity Flow Field Computations”, AIAA Paper No. 95-0361.

[29] Rona, A., Chen, X.X., and Zhang, X., “Control of Cavity Flow Oscillation Through Leading Edge Flow Modifications”, AIAA Paper No. 98-0672.

[30] Kim, I. and Chokani, N., "Navier-Stokes Study of a Supersonic Cavity Flowfield with Passive Control," Journal of Aircraft, Vol. 29, Mar.-Apr. 1992, pp. 217-223.

[31] Lamp, A. M. and Chokani, N., "Computation of Cavity Flows with Suppression Using Jet Blowing," Journal of Aircraft, Vol.34, July-Aug. 1997, pp. 545-551.

[32] CFD-ACE (U) User Manual, Version 6.4, January 2001.

[33] Meganathan, A.J., "An Experimental Study of Low Speed Open Cavity Flows," Master of Science Thesis, University of Tennessee, Knoxville, December 2000.

[34] Gray, C., Greated, C.A., McCluskey, D.R. and Easson, W.J., "An Analysis of the Scanning Beam PIV Illumination System,".J. Phys. Measurement Science and Technology 2, pp. 717-24.

[35] Westerweel, J., "Efficient Detection of Spurious Vectors in Particle Image Velocimetry Data," Experiments in Fluids, vol.23, 1994, pp. 20-28.

[36] Hart, D.P., "The Elimination of Correlation Errors in PIV Processing," International Symposium on Applications of Laser Techniques to Fluid Mechanics, Lisbon, Portugal, July 1998.

APPENDIX

Appendix A

The accuracy of velocity measurement by particle image velocimetry (PIV) depends upon the accuracy with which image displacements can be measured and the accuracy with which image displacements can be related to particle locations and their respective displacements. In order to obtain accurate PIV measurements, it is important to identify the sources of error that cause degradation in the accuracy. The sources of error may be broadly classified into three main types: (1) Seeding errors, (2) Recording errors, and (3) Analysis errors. Each one of these sources of error is described briefly in the following sections.

A.1 Seeding Errors

The measurement principle in PIV is to measure the velocity of the seeding particles, assuming that this is the same as the fluid velocity. If the seeding particles move relative to the fluid, the velocity of the seeding particles will deviate from the fluid velocity, and errors are introduced. Therefore, it is important to seed the flow with particles with the appropriate size and weight so that their velocities are representative of the flow velocities. Another important consideration is the amount of light that the seeding particles scatter. If the amount of light scattered by the particles is relatively small, the camera may not be sensitive enough to record the images of the particles thus resulting in low seed density. On the other hand, excessive amount of light scattered by the seeding particles could result in the saturation of the recording pixels in the digital camera. Therefore, the light scattering characteristics of the seeding particles should be an important consideration when deciding upon the size and material of the particles.

A.2 Recording Errors

The flow field is illuminated with a flat laser sheet. If the sheet is not perpendicular with the line of sight of the camera, the magnification will be different for different regions in the image, and this will lead to errors in the velocity measurements. Another source of error is due to the non-uniform thickness of the laser sheet due to its Gaussian profile [34]. Therefore the seeding particles lying in the sheet will be unequally illuminated depending on their position relative to the centre of the sheet. The diameter of the particle image depends on the intensity of light scattered by the particles, and thus the diameter of the recorded particles will vary. This introduces noise in the measurements, and influences the accuracy of the analysis.

The light scattered from the seeding particles pass through air and glass before it reaches the lens of the camera. Due to the different refraction indexes of air and glass the relative position of the particles in the image is different from their position in the flow field. This causes bias in the position of the velocity vector. Analytical corrections can be applied to reduce the error due to refraction.

A.2 Analysis Errors

Once the flow field images are acquired, correlation analysis is performed to obtain the velocity vectors. Correlation methods are subject to inherent errors that arise from finite seeding particle numbers, and image resolution. Currently, the most widely used technique to eliminate correlation errors is to compare vectors with their neighbors to determine if they are within a range of an appropriate statistical quantity like the mean velocity. The regions where the velocity vectors are eliminated are filled with interpolated vectors. The process of interpolation is a source of error in the PIV measurements. Techniques outlined in detail by Westerweel [35] and Hart [36] can help in reducing the errors due to correlation.

VITA

Sekhar Radhakrishnan was born in Devtang, Bhutan and got his early schooling in various parts of India due to his fathers itinerant defense career. For his undergraduate degree, Sekhar attended the Madras Institute of Technology, Anna University, and graduated with a Bachelor's degree in Aeronautical Engineering in May 1996. He obtained his Masters degree in Mechanical Engineering from UT Space Institute in December 1998. Sekhar got his Doctoral degree in May 2002. His major advisor both in the Masters and Doctoral programs was Dr. Ahmad Vakili. Sekhar is currently employed by CFDRC, a numerical simulations company in Huntsville, Alabama.